New Physics with Neutral and Charged Current Measurements at Long-Baseline Neutrino Experiments

By

Samiran Roy

PHYS08201304002

Harish-Chandra Research Institute, Allahabad

A thesis submitted to the

Board of Studies in Physical Sciences

In partial fulfillment of requirements

for the Degree of

DOCTOR OF PHILOSOPHY

of

HOMI BHABHA NATIONAL INSTITUTE

December, 2019

Homi Bhabha National Institute[1]

Recommendations of the Viva Voce Committee

As members of the Viva Voce Committee, we certify that we have read the dissertation prepared by Samiran Roy entitled "New Physics with neutral and charged current measurements at Long Baseline Neutrino Experiments" and recommend that it may be accepted as fulfilling the thesis requirement for the award of Degree of Doctor of Philosophy.

Chairman – Prof. Ashoke Sen.	**Date: 10-07-2020**
Guide / Convener – Prof. Raj Gandhi	**Date: 10-07-2020**
Co-guide – Prof. Poonam Mehta	**Date: 10-07-2020**
Examiner - Prof. S. Umasankar	**Date: 10-07-2020**
Member 1- Prof. Anshuman Maharana	**Date: 10-07-2020**
Member 2- Prof. Santosh K. Rai'.	**Date: 10-07-2020**
Member 3- Prof. Ujjwal Sen	**Date: 10-07-2020**

Final approval and acceptance of this thesis is contingent upon the candidate's submission of the final copies of the thesis to HBNI.

I/We hereby certify that I/we have read this thesis prepared under my/our direction and recommend that it may be accepted as fulfilling the thesis requirement.

Date: 10.07.2020

Place: Prayagraj

Prof. Poonam Mehta
Co-guide

Prof. Raj Gandhi
Guide

[1] This page is to be included only for final submission after successful completion of viva voce.

STATEMENT BY AUTHOR

This dissertation has been submitted in partial fulfillment of requirements for an advanced degree at Homi Bhabha National Institute (HBNI) and is deposited in the Library to be made available to borrowers under rules of the HBNI.

Brief quotations from this dissertation are allowable without special permission, provided that accurate acknowledgement of source is made. Requests for permission for extended quotation from or reproduction of this manuscript in whole or in part may be granted by the Competent Authority of HBNI when in his or her judgment the proposed use of the material is in the interests of scholarship. In all other instances, however, permission must be obtained from the author.

Samiran Roy

Samiran Roy

DECLARATION

I, Samiran Roy, hereby declare that the investigation presented in the thesis has been carried out by me. The work is original and has not been submitted earlier as a whole or in part for a degree / diploma at this or any other Institution / University.

Samiran Roy

Samiran Roy

List of Publications arising from the thesis

Journal

1. "Correlations and degeneracies among the NSI parameters with tunable beams at DUNE", M. Masud, Samiran Roy, P.Mehta, *Phys. Rev. D 99, 115032* (**2019**).

2. "What measurements of neutrino neutral current events can reveal", R. Gandhi, B. Kayser, S. Prakash, Samiran Roy, *JHEP 1711* (**2017**) 202.

3. "Effect of Non Unitarity on Neutrino Mass Hierarchy determination at DUNE, NOvA and T2K", D. Dutta, P. Ghoshal, Samiran Roy, *Nucl.Phys. B920* (**2017**) 385-401.

4. "Non Unitarity at DUNE and T2HK with Charged and Neutral Current Measurements", D. Dutta, Samiran Roy, *arXiv:1901.11298 [hep-ph]*, **2019.** (Preprint)

Conferences

1. Poster Presentation in the Neutrino and Dark Matter Activity at HRI, Allahabad, India in February 2019. Title: "What measurements of neutrino neutral current events can reveal".

2. Talk at Workshop on High Energy Physics Phenomenology XV (WHEPP), IISER Bhopal, India,December 2017. Title: "Short Baseline Neutrinos".

3. Talk at XXII DAE-BRNS HIGH ENERGY PHYSICS SYMPOSIUM, University of Delhi, India. Title: "Parameter Degeneracies in presence of Non Standard Interactions at Dune".

Samiran Roy

Samiran Roy

Dedicated to

My parents

ACKNOWLEDGEMENTS

First and foremost, I would like to thank my supervisor Prof. Raj Gandhi and co-supervisor Prof. Poonam Mehta for all their support and encouragement throughout my PhD work. They provided an excellent guidance to me both academically and non-academically throughout this significant journey of my life.

I would like to give a very special thanks to Prof. Boris Kayser for the fruitful discussions that immensely helped me in learning neutrino physics. It gives me an immense pleasure to thank my collaborators: Dr. Pomita Ghoshal, Dr. Debajyoti Dutta, Dr. Mehedi Masud, and Dr. Suprabh Prakash.

Next, the turn for HRI, where I spent one of the most excellent times of my life. My wholehearted thanks goes to Ritabrata, Sarif, Abhass, Sandeep, Gautam, Pradeep, Dhruv, Sreetama, Dipyaman, Shouvik, Arpan, Avirup, Purusottam, Sauri, Alam, Nirnoy, Biswajit, Atri, Subhojit, Bidisha, Jaitra, Mithun, Subha, Nabin, Sumana, Samrat da, Jayita di, Arnab, Satadal, Arijit, Deepak whom I interacted with at various times during my PhD and became good friends.

Last but not the least, I am forever grateful to my loving parents and my elder sister and brother in law for their constant support whenever I needed them.

Contents

List of Figures

List of Tables

Chapter 6

Conclusion

In this thesis, we have studied the capability of the long-baseline experiments to constrain new physics scenarios using CC and NC measurements. We have also discussed about the effect of non unitarity on the mass hierarchy determination at long-baseline experiments. The main conclusions from these various studies are summarized as follows.

We examine how NC events can synergistically aid the search for new physics and CP violation when combined with other measurements. We show that typically the NC events offer a window to CP phases and mixing angles that is complementary to that accessed by CC event measurements at both long and short baseline experiments. They can break degeneracies existing in CC measurements, allowing one to distinguish between new physics that violates 3+0 unitarity and new physics that does not. NC events seem not to be affected greatly by matter effects which arise at energies and baselines relevant to DUNE, rendering analytical understanding of new physics somewhat easier. They also aid in constraining parameters that are not easily accessible to CC measurements. Overall, in an experimental era when combined measurements can lead to significantly increased precision and understanding, NC studies can play a valuable role in the search for new physics at neutrino detectors.

We have studied constraints on non unitarity parameters at DUNE and T2HK, specially focusing on the contribution of the NC measurements at DUNE. We have calculated the NC events in the presence of both heavy and light sterile neutrinos and have found that even in the averaged out regime of light sterile neutrinos, the NC events are different from the heavy sterile case in the leading order. In this analysis, we have found that the ν_e background is the most dominant component in the measurements of the α_{11} parameter and hence this parameter will be better bounded by this background than by the signal. In case of the α_{22} parameter, NC measurements help in enhancing the bounds further. We have also found that combining both DUNE and T2HK can improve overall bounds on all the NU parameters. Finally, we have found that NC measurements at DUNE help in deriving better bounds on the α_{33} parameter compared to the CC measurements.

Long baseline neutrino experiments are sensitive to large matter effects and they have the potential to resolve the mass ordering in the neutrino sector. The superbeam experiment DUNE is one of the most promising candidates to study the neutrino mass hierarchy, along with NOνA and T2K. But in the presence of non unitarity of the leptonic mixing matrix, the capability of such experiments to discriminate between the two hierarchies gets suppressed. The mass hierarchy sensitivity of DUNE decreases in the presence of new physics. In this chapter we analyse the origin and extent of this loss of sensitivity at the level of oscillation probabilities, events, mass hierarchy sensitivity and the discovery reach of DUNE, NOνA and T2K. We have found that in the presence of NU, the mass hierarchy sensitivity of NOνA and T2K decreases significantly. But DUNE can still resolve the neutrino mass hierarchy at more than 5σ C.L. irrespective of the true hierarchy.

We address the question of constraining the parameter space of NSI parameters at DUNE by exploiting wide band nature of the beam. We systematically study correlations among various parameters using two beam tunes (LE and ME) and illustrated that to probe a subset of NSI parameter space more effectively, it is advantageous to use a combination of LE and ME tuned beams as opposed to using only the standard LE beam tune.

We provide a systematic and comprehensive description of the overall impact of the NSI parameters on the relevant probabilities (for $\nu_\mu \to \nu_e$ and for $\nu_\mu \to \nu_\mu$) as a function of energy as well as the CP phase. In the section 5.5, we provide analytic expressions of all the relevant expressions for the SI-NSI probability differences in the presence of individual NSI parameters (taken one at a time). These aid in our understanding of the dependencies of oscillation probabilities. We then quantify the differences in terms of a $\Delta\chi^2$ quantity and connected the features obtained to the probability level description. In Fig. 5.9, we have illustrated the $\Delta\chi^2$ correlations among the various parameters in the new parameter space appearing in the presence of NSI at a confidence level of 99%. Our key findings can be summarized as follows. The degenerate contours in the space associated with parameters, $|\varepsilon_{e\mu}|$ and $\phi_{e\mu}$ (shown as panels shaded in light yellow colour in Fig. 5.9) shrink significantly when we use the LE+ME beam as opposed to LE beam alone. For a quantitative estimate of the improvement, one can compute the area of the parameter space outside each contour (i.e., above the confidence level of 99%) and express the area as the percentage of the total parameter space plotted. It is evident from the pair of numbers (cyan for LE and black for LE+ME) indicated in the light yellow panels that the LE+ME beam leads to improvement over the LE beam. For the remaining NSI parameters, we see marginal or no improvement in terms of constraining the parameters using LE+ME beam in comparison with LE beam. Our detailed analysis also provides explanation for distinguishing features of the $\Delta\chi^2$ contours for different parameters.

SUMMARY

Neutrino oscillations have been established on a firm footing. We have now entered in the precision measurement era in neutrino physics. Although we have reliable measurements of the mixing angles θ_{12} and θ_{13} and the mass squared differences (Δm^2_{21}, $|\Delta m^2_{31}|$), we do not know the mass hierarchy (*i.e.* the sign of Δm^2_{31}), octant of θ_{23} and also do not have completely conclusive information about leptonic CP phase (δ_{cp}). Upcoming various super beam neutrino experiments have the potential to give us very good information about these unknowns. These experiments are also quite sensitive to new physics which enters into the oscillation probability.

Neutrinos can be detected through charged current (CC) interactions. In CC measurements, the final state particles are a lepton along with a hadron. We distinguish different flavors of neutrino species in the CC process by detecting the corresponding lepton flavour. Neutrinos also interact through the Z boson, *i.e.* via neutral current (NC) interactions. In the standard neutrino oscillation scenario, the NC events are proportional to the total number of the active flavor neutrinos. But in the presence of new physics, the number of NC events are modified and can be used as a tool to search and constrain new physics scenarios. The synergy between CC and NC will help us to probe the new physics scenarios more effectively. We also discuss the effect of new physics to the standard neutrino oscillation measurements.

One of the forms of new physics under active exploration is an extra sterile neutrino, which mixes with the active neutrino flavours. The effect of a sterile neutrino shows up not only in the short baseline experiments but also in the long-baseline experiments because of the mixing mentioned above. All the active flavor neutrinos contribute to the neutral current processes and produce a large number of events. We note that the NC probability is immune to any parameter uncertainty in the 3+0 case as opposed to the charge current (CC) measurements. In the presence of sterile states, however, active flavors can oscillate into a sterile flavor, giving a lesser number of events compared to standard (3+0) case.

Thus any depletion of NC events indicates the presence of sterile neutrino. We can also use the NC measurements to test the unitarity of the leptonic mixing matrix.

The neutrino mass ordering is one of the principal unknowns in the neutrino sector. Long baseline neutrino experiments have the potential of resolving this issue as they are sensitive to large matter effects. In the presence of new physics such as non unitarity, the capability of such experiments to discriminate between the two hierarchies gets suppressed.

In this thesis, we focus on the capability of the long-baseline neutrino experiments to constrain various new physics scenarios such as light sterile neutrino, non unitarity of the leptonic mixing matrix, NSIs etc. We also focus on the degeneracy arises due to NSIs in the neutrino oscillations probability and the effect of new physics such as non unitarity in the measurements of mass hierarchy.

Chapter 1

Introduction

Neutrinos are the second most abundant particles in nature after photons. In the Standard Model (SM) [1], there are three flavor neutrinos which are electron type (ν_e), muon type (ν_μ), and tau type (ν_τ). Neutrinos are electrically neutral. They do not participate in the electromagnetic interactions, and they interact only through weak interactions with other SM particles. Neutrinos are produced in the flavor state through charged current (CC) interactions. But the flavor states do not coincide with the mass eigenstates. The flavor states are linear superpositions of the mass eigenstates and they are related to each other by the leptonic mixing matrix or Pontecorvo−Maki−Nakagawa−Sakata (PMNS) matrix [2, 3]. Consequently as the neutrino propagates, it can change its flavor. Standard neutrino oscillations depend on the two mass squared differences namely the solar (Δm^2_{21}) and atmospheric (Δm^2_{31}) differences, three mixing angles (θ_{12}, θ_{13}, and θ_{23}) and one CP violating phase (δ_{cp}). Since the neutrino is a very weakly interacting particle, it is very difficult to detect it. We need a large detector mass to get a significant amount of neutrino events. The present and the future experiments are focused on determining the properties of neutrinos, such as mass squared differences, mixing angles, and the CP violating phase more precisely. The other goals of the present and future experiments also include exploring scenarios with any kind of new physics present in the neutrino sector. In this thesis, we focus on the capabilities of long-baseline experiments to search for new physics scenarios and its effect on the standard measurements of the oscillation parameters.

In this chapter we first provide a brief history of the neutrino. Then, we describe SM, the physics of neutrino oscillations, and the mechanism of neutrino mass generation. We then describe some new physics scenarios in the neutrino sector and finally give a brief summary of our results.

1.1 History of neutrinos

In 1914, Chadwick demonstrated that the beta (β) spectrum from the decay of radioactive nuclei was continuous, in contrast to α and γ rays with unique energy spectrum. Later Meitner showed that the missing energy could not be described by the neutral γ rays and that led to the idea of the possible explanation of the continuous β- decay spectrum with a new neutral particle. In order to conserve energy, linear momentum and angular momentum (spin) in β- decay, W. Pauli [4] proposed a neutral weakly interacting spin-half fermion. Later, Enrico Fermi named the new particle as the *neutrino* in 1933 and gave his famous theory of β- decay in 1934, now known as the Fermi theory [5, 6]. In 1956, F. Reines and C.L. Cowan [7] were able to detect the (anti) neutrino through inverse beta decay and confirm its existence.

1.2 Neutrinos in the Standard Model

There are four fundamental forces in nature, namely gravity, strong, electromagnetic and weak forces. The SM combines the strong, electromagnetic and weak interactions of the elementary particles in the common framework of quantum field theory. The SM is a $SU(3)_C \times SU(2)_L \times U(1)_Y$ local gauge invariant theory where C, L and Y denote color, left-handed chirality and hyper charge respectively. Strong interactions are mediated by eight massless gluons which are the generators of $SU(3)_C$. The weak and the electromagnetic forces are mediated by massive bosons ($W^{\pm}$, Z) and a massless γ respectively. There are three generations in the SM, and the particles in the generations carry the same quantum numbers and they differ only in mass. The neutrinos (or leptons) do not carry any color charges. Therefore, here we consider only the electroweak part of the SM. The $SU(2)_L \times U(1)_Y$ local gauge invariant Lagrangian (considering only the leptonic part of the SM) is given by

$$\mathcal{L} \;=\; i\sum_{e,\mu,\tau} \bar{L}_{\alpha L} \not{D} L_{\alpha L} + i\sum_{e,\mu,\tau} \bar{l}_{\alpha R} \not{D} l_{\alpha R} - \sum_{\alpha,\beta=e,\mu,\tau} Y_{\alpha\beta} \bar{L}_{\alpha L} \Phi l_{\beta R} + h.c. \qquad (1.2.1)$$

where $L_{\alpha L} = (\nu_{\alpha L}\ l_{\alpha L})^T$ is the lepton doublet under $SU(2)_L$, $l_{\alpha R}$ is a singlet under $SU(2)_L$, Φ is the Higgs doublet and $Y_{\alpha\beta}$ are Yukawa couplings and

$$D_\mu = \partial_\mu + ig \sum_{a=1,2,3} A_{\mu a} \tau^a/2 + ig' B_\mu Y/2. \qquad (1.2.2)$$

Here $A^{\mu a}$ is the vector gauge boson field associated with the three generators $\tau^a/2$ (a=1,2,3) of the group $SU(2)_L$ and B_μ is the vector boson field associated with the generator Y of the group $U(1)_Y$. g and g' are the two independent coupling constants of $SU(2)_L$ and $U(1)_Y$ respectively. Expanding the covariant derivatives of Eq 1.2.1, we get the interaction Lagrangian of leptons with the gauge bosons:

$$\mathcal{L}_I = -\frac{1}{2} \bar{L}_{\alpha L} (g \not{A}^a \tau^a - g' \not{B}) L_{\alpha L} + g' \bar{l}_{\alpha R} \not{B} l_{\alpha R}$$

Separating the interaction Lagrangian into charged current (CC) and neutral current (NC) parts, we get :

$$\mathcal{L}_I^{CC} = -\frac{g}{2} \{ \bar{\nu}_{\alpha L} (\not{A}_1 - i\not{A}_2) l_{\alpha L} + \bar{l}_{\alpha L} (\not{A}_1 + i\not{A}_2) \nu_{\alpha L} \} \qquad (1.2.3)$$

and

$$\mathcal{L}_I^{NC} = -\frac{1}{2}\{\bar{\nu}_{\alpha L}(g\not{A}_3 - g'\not{B})\nu_{\alpha L} - \bar{l}_{\alpha L}(g\not{A}_3 + g'\not{B})l_{\alpha L} - 2g'\bar{l}_R\not{B}l_R\} \tag{1.2.4}$$

Now we define a field (W^μ) (such that it annihilates W^+ and creates W^- bosons) as:

$$W^\mu \equiv \frac{A_1^\mu - iA_2^\mu}{\sqrt{2}}$$

and we obtain

$$\begin{aligned} \mathcal{L}_I^{CC} &= -\frac{g}{2}\{\bar{\nu}_{\alpha L}\not{W} l_{\alpha L} + \bar{l}_{\alpha L}\not{W}^\dagger \nu_{\alpha L}\} \\ &= -\frac{g}{2\sqrt{2}}\bar{\nu}_\alpha\gamma^\mu(1-\gamma^5)l_\alpha W_\mu + \ h.c. \end{aligned} \tag{1.2.5}$$

The SM must include the quantum electrodynamics (QED) interaction :

$$\mathcal{L}_I^{(\gamma)} = e j_{em}^\mu A_\mu \tag{1.2.6}$$

where e is the electric charge of the elementary particle, A^μ is the electromagnetic field, and

$$j_{em}^\mu = \bar{l}\gamma^\mu l. \tag{1.2.7}$$

We can get the QED Lagrangian from the NC Lagrangian by combining A_3^μ and B_μ appropriately to define A^μ. We define two orthogonal fields (A^μ, Z^μ) as

$$\begin{aligned} A^\mu &= \sin(\theta_W)A_3^\mu + \cos(\theta_W)B^\mu \\ Z^\mu &= \cos(\theta_W)A_3^\mu - \sin(\theta_W)B^\mu. \end{aligned} \tag{1.2.8}$$

The angle θ_W is called the weak mixing angle or the Weinberg angle. Inserting the above two equations into Eq. 1.2.4 and using charge neutrality condition of neutrino, we get

$$\begin{aligned} \mathcal{L}_{I,L}^{(NC)} &= -\frac{g}{2\cos(\theta_W)}\{\bar{\nu}_{\alpha L}\not{Z}\nu_{\alpha L} - (1-2\sin^2\theta_W)\bar{l}_L\not{Z}l_L + 2\sin^2\theta_W\bar{l}_R\not{Z}l_R\} \\ &+ g\ \sin(\theta_W)\,\bar{l}\not{A}l. \end{aligned} \tag{1.2.9}$$

By defining $g\ \sin(\theta_W) = e$, we get the QED interaction Lagrangian as in Eq. 1.2.6 and the *weak neutral current* is given by

$$\mathcal{L}^Z = -\frac{g}{2\cos(\theta_W)} j_Z^\mu Z_\mu, \tag{1.2.10}$$

where

$$j_Z^\mu = \bar{\nu}_{\alpha L}\gamma^\mu\nu_{\alpha L} - (1-2\sin^2\theta_W)\bar{l}_L\gamma^\mu l_L + 2\sin^2\theta_W\bar{l}_R\gamma^\mu l_R. \tag{1.2.11}$$

Neutrinos are produced through a CC interaction and they can be detected through both CC and NC interactions. Any presence of new physics beyond the standard model, in principle can alter the detection and production process and we will discuss those issues in chapter 2 and chapter 3.

1.3 Neutrino Oscillation

Similar to the $K^0 \rightleftarrows \bar{K}^0$ oscillation in quark sector, neutrino-antineutrino oscillation [8,9] was proposed by Bruno Pontecorvo in 1957. In the 1967 paper [10], B.Pontecorvo discussed the effect of neutrino oscillations on the solar neutrinos. Three years later in 1970, the solar neutrinos were first measured by R. Davis [11, 12]. The observed neutrino flux from the sun was about 2-3 times smaller than the predicted neutrino flux by the Standard solar model [13]. Over a period of time, it was realized that the neutrino oscillation was the most natural way to explain the solar neutrino anomaly compared to any other astrophysical (or particle physics) explanation [14]. Finally the theory of neutrino oscillations was developed in 1975 – 76 by S. Eliezer and A.R. Swift [15], S.M. Bilenky and B. Pontecorvo [16].

Neutrinos are produced in flavor states (ν_α) through the CC interaction as in Eq. 1.2.5. Neutrinos are massless in the SM. But for neutrino oscillation, the neutrino should have mass, which allows the flavor and the mass basis to mix. We can represent the flavor states ($|\nu_\alpha\rangle$) as:

$$|\nu_\alpha\rangle = \sum_{i=1}^{3} U^*_{\alpha i}|\nu_i\rangle, \tag{1.3.1}$$

where U is the unitary lepton mixing matrix (or PMNS mixing matrix) and $|\nu_i\rangle$ is the mass eigenstate of i-th neutrino. The 3×3 PMNS mixing matrix is given by,

$$U = \begin{pmatrix} 1 & 0 & 0 \\ 0 & c_{23} & s_{23} \\ 0 & -s_{23} & c_{23} \end{pmatrix} \begin{pmatrix} c_{13} & 0 & s_{13}e^{-i\delta} \\ 0 & 1 & 0 \\ -s_{13}e^{i\delta} & 0 & c_{13} \end{pmatrix} \begin{pmatrix} c_{12} & s_{12} & 0 \\ -s_{12} & c_{12} & 0 \\ 0 & 0 & 1 \end{pmatrix}, \tag{1.3.2}$$

where $s_{ij} = \sin\theta_{ij}, c_{ij} = \cos\theta_{ij}$ and δ is the Dirac-type CP phase.

1.3.1 Neutrino Oscillations in Vacuum

In neutrino oscillation experiments, the flavor neutrinos are produced at the source through pion, kaon, or μ decays or via nuclear reactions. Those neutrinos are observed at the detector through weak processes, either via CC or NC interactions. As mentioned earlier, the flavor states are superpositions of mass eigenstates. During propagation, different mass eigenstates pick up different phases, resulting in a non-zero flavor transition probability. To observe the oscillation pattern, there are two necessary ingredients:

1) Neutrinos must maintain quantum coherence over the macroscopic distances.

2) At production and detection, there must be sufficient uncertainty in their momenta so that coherent flavor states are produced.

Consider a left-handed ultra relativistic neutrino with flavor α ($\alpha = e, \mu, \tau$) and momentum p produced at time $t = 0$,

$$|\nu_\alpha(t=0)\rangle = \sum_{i=1}^{3} U^*_{\alpha i} |\nu_i(t=0)\rangle. \tag{1.3.3}$$

After time t, the the flavor state becomes:

$$|\nu_\alpha(t)\rangle = \sum_{i=1}^{3} U^*_{\alpha i} |\nu_i(t)\rangle. \tag{1.3.4}$$

The massive state ($|\nu_i\rangle$) is an eigenstate of the vacuum Hamiltonian $\mathcal{H}_0$:

$$\mathcal{H}_0 |\nu_i\rangle = E_i |\nu_i\rangle, \quad \text{with} \quad E_i = \sqrt{p^2 + m_i^2}\,. \tag{1.3.5}$$

For ultrarelativistic neutrinos, we have

$$E_i \simeq E + \frac{m_i^2}{2E}, \quad p \simeq E. \tag{1.3.6}$$

Therefore, we can write the flavor states as

$$\begin{aligned} |\nu_\alpha(t)\rangle &= \sum_{i=1}^{3} U^*_{\alpha i} e^{-iE_i t} |\nu_i(t=0)\rangle \\ &= \sum_{i=1}^{3} U^*_{\alpha i} e^{-i(E+m_i^2/2E)t} |\nu_i(t=0)\rangle \\ &= \sum_{i=1}^{3} U^*_{\alpha i} e^{-i\Delta m_{i1}^2/2Et} |\nu_i(t=0)\rangle, \end{aligned} \tag{1.3.7}$$

where $\Delta m_{i1}^2 = m_i^2 - m_1^2$. We have neglected an overall phase factor in the above Eq. 1.3.7.

Hence, we can write the transition probability in vacuum as:

$$\begin{aligned} P(\nu_\alpha \to \nu_\beta) &= |\langle \nu_\beta | \nu_\alpha(t) \rangle|^2 \\ &= |\sum_{i=1}^{3} U^*_{\alpha i} e^{-i\Delta m^2_{i1}/2Et} U_{\beta i}|^2. \end{aligned} \tag{1.3.8}$$

Two Flavor Case:

Here for simplicity, we consider two flavor neutrinos to illustrate the neutrino oscillation in vacuum. For the two flavor case, the lepton mixing matrix (U) can be represented by only one mixing angle (θ) as:

$$U = \begin{pmatrix} \cos(\theta) & \sin(\theta) \\ -\sin(\theta) & \cos(\theta). \end{pmatrix}$$

The appearance probability ($\nu_\alpha \to \nu_\beta$) in the two flavor case is given by

$$P_{\alpha\beta} = \sin^2(2\theta)\sin^2(\frac{\Delta m^2_{21} L}{4E}), \quad \alpha \neq \beta, \tag{1.3.9}$$

and the survival probability ($\nu_\alpha \to \nu_\alpha$) is

$$P_{\alpha\alpha} = 1 - \sin^2(2\theta)\sin^2(\frac{\Delta m^2_{21} L}{4E}). \tag{1.3.10}$$

For an ultrarelativistic neutrino, t equals the length (L) in natural units. The oscillation amplitude depends on the mixing angle θ and the oscillation phase depends on mass squared difference (Δm^2_{21}), L and the energy (E) of the neutrino. The total oscillation probability *i.e.* $P_{\alpha\beta} + P_{\alpha\alpha}$ for a given flavor α equals to unity since the time evolution of the neutrino is unitary.

1.3.2 Neutrino Oscillation in Matter

The vacuum oscillation probability changes in presence of matter. When a neutrino propagates through matter, it interacts coherently with matter. Only electron type neutrinos interact with electrons in the medium coherently via CC interactions but all the flavor neutrinos interact coherently with up, down type quarks and electrons via NC interactions. The weak interaction consists of both the vector and the axial vector parts, of which only the vector parts add up coherently. The contribution in the oscillation Hamiltonian due to the charged current coherent process is given by

$$V_{CC} = \sqrt{2} G_F N_e,$$

where G_F is the Fermi constant and the N_e is the number density of the electron in the medium. In astrophysical environments with low temperature and density, the medium is composed of electrons, protons and neutrons, and electrical neutrality implies an equal number density of electrons and protons. The NC coherent contributions of electrons and protons cancel each other and only neutrons contribute coherently in the neutral current potential:

$$V_{NC} = -\frac{1}{2} \sqrt{2} G_F N_n,$$

where N_n is the number density of the neutrons in the medium. For anti neutrino, both V_{CC} and V_{NC} change sign. Now in presence of matter, the Schrodinger equation for the flavor neutrinos becomes

$$i\frac{d\Psi}{dx} = \frac{1}{2E}(UM^2U^\dagger + A)\Psi. \tag{1.3.11}$$

In the case of three neutrino mixing, we have

$$\Psi = \begin{pmatrix} \nu_e \\ \nu_\mu \\ \nu_\tau \end{pmatrix}, \quad M^2 = \begin{pmatrix} 0 & 0 & 0 \\ 0 & \Delta m_{21}^2 & 0 \\ 0 & 0 & \Delta m_{31}^2 \end{pmatrix}, \quad A = \begin{pmatrix} A_{CC} + A_{NC} & 0 & 0 \\ 0 & A_{NC} & 0 \\ 0 & 0 & A_{NC} \end{pmatrix}, \tag{1.3.12}$$

where $A_{CC} \equiv 2EV_{CC}$ and $A_{NC} \equiv 2EV_{NC}$. The neutral current potential (A_{NC}) will not contribute to the oscillation probability since we can absorb it in a redefinition of the neutrino field with an overall phase. Therefore, for three neutrino mixing, only the charged current matter potential term (A_{CC}) will affect neutrino propagation through matter. The matter effect plays a crucial role in neutrino oscillations. We discuss its effect in the following section.

The MSW Effect

For simplicity, we consider two neutrino mixing between ν_e, ν_μ and ν_1, ν_2. For two flavor case, the mixing matrix (U) is given by Eq. 1.3.9 and the time evolution of the flavor states becomes

$$i\frac{d}{dx}\begin{pmatrix} \nu_e \\ \nu_\mu \end{pmatrix} = \frac{1}{4E}\begin{pmatrix} -\Delta m^2 \cos(2\theta) + A_{CC} & \Delta m^2 \sin(2\theta) \\ \Delta m^2 \sin(2\theta) & \Delta m^2 \cos(2\theta) - A_{CC} \end{pmatrix}\begin{pmatrix} \nu_e \\ \nu_\mu \end{pmatrix}, \tag{1.3.13}$$

where θ is the mixing angle and $\Delta m^2 = m_2^2 - m_1^2$. The effective Hamiltonian (H_F) in presence of matter is given by

$$H_F = \frac{1}{4E}\begin{pmatrix} -\Delta m^2 \cos(2\theta) + A_{CC} & \Delta m^2 \sin(2\theta) \\ \Delta m^2 \sin(2\theta) & \Delta m^2 \cos(2\theta) - A_{CC} \end{pmatrix}. \tag{1.3.14}$$

We can diagonalize the above matrix by an orthogonal transformation

$$U_M^T H_F U_M = H_M, \tag{1.3.15}$$

where

$$H_F = \frac{1}{4E}\text{diag}(-\Delta m_M^2, \Delta m_M^2) \tag{1.3.16}$$

is the effective Hamiltonian in matter in the mass basis and

$$\Delta m_{\mathrm{M}}^2 = \sqrt{(\Delta m^2 \cos(2\theta) - A_{CC})^2 + (\Delta m^2 \sin(2\theta))^2}. \tag{1.3.17}$$

U_M is the effective unitary mixing matrix in matter which can be represented as:

$$U_M = \begin{pmatrix} \cos(\theta_M) & \sin(\theta_M) \\ -\sin(\theta_M) & \cos(\theta_M) \end{pmatrix}, \tag{1.3.18}$$

where θ_M is the effective mixing angle in matter and is given by

$$\tan(2\theta_M) = \frac{\tan(2\theta)}{1 - A_{CC}/\Delta m^2 \ \cos(2\theta)}. \tag{1.3.19}$$

Note that there will be a resonance when A_{CC} becomes equal to $\Delta m^2 \cos(2\theta)$ and the number density of electrons at resonance is given by

$$N_e^R = \frac{\Delta m^2 \ \cos(2\theta)}{2\sqrt{2}E\,G_F}. \tag{1.3.20}$$

The effective mixing angle (θ_M) becomes equal to $\frac{\pi}{4}$ (*i.e.* maximal mixing) at resonance. Therefore, total flavor transition from one flavor to another becomes possible in the two flavor case if the resonance region is broad enough. This phenomena is called the MSW effect [17, 18], named after Mikheev, Smirnov, and Wolfenstein.

Now A_{CC} is positive for neutrino in the normal matter. From Eq. 1.3.19, we can observe that the resonance exists only if $\theta < \pi/4$, as for $\theta > \pi/4$ the value of $\cos(2\theta) < 0$. The situation becomes reversed for the anti neutrino case, since A_{CC} is negative in matter.

If we consider constant matter density, then we can solve the differential Eq. 1.3.13 easily. For an electron type initial flavor, the appearance and disappearance transition probabilities are given by

$$\begin{aligned} P_{\nu_e \to \nu_\mu} &= \sin^2(2\theta_M)\sin^2(\frac{\Delta m_M^2 L}{4E}), \text{ and} \\ P_{\nu_\mu \to \nu_\mu} &= 1 - \sin^2(2\theta_M)\sin^2(\frac{\Delta m_M^2 L}{4E}). \end{aligned} \tag{1.3.21}$$

The structure of the above equations is identical to the two-neutrino oscillation probability in vacuum.

1.4 Neutrino Mass : type I see-saw mechanism

Neutrinos are massless in the standard model since there are no right handed neutrinos in the theory. But from neutrino oscillations, we know that neutrinos should have tiny mass squared differences, cosmology also indicates that neutrinos have very small absolute masses (< 1 eV) [19]. The most popular way to generate the small neutrino mass is the see-saw mechanism [20–23], by introducing right handed SM singlet fields into the theory. We consider N_s right handed sterile neutrino fields ν_{sR}, with $s = s_1, .., s_{N_s}$. In the presence of right handed sterile neutrinos, the most general Dirac-Majorana mass term can be written as

$$\mathcal{L}_{mass} = \mathcal{L}^L_{mass} + \mathcal{L}^R_{mass} + \mathcal{L}^D_{mass}, \tag{1.4.1}$$

where Majorana mass terms are,

$$\mathcal{L}^L_{mass} = \frac{1}{2} \sum_{\alpha\beta = e,\mu,\tau} \nu^T_{\alpha L} C^\dagger M^L_{\alpha\beta} \nu_{\beta L} + h.c., \tag{1.4.2}$$

$$\mathcal{L}^{R}_{mass} = \frac{1}{2} \sum_{s,s'=s_1,..,s_N} \nu^{T}_{sR} C^{\dagger} M^{R}_{ss'} \nu_{s'R} + h.c.\,, \tag{1.4.3}$$

and the Dirac mass term is,

$$\mathcal{L}^{D}_{mass} = \sum_{s=s_1,..,s_N} \sum_{\alpha=e,\mu,\tau} \bar{\nu}_{sR} M^{D}_{s\alpha} \nu_{\alpha L} + h.c. \tag{1.4.4}$$

The mass matrices M_L, M^R and M^D are complex. The Majorana mass matrices M_L and M^R are symmetric. Now, to obtain the neutrino fields with definite masses, we have to diagonalize Eq. 1.4.1. For convenience, we define a column matrix of N $(= 3 + N_s)$ left handed fields as

$$\mathbf{N}_L \equiv \begin{pmatrix} \nu_L \\ \\ \nu^{C}_{R} \end{pmatrix}, \tag{1.4.5}$$

where

$$\nu_L = \begin{pmatrix} \nu_{eL} \\ \\ \nu_{\mu L} \\ \\ \nu_{\tau L} \end{pmatrix}, \quad \text{and} \ \nu^{C}_{R} = \begin{pmatrix} \nu^{C}_{s_1 R} \\ \\ . \\ \\ . \\ \\ \nu^{C}_{s_N R} \end{pmatrix} \tag{1.4.6}$$

The general mass term in Eq. 1.4.1 can be written in the compact form as

$$\mathcal{L}_{mass} = \frac{1}{2} N^{T}_{L} C^{\dagger}\, M\, N_L + h.c., \tag{1.4.7}$$

where M is a $N \times N$ symmetric matrix and is given by

$$M = \begin{pmatrix} M_L & M^{D^T} \\ M^D & M^R \end{pmatrix}. \tag{1.4.8}$$

We can diagonalize Eq. 1.4.7 by the unitary matrix V. The definite mass eigenstates (n_L) are related to the flavor states (N_L) as

$$N_L = V\, n_L, \quad \text{with} \quad n_L = \begin{pmatrix} \nu_{1L} \\ . \\ . \\ \nu_{NL} \end{pmatrix}. \tag{1.4.9}$$

Now,

$$V^T\, M\, V \;=\; M_{\text{diag}}, \;\; \text{where}\;\; (M_{diag})_{kj} = m_k \delta_{kj} \;\; (k, j = 1, .., N), \tag{1.4.10}$$

with real and positive masses m_k. In terms of the massive left handed fields the mass term as in Eq. 1.4.7 becomes

$$\mathcal{L}_{mass} = \frac{1}{2} n_L^T C^\dagger\, M_{\text{diag}}\, n_L + h.c. \tag{1.4.11}$$

The M_L mass term is forbidden by SM gauge symmetry. Hence we will take $M_L = 0$. The mass term M_R is generated by new physics beyond the standard model. Thus we can take it very large. If all the eigenvalues of M_R are much bigger than the all elements of M_L, then we can diagonalize Eq. 1.4.10 as

$$V^T M V = M_{\text{diag}} \simeq \begin{pmatrix} (M_{light})_{3\times 3} & 0 \\ & \\ 0 & (M_{heavy})_{N_s \times N_s} \end{pmatrix}, \tag{1.4.12}$$

with

$$V \simeq \begin{pmatrix} 1 - \dfrac{1}{2} M^{D^\dagger} (M^R M^{R^\dagger})^{-1} M^D & [(M^R)^{-1} M^D]^\dagger \\ & \\ -(M^R)^{-1} M^D & 1 - \dfrac{1}{2} (M^R)^{-1} M^D M^{D^\dagger} (M^{R^\dagger})^{-1} \end{pmatrix}. \tag{1.4.13}$$

The light (M_{light}) and heavy (M_{heavy}) mass matrices are given by

$$M_{light} \simeq -M^{D^T} (M^R)^{-1} M^D, \quad M_{heavy} \simeq M^R \tag{1.4.14}$$

The eigenvalues of M^R will give the masses of the heavy neutrinos, whereas the eigenvalues of M_{light} will give light neutrino masses. Elements of M_{light} are suppressed with respect to M^D elements by the small matrix factor $M^{D^T}(M^R)^{-1}$. However, light neutrino masses and their relative magnitudes can vary over wide ranges, depending on the values of the M^D and M^R matrix elements. The neutrino mass generation above is called Type-I see-saw mechanism.

There are other see-saw mechanisms like the type II [24–28] and type III [29, 30] see-saw which produce small neutrino mass naturally by adding a new heavy scalar triplet (type II see-saw) or a heavy fermionic triplet (type III see-saw) under $SU(2)_L$ to the theory and there exists low scale see-saw *i.e.* the inverse see-saw mechanism [31, 32] which can produce small neutrino mass naturally by adding small lepton number violating terms in the theory. In the literature, there exist other mechanisms for small neutrino mass production: for e.g., models with specific textures for the mass matrix [33–35], models with $\mu - \tau$ symmetries [36–38], radiative models [39], and models with extra dimensions [40–43] etc.

1.5 Neutrino oscillation parameters: present status

Standard three neutrino oscillations depend on three mixing angles (θ_{12}, θ_{13}, and θ_{23}), two mass squared difference ($\Delta m^2_{21}, \Delta m^2_{31}$) and one CP violating phase (δ_{cp}). Although we have reliable measurements of the solar ($\Delta m^2_{21} = m^2_2 - m^2_1$) and atmospheric (magnitude of $\Delta m^2_{31} = m^2_3 - m^2_1$) mass squared differences and the mixing angles $\theta_{12}(\sim 33.8^o)$ and $\theta_{13}(\sim 8.6^o)$, we do not know the mass hierarchy (*i.e.* $\Delta m^2_{31} > 0$, normal hierarchy (NH) or $\Delta m^2_{31} < 0$, inverted hierarchy (IH)), octant of θ_{23} (i.e. θ_{23} can be either $> \frac{\pi}{4}$ or $< \frac{\pi}{4}$) and also do not have very good information about the leptonic CP phase (δ_{cp}). The present status of the neutrino oscillation parameters are shown in table 1.1.

Table 1.1: Current status of oscillation parameters [44].

Oscillation parameter	Best fit value	3σ range
$\theta_{12}/^\circ$	$33.82^{+0.78}_{-0.76}$	$31.61 \rightarrow 36.27$
$\theta_{23}/^\circ$ (NH)	$49.6^{+1.0}_{-1.2}$	$40.3 \rightarrow 52.4$
$\theta_{23}/^\circ$ (IH)	$49.8^{+1.0}_{-1.1}$	$40.6 \rightarrow 52.5$
$\theta_{13}/^\circ$ (NH)	$8.61^{+0.13}_{-0.13}$	$8.22 \rightarrow 8.99$
$\theta_{13}/^\circ$ (IH)	$8.65^{+0.13}_{-0.13}$	$8.27 \rightarrow 9.03$
$\delta_{cp}/^\circ$ (NH)	215^{+40}_{-29}	$125 \rightarrow 392$
$\delta_{cp}/^\circ$ (IH)	284^{+27}_{-29}	$196 \rightarrow 360$
$\Delta m^2_{21}/10^{-5}eV^2$	$7.39^{+0.21}_{-0.20}$	$6.79 \rightarrow 8.01$
$\Delta m^2_{31}/10^{-3}eV^2$ (NH)	$+2.525^{+0.033}_{-0.032}$	$+2.427 \rightarrow +2.625$
$\Delta m^2_{31}/10^{-3}eV^2$ (IH)	$-2.512^{+0.034}_{-0.032}$	$-2.611 \rightarrow -2.412$

1.6 New Physics in the neutrino sector

Three neutrino oscillations are established on a firm footing due to various experiments like Super-Kamiokande [45], T2K [46,47], Daya Bay [48] etc. We have now entered into the precision measurements era in neutrino oscillation. New physics in the neutrino sector has the potential to alter the measurements of the standard oscillation parameters. In this section, we will summarize a few relevant new physics scenarios.

A Light Sterile Neutrino

The short baseline experiment LSND [49] had found a significant excess of positron like signals over the estimated background from their primary anti-muon neutrino ($\bar{\nu}_\mu$) beam. The standard neutrino oscillation depends on the phase $\frac{\Delta m^2_{ij} L}{4E}$. Now the solar ($\Delta m^2_{21} \sim 10^{-5}$ eV^2) and atmospheric ($\Delta m^2_{31} \sim 10^{-3}$ eV^2) mass squared differences can not produce enough $\bar{\nu}_\mu \to \bar{\nu}_e$ transition for the LSND baseline ($L \sim 30$ m) and energy range ($E \sim 30$ MeV). To resolve these anomalies, a sterile neutrino of mass squared difference ~ 1 eV^2 was proposed. The sterile neutrino mass state mixes with the active flavors and is able to explain the excess positron like signal through the oscillation of $\bar{\nu}_\mu$ to $\bar{\nu}_e$. LSND results were tested in the MiniBooNE [50] experiment which also got an excess of events both in the neutrino and the anti-neutrino mode though it is not in an exact agreement with the LSND signal. Apart from these results, there are hints of light sterile neutrino from different other experiments. The somewhat lower than expected event rate at SAGE and GALLEX measurements also supports the sterile neutrino oscillation with $\Delta m^2 \gtrsim 1$ eV^2 [51, 52] (the Gallium anomaly). Also in reactor anti-neutrino experiments, the observed events are lower than the predicted values and this is known as the reactor anomaly. The observed lower number of events can be explained by sterile neutrino oscillations of mass squared difference $\gtrsim 1.5$ eV^2 [53]. But the sterile neutrino hypothesis does not fit very well in the global analysis of sterile neutrino. There exist tensions between the appearance and disappearance data [54,55] and also cosmology disfavour pure light sterile hypothesis [56].

Non Standard Interactions (NSI)

Neutrino mass already guarantees new physics beyond the standard model. Non-Standard interactions provide a general framework to quantify and the parametrize the effect of additional new physics in the neutrino sector in terms of an effective potential. Models of physics that predict NSIs include, for example, R-parity violating supersymmetric models [57], various see-saw models [58,59], left-right symmetric models, extra dimensions [60] etc. i.e. basically all modern beyond standard model physics could give rise to NSIs in the neutrino sector. The details of a particular model may vary, but typically they all have the following forms for neutral current (NC) and charged current (CC) NSIs,

$$\mathcal{L}_{NC} = -2\sqrt{2}G_F \sum_{f,P,\alpha,\beta} \varepsilon^{f,P}_{\alpha,\beta}(\bar{\nu}_\alpha \gamma^\mu P_L \nu_\beta)(\bar{f}\gamma_\mu P f), \tag{1.6.1}$$

$$\mathcal{L}_{CC} = -2\sqrt{2}G_F \sum_{f,P,\alpha,\beta} \varepsilon^{f,P}_{\alpha,\beta}(\bar{\nu}_\alpha \gamma^\mu P_L l_\beta)(\bar{f}\gamma_\mu P f'), \tag{1.6.2}$$

where G_F is the Fermi constant and ε matrix quantify the effect of new interactions relative to the weak scale. f and f' ($\in \{e, u, d\}$) are the matter fermions and $P \in \{P_L, P_R\}$ are the chirality projection operators. The production is affected by the CC NSIs and both the CC and NC NSIs can affect the detection of neutrinos in the detector. On the other hand, any NC NSIs will affect the neutrino propagation through matter. In general, NSIs can alter standard measurements like mass hierarchy, CP or octant of long-baseline experiments. Therefore, we need to constrain the NSIs parameters so that we can measure those parameters accurately. In chapter 5, we consider the effect of different beam tunes of DUNE to constrain the NSIs parameters.

Non Unitarity of Leptonic Mixing Matrix

Non unitarity of the leptonic mixing matrix is the another departure from the standard three neutrino hypothesis. In several extensions of the standard model, neutral heavy leptons (NHL) could arise naturally. For example, in type I see-saw models [61], we need heavy right handed neutrinos to produce small active neutrino masses. Due to the mass mixing between heavy and light flavor states, as in Eq. 1.4.7, we need a bigger matrix (V as in Eq. 1.4.13) to diagonalize the mass matrix M of Eq. 1.4.8. The full matrix V of dimension $3 + N_s$ is unitary but its 3×3 sub-block matrix (*i.e.* $1 - \frac{1}{2} M^{D^\dagger}(M^R M^{R^\dagger})^{-1} M^D$) is non unitarity. There are other variants of the see-saw mechanism, like the inverse see-saw [31, 32], where we introduce small lepton number violating mass terms which help to produce small neutrino mass naturally without very heavy right handed neutrinos as opposed to the type I see-saw. The inverse see-saw can produce sizeable non unitarity of the lepton mixing matrix [62, 63]. More generally, non unitarity of the leptonic mixing matrix may arise due to the effect of new physics at both high and low energy scales. In the high energy scenario, the non unitarity is because of the mixing of heavy right-handed neutrinos which are kinematically forbidden in neutrino oscillation experiments. On the other hand, if there are light sterile neutrinos of mass squared difference ~ 1 eV^2, then due to mixing the 3×3 leptonic mixing matrix becomes non unitarity and the sterile states are kinematically accessible in neutrino oscillations. In chapter 3, we will compare non unitarity coming from both heavy and light sterile neutrinos and we discuss the capabilities of future experiments to constrain the non unitarity parameter space. In chapter 4, we show how the mass hierarchy measurements will be hampered in the presence of leptonic non unitarity.

Other new physics like neutrino decay, neutrino decoherence, CPT violation/Lorentz violation etc. can also affect the neutrino oscillations and can be constrained by present and future neutrino experiments.

1.7 An overview of the thesis

Neutrino physics has entered the era of into the precision measurements. Present and future long-baseline experiments will able to measure standard neutrino oscillations parameters with increased precision and will also be able to point the presence of new physics in the neutrino sector. This thesis addresses the capabilities of long-baseline experiments (such as DUNE, T2HK, NOνA and T2K) to constrain new physics scenarios and studies the effect of new physics in the measurements of standard oscillations parameters.

Chapter 2 discusses what neutral current measurements can reveal. NC events depend on the total number of active flavors present in the beam. Therefore the presence of one extra light sterile neutrino will reduce the NC events. This allows us to constrain light sterile neutrino mixing parameters. We can also distinguish between new physics scenarios that violate three flavour unitarity and those which do not.

In chapter 3, we discuss the potential of DUNE and T2HK to constrin the non unitarity of the leptonic mixing matrix using CC and NC measurements. The synergy between CC and NC will provide better bounds on the non unitarity parameters. We also compare the non unitarity coming from both heavy and light sterile neutrinos and show that the NC events for both cases will not remain same in the leading order, unlike CC events.

In chapter 4, we discuss the effect of non unitarity on the mass hierarchy determination at DUNE, NOνA and T2K. We find that in the presence of non unitarity, the capability of those experiments to determine the mass hierarchy will be reduced significantly.

In chapter 5, we consider different beam tunes available at DUNE to constrain non-standard interactions. The combination of low and high energy beams will help to constrain some of the non-standard parameters (*e.g.* $\varepsilon_{e\mu}$) more effectively.

Chapter 2

What measurements of neutrino neutral current events can reveal

The major goals of present-day and near-future neutrino oscillation experiments are: a) the determination of the neutrino mass hierarchy (MH) and b) the discovery and possible measurement of the magnitude of CP violation (CPV) in the lepton sector. In addition, ancillary goals include making increasingly precise determinations of neutrino mass-squared differences, $\delta m_{ij}^2 = m_i^2 - m_j^2$ (i, j = 1, 2, 3 & $i \neq j$) and mixing angles θ_{ij}. Recent status reviews may be found in [64–66].

The capability for increased precision in neutrino experiments has recently led to the formulation of another important line of inquiry: the search for new physics at neutrino detectors, and its identification and disentanglement from physics related to the standard model with three generations of massive neutrinos. It is the purpose of this work to bring out facets of NC measurements at neutrino detectors that can aid in furthering efforts in this direction either on their own or when employed in synergy with other measurements.

Most investigations for new physics at long or short baseline neutrino experiments have focussed on measurements made using the CC channels, with either $\nu_\mu \to \nu_e$ or $\nu_\mu \to \nu_\mu$ as the underlying probabilities, and a final state electron or muon respectively. Our purpose in this chapter is to study the potential of neutrino NC events at such experiments to provide a tool to investigate features of new physics scenarios. This category of neutrino interactions in a typical detector fed by a neutrino beam generated in an accelerator facility can comprise neutrino-nucleon and neutrino-electron elastic scattering, neutrino deep-inelastic scattering, neutrino-nucleon resonant scattering with a pion in the final state, and finally, neutrino coherent pion scattering[1]. Similar processes exist, of course, for anti-neutrinos. The relative contributions from these various channels depend on the detector medium, the cross section and the energy of the beam, among other things.

As we shall show in the remainder of the chapter, the measurement and study of NC events can in some cases provide a qualitatively different, complementary and statistically superior handle on neutrino properties in new physics scenarios compared to CC measurements. Even when making measurements without the presumption of any new physics, these differences and complementarity can be useful. To see this, we consider Fig. 2.1, which assumes the 3+0 scenario. This figure shows, in the left panel, the full 3σ allowed possible band of CC electron events at the DUNE far detector given our present knowledge of three generation neutrino parameters[2]. The hierarchy is treated as being unknown, and the mixing angles and the CP phase are varied in their presently allowed ranges. Clearly, any measurement by DUNE in this large band is currently acceptable as being consistent with the standard model with massive neutrinos, given the present three flavour parameter ranges. The right panel shows the NC events for the same parameter variations[3]. Besides the superior statistics, we note the lack of any dependence on the parameter uncertainties. The reason for this is, of course, the fact that the NC rate is

[1]NC resonant pion scattering in DUNE can comprise the processes $\nu_\mu p \rightarrow \nu_\mu p\pi^0(n\pi^+)$ and $\nu_\mu n \rightarrow \nu_\mu n\pi^0(p\pi^-)$. NC coherent pion scattering from a target nucleus A is the process $\nu_\mu A \rightarrow \nu_\mu A\pi^0$.

[2] Throughout this work, we have used the GLoBES software package [67, 68] along with the snu.c routine [69, 70] to generate probability, events, and to do $\Delta\chi^2$-level analyses.

[3]As explained in Sec. 2.2, we use migration matrices provided to us by Michel Sorel to relate reconstructed visible energy in NC events in DUNE to true energy. We note that in the reconstructed energy spectrum in Fig. 2.1, and also later in the chapter in the right panel of Fig. 2.7, there is a small but somewhat surprising dip between 200 and 300 MeV. We thank Dr. Sorel for checking that this dip is indeed produced by the migration matrices. Since these matrices incorporate many physics details, it is difficult to pin down the origin of the dip more precisely. However, our conclusions are not affected by this dip.

insensitive to any flavour oscillations given the universality of weak interactions. A significant deviation from the rate shown, if detected, would clearly indicate the presence of certain kinds of new physics (as we discuss later in the chapter), as opposed to the CC rate which is encumbered by significant uncertainty as well as the possibility of degeneracy between new and standard physics.

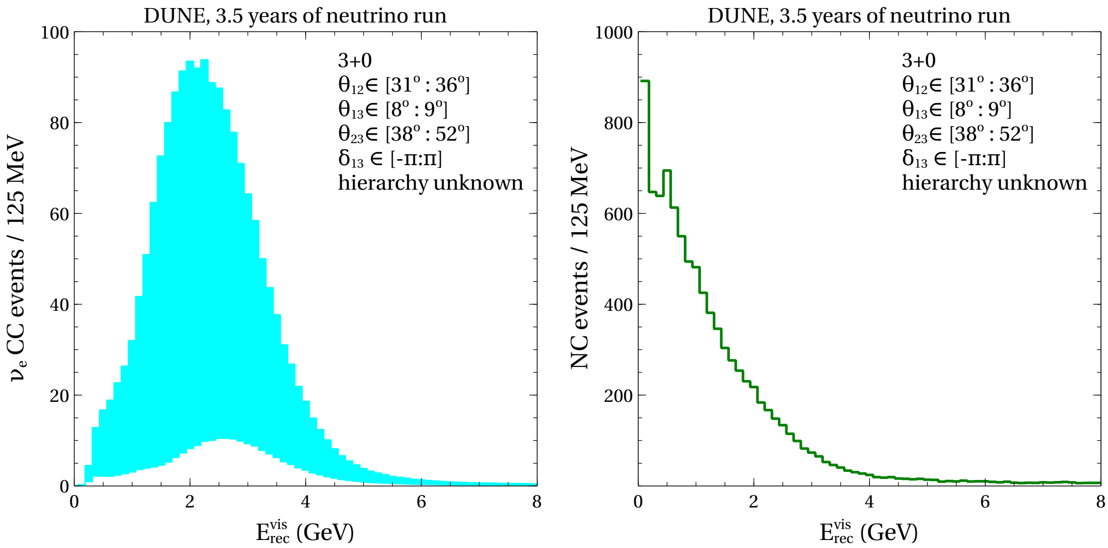

Figure 2.1: The left and right panel correspond to ν_e CC and NC events respectively. Here, all parameters are varied in their currently allowed range. E^{vis}_{rec} represents the reconstructed visible energy of the events in the detector. In the case of CC events, it closely matches the true energy of the incoming neutrino. For the NC events, E^{vis}_{rec} can be very different from the true incoming neutrino energy, as we discuss later.

In subsequent sections, we first emphasise and bring out a general property of CC versus NC event measurements which can be useful in new physics settings with CP violation at both long and short baselines. We show, in a general way, that NC and CC measurements complement each other in providing information on CP phases and mixing angles. Then, using the 3+1 scenario[4] at DUNE as an exemplar, we derive an approximate analytic expression for the probability governing NC event rates in vacuum , and discuss its features. We find that the effects of matter on NC event rates are small, allowing us to use the vacuum expression to good effect.

[4]This is dictated less by a belief in the veracity of 3+1 as nature's choice of physics beyond the standard model and more by the fact that it offers a simple template enabling us to bring out features and draw conclusions which may have applicability to other more complex new physics scenarios. Indeed, recent constraints restrict the allowed 3+1 parameter space significantly, as we discuss in Sec. 2.2.

We find that NC measurements can be revealing in several ways; for instance, we show that some CP-violating phase combinations lead to significant effects on the neutrino and anti-neutrino NC probabilities, although not to a significant CP-violating difference between them. Nevertheless, we find that under some circumstances there is good sensitivity to these phases. We provide bi-probability plots of neutrino versus anti-neutrino NC probabilities for fixed mixing angles to show that the CP phases can have substantial effects. We discuss how NC events break the degeneracy present in CC events, allowing us to discriminate new physics associated with new sterile states from that associated with non-standard interactions in neutrino propagation. We identify the general category of new physics scenarios which lend themselves to such degeneracy breaking via NC events. Using the 3+1 scenario as an example, we show the efficacy of NC events in constraining parameters and discuss how they can help improve existing bounds.

Finally, it bears noting that since all three flavours contribute, NC event measurements are typically statistically rich. For instance, in the Deep Underground Neutrino Experiment (DUNE), a 7-ton fine-grained tracking near detector at $\sim$ 500 m is planned, and it is expected to detect in excess of 400000 NC current events in a year [71]. Similar considerations would hold for the planned Short-Baseline Neutrino (SBN) program at Fermilab [72, 73]. Even at long baselines, NC events are typically very high in number compared to ν_e ($\bar{\nu}_e$) measured CC channel, which buttresses the significance of any conclusions based on their measurement.

2.1 Neutral current events in new physics scenarios with CP violation: a general property

This section identifies a salient property of the NC probability, P_{NC}, defined as $\Sigma_\beta P_{\nu_\alpha \to \nu_\beta}$, $\alpha, \beta = e, \mu, \tau$ for a given neutrino source beam of flavour α and an assumed physics scenario, which will actively contribute to the measured NC rate. In the standard $3+0$

scenario, for instance, given a source beam of primarily muon neutrinos and the universality of weak interactions, $P_{NC} = P_{\mu e} + P_{\mu\tau} + P_{\mu\mu} = 1$. For the same source beam, but an assumed 3+1 scenario, $P_{NC} = 1 - P_{\mu s} = P_{\mu e} + P_{\mu\tau} + P_{\mu\mu} \neq 1$, where s denotes the sterile flavour. This section is focussed on bringing out a feature of NC events that is generic to new physics scenarios with CP violation, assuming a 3+2[5] scenario at a short baseline as an example.

In general, useful conclusions regarding the properties of P_{NC} can be drawn by examining analytic expressions and comparing them to expressions for their corresponding CC counterparts, *e.g.* $P_{\mu e}$. We begin by writing down a general expression for the flavour oscillation probability in vacuum,

$$\begin{aligned} P_{\nu_\alpha \to \nu_\beta} &= \delta_{\alpha\beta} - 4Re \sum_{k>j} (U^*_{\alpha k} U_{\beta k} U_{\alpha j} U^*_{\beta j}) \sin^2 \Delta_{kj} \\ &+ 2Im \sum_{k>j} (U^*_{\alpha k} U_{\beta k} U_{\alpha j} U^*_{\beta j}) \sin 2\Delta_{kj}. \end{aligned} \tag{2.1.1}$$

Here k, j run over the mass eigenstates, wheras α, β denote flavours. Additionally, $\Delta_{kj} = 1.27 \times \delta m^2_{kj} [\mathrm{eV}^2] \times L[km]/E[GeV]$ where L is the baseline length and E is the neutrino energy. Eq. 2.1.1 is valid for any number of flavours (including sterile ones, if present).

Consider an experiment sourced by an accelerator generated ν_μ beam, and a 3+2 scenario, with two additional sterile flavour states ν_{s_1} and ν_{s_2}, and mass eigenstates ν_4 and ν_5. From Eq 2.1.1, we see that the CP violating part of $P_{\mu s_1}$ resides in

$$\begin{aligned} P^{CP}_{\mu s_1} &\propto Im \sum_{k>j} (U^*_{\mu k} U_{s_1 k} U_{\mu j} U^*_{s_1 j}) \sin 2\Delta_{kj} \\ &\simeq Im[U^*_{\mu 5} U_{s_1 5} (U_{\mu 4} U^*_{s_1 4} \sin 2\Delta_{54} + U_{\mu 3} U^*_{s_1 3} \sin 2\Delta_{53} + U_{\mu 2} U^*_{s_1 2} \sin 2\Delta_{52} + U_{\mu 1} U^*_{s_1 1} \sin 2\Delta_{51}) \\ &+ U^*_{\mu 4} U_{s_1 4} (U_{\mu 3} U^*_{s_1 3} \sin 2\Delta_{43} + U_{\mu 2} U^*_{s_1 2} \sin 2\Delta_{42} + U_{\mu 1} U^*_{s_1 1} \sin 2\Delta_{41}) \\ &+ U^*_{\mu 3} U_{s_1 3} (U_{\mu 2} U^*_{s_1 2} \sin 2\Delta_{32} + U_{\mu 1} U^*_{s_1 1} \sin 2\Delta_{31}) + U^*_{\mu 2} U_{s_1 2} (U_{\mu 1} U^*_{s_1 1} \sin 2\Delta_{21})] \end{aligned} \tag{2.1.2}$$

[5]Note that 3+2 scenario is highly disfavored from cosmology.

A similar expression can be written down for $P^{CP}_{\mu s_2}$ with s_1 replaced by s_2 everywhere, leading to

$$P_{NC} = 1 - P_{\mu s_1} - P_{\mu s_2}.$$

For a short baseline (SBL) experiment, the terms proportional to $\sin 2\Delta_{ij}$, with $i, j = 1, 2, 3$ can be dropped in comparison to the others, and $P_{\mu s_{1,2}}$ simplify; for instance,

$$\begin{aligned} P^{CP}_{\mu s_1} &\simeq Im[U^*_{\mu 5} U_{s_1 5} (U_{\mu 4} U^*_{s_1 4} \sin 2\Delta_{54} \\ &+ U_{\mu 3} U^*_{s_1 3} \sin 2\Delta_{53} + U_{\mu 2} U^*_{s_1 2} \sin 2\Delta_{52} + U_{\mu 1} U^*_{s_1 1} \sin 2\Delta_{51}) \\ &+ U^*_{\mu 4} U_{s_1 4} (U_{\mu 3} U^*_{s_1 3} \sin 2\Delta_{43} + U_{\mu 2} U^*_{s_1 2} \sin 2\Delta_{42} + U_{\mu 1} U^*_{s_1 1} \sin 2\Delta_{41})]. \end{aligned} \tag{2.1.3}$$

For this scenario, the CP violating part of the CC probability, under the same approximation as Eq. 2.1.3, is proportional to

$$\begin{aligned} P^{CP}_{\mu e} &\propto Im \sum_{k>j} (U^*_{\mu k} U_{ek} U_{\mu j} U^*_{ej}) \sin 2\Delta_{kj} \\ &\simeq Im[U^*_{\mu 5} U_{e5} (U_{\mu 4} U^*_{e4} \sin 2\Delta_{54} + U_{\mu 3} U^*_{e3} \sin 2\Delta_{53} + U_{\mu 2} U^*_{e2} \sin 2\Delta_{52} + U_{\mu 1} U^*_{e1} \sin 2\Delta_{51}) \\ &+ U^*_{\mu 4} U_{e4} (U_{\mu 3} U^*_{e3} \sin 2\Delta_{43} + U_{\mu 2} U^*_{e2} \sin 2\Delta_{42} + U_{\mu 1} U^*_{e1} \sin 2\Delta_{41})]. \end{aligned} \tag{2.1.4}$$

In a scenario geared towards explaining the short baseline anomalies [49, 53, 74–76], further simplifications are possible, *e.g.* $\delta m^2_{lm} >> \delta m^2_{mn}$, $l = 4$ or $l = 5$, $m, n = 1, 2, 3$ [6]. After a little algebra, one then finds that the CP violating difference between NC events measured using an initially muon-flavoured neutrino beam, and those measured using its anti-neutrino counterpart, will be proportional to the quantity D_{NC}, given by

$$D_{NC} \propto Im[U^*_{\mu 5} U_{\mu 4} (U_{s_1 5} U^*_{s_1 4} + U_{s_2 5} U^*_{s_2 4})] \sin \Delta_{54} \sin \Delta_{43} \sin \Delta_{53}. \tag{2.1.5}$$

[6] We stress that the general conclusion we draw in this section remains unchanged with or without such simplifications.

On the other hand, the analogous difference for CC events from $\nu_\mu \to \nu_e$ transitions is proportional to

$$D_{CC} \quad \propto \quad Im[U^*_{\mu 5} U_{\mu 4} U_{e5} U^*_{e4}] \sin \varDelta_{54} \sin \varDelta_{43} \sin \varDelta_{53}. \tag{2.1.6}$$

Comparing Eq. 2.1.3 with Eq. 2.1.4 and Eq. 2.1.5 with Eq. 2.1.6, we see that in both cases they tap into different CP phases and sectors of the mixing matrix. Consequently, the NC measurements will provide a qualitatively and quantitatively different window into the CP violating and mixing sectors of a new physics scenario compared to the CC measurements. Should a new physics scenario with CP violation be nature's choice, then combining NC measurements with CC measurements would provide a valuable way to probe it.

2.2 Neutral current and new physics at long baselines

For the remainder of this chapter, we focus largely, but not exclusively, on the 3+1 scenario in order to study the potential of NC events as a probe and diagnostic tool for new physics.

Additionally, we perform our calculations for the DUNE far detector. DUNE [71] is a proposed future super-beam experiment with the main aim of establishing or refuting the existence of CPV in the leptonic sector. In addition to this primary goal, this facility will also be able to resolve the other important issues like the mass hierarchy and the octant of θ_{23}. The $\nu_\mu(\bar{\nu}_\mu)$ super-beam will originate at the Fermilab. The optimised beam simulation assumes a 1.07 MW - 80 GeV proton beam which will deliver 1.47×10^{21} protons-on-target (POT) per year. A 40 kt Liquid Argon (LAr) far-detector will be placed in the Homestake mine in South Dakota, 1300 km away. The experiment plans to have a total of 7 years of running, divided equally between neutrinos and anti-neutrinos, corresponding to a total exposure of 4.12×10^{23} kt-POT-yr. The complete experimental description of the DUNE experiment such as the CC signal and background definitions as well as assumptions on the detector efficiencies concerning the CC events are from [77]. The details regarding the anticipated NC events at DUNE were taken from [78]. The NC event detection efficiency has been assumed to be 90%. In order to correctly reproduce the NC events spectra, we have made use of the *migration matrices*. In a NC event, the outgoing (anti-)neutrino carries away some fraction of the incoming energy. This energy is missed and hence, the reconstructed visible energy is less than the total incoming energy. As such, the events due to energetic (anti-)neutrinos are reconstructed inaccurately at lower visible energies in a majority of such cases[7]. Therefore, using a gaussian energy resolution function in such a situation is not appropriate. We have used the migration matrices from [79], provided to us by [80]. Note that these migration matrices correspond to a binning of 50 MeV and therefore, in this work too, we have considered the energy bins of 50 MeV for NC events[8]. For the analysis of CC events, we have used energy bins of 125 MeV as in [77]. The background to NC events consists of CC events that get mis-identified as NC events. These include electron events (due to CC signal $\nu_\mu \to \nu_e$ or intrinsic beam $\nu_e \to \nu_e$), muon events ($\nu_\mu \to \nu_\mu$), tau events ($\nu_\mu \to \nu_\tau$) and their respective CP-reversed channels due to anti-neutrino/neutrino contaminations in the beam. It should be noted that the backgrounds too, will oscillate into the sterile flavour depending on the values of U_{e4}, $U_{\mu4}$ and $U_{\tau4}$. In such a scenario, the simplifying assumptions of putting one or more of these matrix elements to 0, *may not* give the correct estimate of the NC signal events. For the NC analysis, the signal and background normalisation errors have been taken to be 5% and 10% respectively.

Finally, we note that in the 3+1 scenario, flavor oscillations may lead to some depletion of the active neutrino flux and of its muon neutrino component at the location of the DUNE near detector ($\sim$ 500 m). This could, in principle, distort the flux measurement made at this location, which forms the basis of conclusions drawn regarding oscillations measured

[7]The profile of NC events spectrum, for example, can be seen in the right panel of Fig. 2.1.

[8]For the sake of clarity, we show NC events in Figs. 2.1 and 2.7 in energy bins of 125 MeV. However, for binned-$\Delta\chi^2$ calculations, we have considered 50 MeV energy bins.

at the far detector. We have assumed an overall error of 5% in flux measurements, and have checked that given the currently allowed parameter ranges for the 3+1 scenario, the change in flux due to a sterile species is always below this limit. On the other hand, as we show in this work, depletion in the NC rate significantly above this uncertainty is expected at the far detector, hence enabling DUNE to detect the possible presence of a sterile state via neutral current measurements.

2.2.1 An approximate analytical expression for $P_{\mu s}$

As mentioned above, the NC rate in a 3 + 1 scenario will be proportional to $1 - P_{\mu s}$. We give below a useful approximate expression, starting from Eq. 2.1.1, since the full expression which follows from it is extremely long and complicated. In obtaining this approximate form, we have adopted the following parameterisation for the PMNS matrix:

$$U^{3+1}_{\rm PMNS} = O(\theta_{34}, \delta_{34}) O(\theta_{24}, \delta_{24}) O(\theta_{14}) O(\theta_{23}) O(\theta_{13}, \delta_{13}) O(\theta_{12}) \tag{2.2.1}$$

Here, in general, $O(\theta_{ij}, \delta_{ij})$ is a rotation matrix in the ij sector with associated phase δ_{ij}. For example,

$$O(\theta_{24}, \delta_{24}) = \begin{pmatrix} 1 & 0 & 0 & 0 \\ 0 & \cos\theta_{24} & 0 & e^{-i\delta_{24}} \sin\theta_{24} \\ 0 & 0 & 1 & 0 \\ 0 & -e^{i\delta_{24}} \sin\theta_{24} & 0 & \cos\theta_{24} \end{pmatrix}; \; O(\theta_{14}) = \begin{pmatrix} \cos\theta_{14} & 0 & 0 & \sin\theta_{14} \\ 0 & 1 & 0 & 0 \\ 0 & 0 & 1 & 0 \\ -\sin\theta_{14} & 0 & 0 & \cos\theta_{14} \end{pmatrix} etc.$$

Measurements from MINOS, MINOS+, Daya Bay and the IceCube experiments provide significant constraints on the 3+1 paradigm. See, for instance, [81–83]. The Super-

Kamiokande data, MINOS NC data, NOνA NC data and the IceCube-DeepCore data provide constraints on the 3-4 mixing [84–87]. Our work in this chapter utilises only the currently allowed parameter space for this scenario as determined by these references[9]. Since these current constraints restrict $\theta_{13}, \theta_{14}, \theta_{24} \leq 13°$, we take $\sin^3\theta_{ij} = 0$, where θ_{ij} is any of these angles. We also set $\theta_{23} = 45°$ for simplicity, and assume $\sin^2\frac{\Delta m^2_{31}L}{4E} = \sin^2\frac{\Delta m^2_{32}L}{4E}$, while neglecting the contribution from the solar mass-squared difference, since $\Delta m^2_{21} << \Delta m^2_{31}$. Additionally, we work under the assumption that the mass-squared differences δm^2_{lm}, $l = 4$, $m = 1, 2, 3$ are all approximately equal, implying that the fourth mass eigenstate is much heavier than the other three. With these simplifications, we obtain, for the vacuum transition probability for ν_μ to ν_s,

$$
\begin{aligned}
\mathrm{P}^{\mathrm{vac}}_{\mu s} \simeq\ & \cos^4\theta_{14}\cos^2\theta_{34}\sin^2 2\theta_{24}\sin^2\frac{\Delta m^2_{41}L}{4E} \\
+\ & \Big[\cos^4\theta_{13}\cos^2\theta_{24}\sin^2\theta_{34} - \cos^2\theta_{13}\cos^2\theta_{24}\cos^2\theta_{34}\sin^2\theta_{24} \\
+\ & \frac{1}{\sqrt{2}}\sin 2\theta_{13}\sin 2\theta_{34}\sin\theta_{14}\cos^3\theta_{24}\cos(\delta_{13}+\delta_{34})\Big]\sin^2\frac{\Delta m^2_{31}L}{4E} \\
+\ & \frac{1}{2}\cos^2\theta_{13}\cos^2\theta_{24}\sin 2\theta_{34}\sin\theta_{24}\sin(\delta_{34}-\delta_{24})\sin\frac{\Delta m^2_{31}L}{2E}.
\end{aligned}
\tag{2.2.2}
$$

Prior to testing the accuracy of this formula and determining its applicability, we note the following characteristics:

1. The first term is, in its exact form, a rapidly oscillating term due to the large mass-squared difference. In the plots to follow, for specificity, we assume it to be $\simeq 1$ eV^2, and adopt the DUNE baseline of 1300 km.

2. Of the three phases, only two linear combinations appear: $\delta_1 = \delta_{13} + \delta_{34}$ and $\delta_2 = \delta_{34} - \delta_{24}$; and only the latter is responsible for CP violation in neutral currents.

[9] It should be noted that there are global analyses of the existing oscillation data that provide constraints on the 3+1 paradigm [55, 88, 89]. However, there exist differences in their results corresponding to the fits in the parameter space $\Delta m^2_{41} - \sin^2\theta_{34}$. There is also the difficulty in reconciling the appearance data with the disappearance data. Keeping these points in mind, we adhere to the constraints on 3+1 from the disappearance data from the above-mentioned standalone experiments.

It follows that these simplifications and characteristics percolate into $P_{NC} = 1 - P_{\mu s}$, which we now plot in Fig. 2.2.

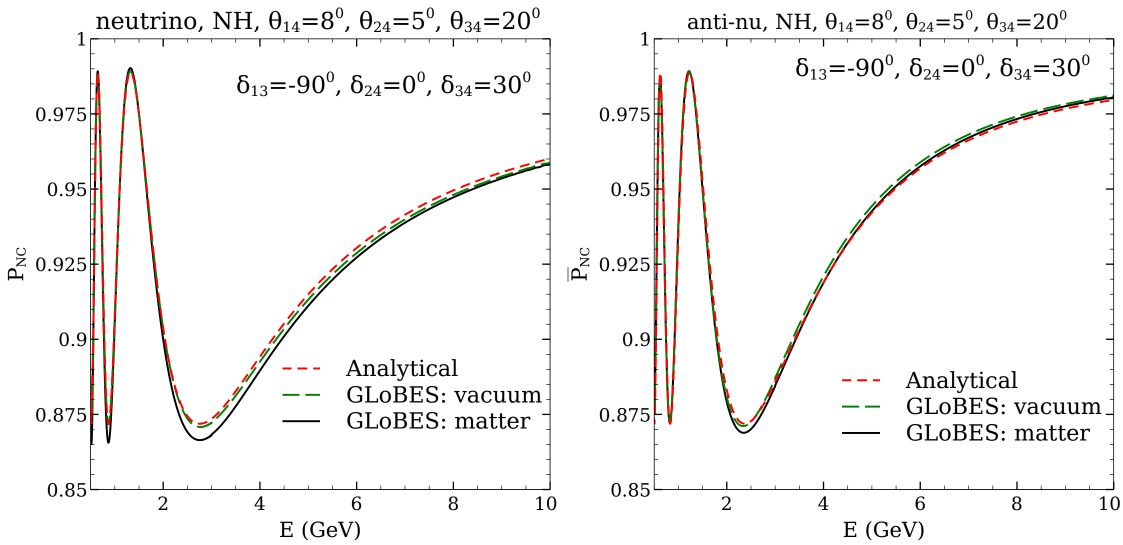

Figure 2.2: Probability plots , comparing $P_{NC} = 1 - P_{\mu s}$ using the approximate formula for $P_{\mu s}$given in the text, Eq. 2.2.2 (red dashed curves) with the full GLoBES result in vacuum (green dashed curves) and matter (black solid curves). The left panel is for neutrinos and the right one for anti-neutrinos. Choices of phases and mixing angles have been made as shown. The curves correspond to $L = 1300$ km.

We see that there is good agreement between the exact GLoBES curves (solid black and dashed green lines) and the ones generated by the analytical approximation (red dashed line). The curves show no rapid oscillations since the small wavelength oscillation part of first term in $P_{\mu s}$ is averaged out to 0.5.

From Fig. 2.2 we see that the approximate formula, derived for the vacuum case, also works well for matter, *i.e.* the overall matter effect in NC event rates is small. Some understanding of this feature can be gleaned from Fig 2.3, which shows full GLoBES curves for the various probabilities, and demonstrates how the $\nu_\mu \to \nu_e$ and $\nu_\mu \to \nu_\tau$ channels have matter effects that are already small in each of these channels, and that nearly cancel each other over the DUNE energy range and baseline. While we certainly cannot generalise this over baselines, energies and new physics scenarios, we note that such a near cancellation can occur for a range of baselines and energies in the 3+0 scenario[10].

[10]For a fuller discussion of the 3+0 case see [90].

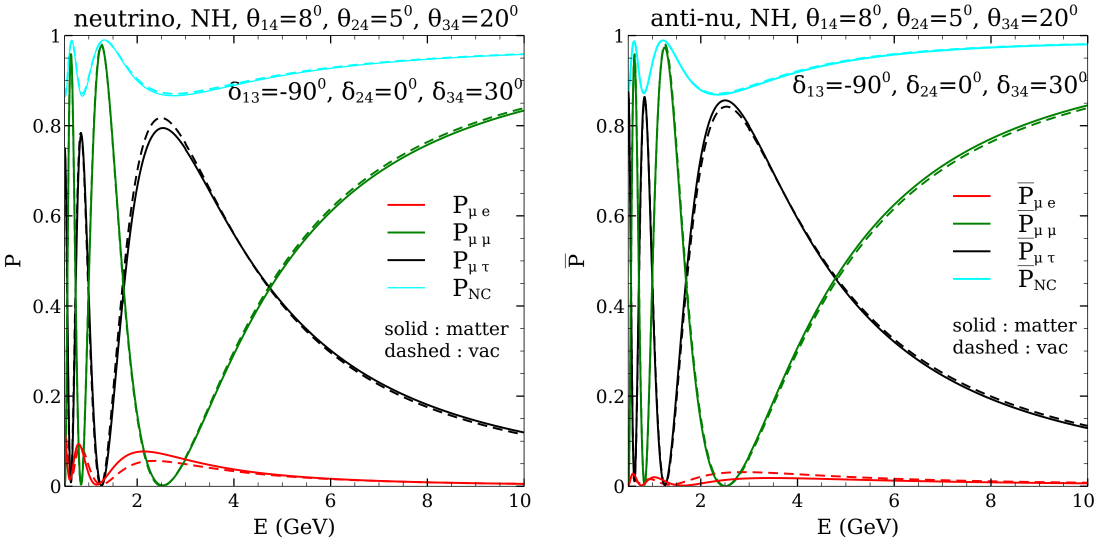

Figure 2.3: Probability plots , comparing $P_{\mu e}, P_{\mu\tau}, P_{\mu\mu}$ and $P_{NC} = 1 - P_{\mu s}$, all for the 3+1 model, using GLoBES. The left panel is for neutrinos and the right one for anti-neutrinos, and solid curves are for matter while the dashed ones are for vacuum. Choices of phases and mixing angles have been made as shown. The curves correspond to $L = 1300$ km.

Finally, we note that the NC probabilities for neutrinos and anti-neutrinos are very similar with the the approximate formula, as a comparison of the left and right panels in Figs. 2.2 and 2.3 demonstrate.

2.2.2 Effect of the CP violating phases on P_{NC}

This section attempts to understand the dependence of P_{NC} on the three CP violating phases δ_{13}, δ_{24} and δ_{34} in a simple way.

In Fig. 2.4 we have plotted the $P_{NC} = 1 - P_{\mu s}$ as a function of the Energy (GeV) in the presence of matter for $L = 1300$ km. The plots correspond to normal hierarchy, $\theta_{14} = 8°$, $\theta_{24} = 5°$ and $\theta_{34} = 20°$. The solid curves show the probability values for neutrinos while the dashed ones are for anti-neutrinos. In the left panel we show the dependence of P_{NC} on the δ_{13} phase. For this panel, we show curves corresponding to $\delta_{13} = -180°, -90°, 0$ and $90°$. The other two phases δ_{24} and δ_{34} have been set to 0. In the right panel, we show the dependence of P_{NC} on the δ_{13} and δ_{34} phases with the δ_{24} phase kept equal to 0. We show four set of curves for both neutrinos and anti-neutrinos

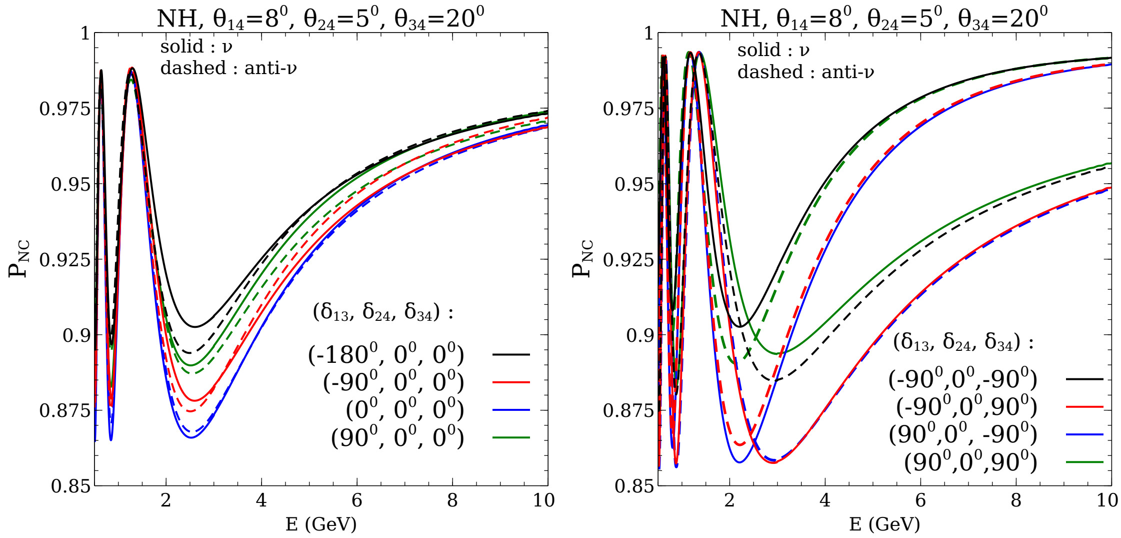

Figure 2.4: P_{NC} vs Energy (in GeV) assuming normal hierarchy for L = 1300 km in the presence of matter. $\theta_{14} = 8°, \theta_{24} = 5°, \theta_{34} = 20°$ (fixed). The solid (dashed) curves are for neutrino (anti-neutrino). Left panel: $\delta_{13} \in \{-180°, -90°, 0, 90°\}$, $\delta_{24} = \delta_{34} = 0$. Right panel: $\delta_{13}, \delta_{34} \in \{\pm 90°, \pm 90°\}$ and $\delta_{24} = 0$ as shown in the key.

corresponding to $\delta_{13}, \delta_{34} \in \{\pm 90°, \pm 90°\}$. From Fig. 2.4, we can draw the following conclusions:

- P_{NC} has significant dependence on the CP phases δ_{13} and δ_{34}.
- The left panel shows that the differences between neutrino and anti-neutrino probabilities are small. However, there is appreciable separation between the $\delta_{13} = 0, -180°$ and $\delta_{13} = -90°, 90°$curves. This can be understood from Eq. 2.2.2 where the δ_{13}-dependence is through a cosine term.
- In the right panel, the introduction of the δ_{34} phase induces larger differences between the neutrino and anti-neutrino probabilities, specially at higher energies. Referring to Eq. 2.2.2, we see that as the energy increases, the CP violating term will tend to undergo less suppression compared to the other terms, hence its effect tends to become more visible. Thus, the measurement of a large CP-asymmetry in the NC events at DUNE can point to a CP-violating value of δ_{34}[11].
- In the right panel, for neutrinos, while the peaks for all curves have about the same

[11]Or, more accurately, a CP-violating value of $\delta_2 = \delta_{34} - \delta_{24}$, as we emphasise below.

value of P_{NC}, among the minima, the lowest value of P_{NC} occurs for $(\delta_{13}, \delta_{34})$ values around $(-90°, 90°)$ while the highest value occurs for $(\delta_{13}, \delta_{34})$ values around $(-90°, -90°)$. For anti-neutrinos, again, examining minima, the lowest value of P_{NC} occurs for $(\delta_{13}, \delta_{34})$ values around $(90°, -90°)$ while the highest value occurs for $(\delta_{13}, \delta_{34})$ values around $(90°, 90°)$. This again, is easy to understand from Eq. 2.2.2, where the CP dependence is of the form $A\cos(\delta_{13}+\delta_{34})+B\sin\delta_{34}$ for $\delta_{24} = 0$. Note that here we have shown the curves for restrictive values of δ_{13} and δ_{34}, but this behaviour is verified again in Fig. 2.6 in a more general way.

- It is also evident from the right panel of Fig. 2.4 that the probability curve for neutrino corresponding to $(\delta_{13}, \delta_{34})$ of let's say (x, y) where $x, y = \pm 90°$ is degenerate with the anti-neutrino curve of $(-x, -y)$, especially at higher and lower energies. Small differences due to matter effects can be seen near the minima. Neglecting these small matter effects, we see from the approximate expression for the vacuum oscillation probability, Eq. 2.2.2, that the degenerate probability curves should indeed be identical.

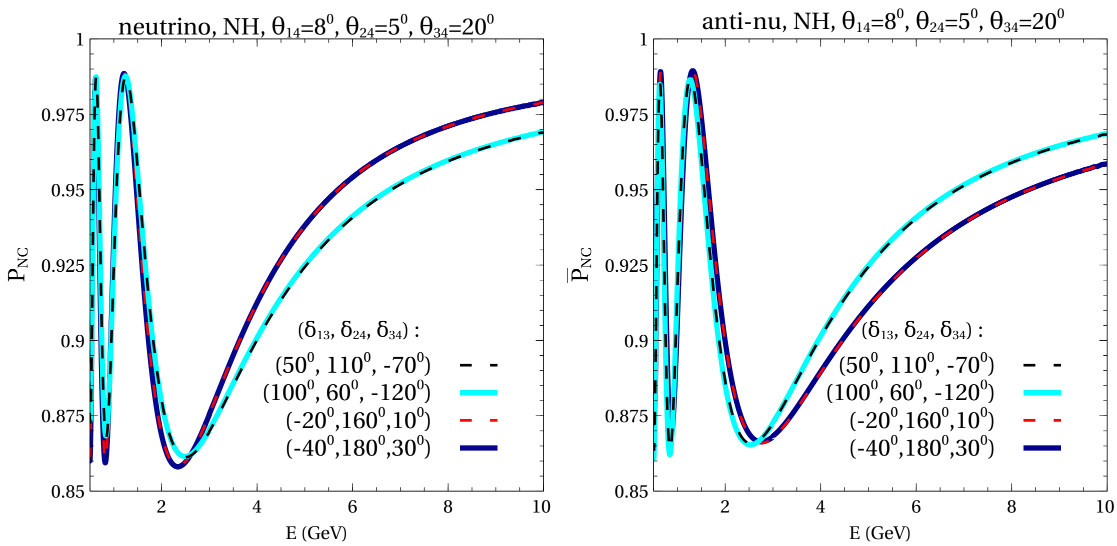

Figure 2.5: P_{NC} vs Energy (in GeV) assuming normal hierarchy for $L = 1300$ km in the presence of matter. $\theta_{14} = 8°, \theta_{24} = 5°, \theta_{34} = 20°$ (fixed). The left (right) panel corresponds to neutrino (anti-neutrino) probabilities. Different values of $\delta_{13}, \delta_{24}, \delta_{34}$ are chosen as shown in the key.

Under the approximations in which Eq. 2.2.2 is valid, it can be seen that there are only two effective CP phases that will play a role in P_{NC} at the leading order. These are $\delta_1 = \delta_{13}+\delta_{34}$ and $\delta_2 = \delta_{34} - \delta_{24}$. Thus, in our chosen parameterisation of the PMNS matrix, there is a degeneracy between the three CP phases. We show this explicitly in Fig. 2.5. We have plotted P_{NC} as a function of the energy for neutrinos (anti-neutrinos) in the left (right) panel. We choose two sets of different $(\delta_{13}, \delta_{24}, \delta_{34})$ values (as shown in the key in the figures) which give the same δ_1 and δ_2 values. The assumed values of the other oscillation parameters are same as Fig. 2.4. It can be seen that there is almost complete degeneracy between the curves corresponding to common values of the phases δ_1 and δ_2. Note that Eq. 2.2.2 is derived for vacuum, and for the special value $\theta_{23} = 45^o$. However the degeneracies hold true for matter probabilities at $L = 1300$ km and for other assumed values of θ_{23} within its allowed range.

It is therefore possible to set one of the phases equal to 0, without the loss of generality. Since, we have considered $\sin\theta_{24}$ to be a small quantity as its range of values is the most restricted, putting $\delta_{24} = 0$ may be the best choice in order to not have significant differences between vacuum and matter probabilities. We explore this in Fig. 2.6, generated using GLoBES. These plots show the values of probabilities in the P_{NC} - $\bar{P}_{NC}$ plane for different values of the oscillation parameters. In Fig. 2.6, we show results for normal hierarchy, $\theta_{14} = 8°$, $\theta_{24} = 5°$ and $\theta_{34} = 20°$. The left (right) panel corresponds to neutrino energy of 3 GeV (5 GeV). The green region shows the space in the $P_{NC} - \bar{P}_{NC}$ plane when all the three phases are varied in the range $[-180°, 180°]$. The red region corresponds to the space when δ_{13} and δ_{34} are varied in $[-180°, 180°]$, holding δ_{24} equal to 0. The four black points correspond to $\delta_{13}, \delta_{34} \in \{\pm 90°, \pm 90°\}$ when $\delta_{24} = 0$. From Fig. 2.6, we conclude that

- The fact that the red region is almost the same as the green region suggests that putting $\delta_{24} = 0$ does not lead to any loss of obtainable P_{NC} - $\bar{P}_{NC}$ space.
- The four black points - $\delta_{13}, \delta_{34} \in \{\pm 90°, \pm 90°\}$ indeed quite closely correspond to the δ_{13}, δ_{34} values for which the the P_{NC} and $\bar{P}_{NC}$ are minimum or maximum. This

is true for both 3 GeV and 5 GeV.

- The dependence on the δ_{13} and δ_{34} phases as expressed in Eq. 2.2.2 is reasonably accurate.

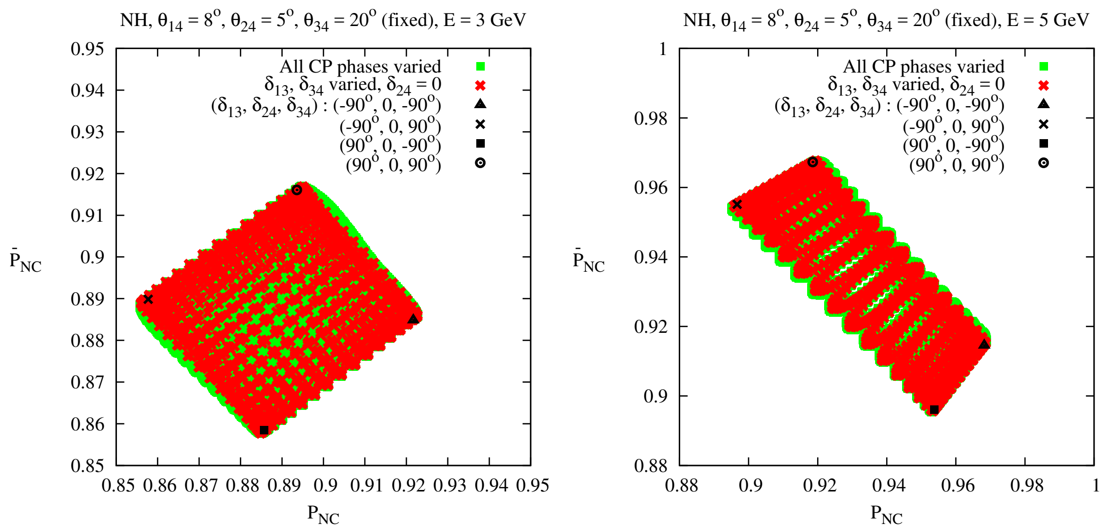

Figure 2.6: $\bar{P}_{NC}$ vs P_{NC} at $E = 3\ GeV$ (left-panel) and at $E = 5\ GeV$ (right-panel) for $L = 1300$ km in the presence of matter. $\theta_{14} = 8°, \theta_{24} = 5°, \theta_{34} = 20°$ (fixed). Green region: This region corresponds to all $\bar{P}_{NC}$ - P_{NC} values that are obtained when all the three CP phases are varied in $[-180°, 180°]$. Red region: This region corresponds to all $\bar{P}_{NC}$ - P_{NC} values that are obtained when δ_{13} and δ_{34} are varied in $[-180°, 180°]$ while $\delta_{24} = 0$. Black points: $\delta_{13}, \delta_{34} \in \{\pm 90°, \pm 90°\}$ when $\delta_{24} = 0$.

Finally, we point out that the situation above serves as another example of the point made in Section 2. The NC events for the long baseline of DUNE and the chosen 3+1 new physics scenario provide a window into CP violation via the phase combinations $\delta_1 = \delta_{13} + \delta_{34}$ and $\delta_2 = \delta_{34} - \delta_{24}$ both in vacuum and in matter. On the other hand, as discussed in [91], the CC probability $P_{\mu e}$ in matter for the same scenario is sensitive to all three CP phases[12], which leads to degeneracies. Thus NC measurements, with their high statistics, are an important complementary tool to probe CP violation and break degeneracies in new physics scenarios in conjunction with CC measurements.

[12]In vacuum, as discussed in [91], the CC probability has no sensitivity to δ_{34}.

2.3 Neutral current measurements as a tool to break BSM physics degeneracies

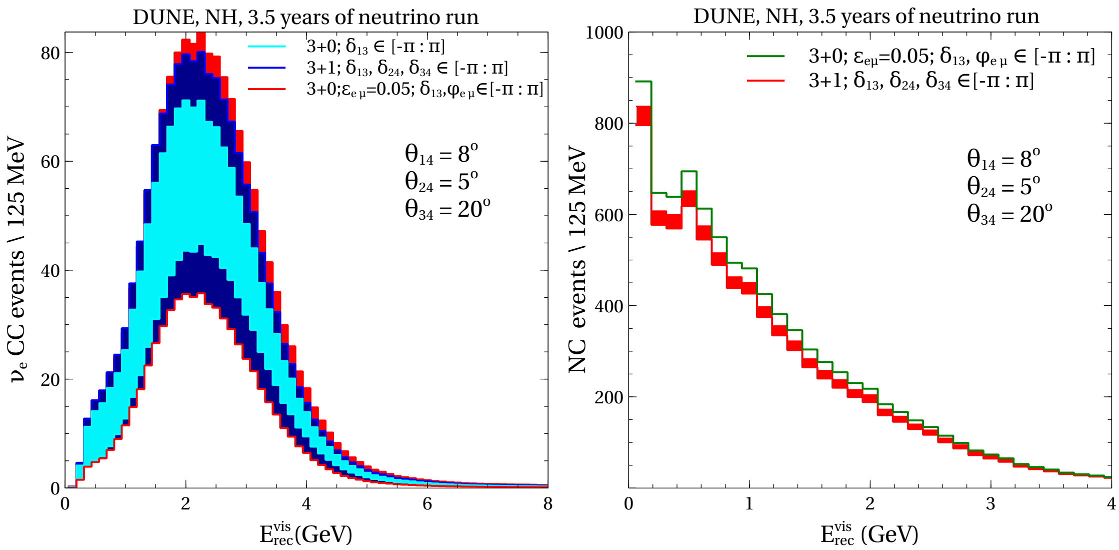

Figure 2.7: CC and NC events as a function of reconstructed neutrino energy in DUNE with 3.5 yrs of neutrino running. The left panel corresponds to ν_e CC events for two different new physics scenarios, as well as for the standard 3+0 paradigm. The green line and the red band in the right panel show NC neutrino events in the presence of propagation-related NSI, and in the presence of a sterile neutrino, respectively. In all cases the respective CP phases have been varied over their full range of $[-180°, +180°]$. In the case of NSIs, $A(\delta_{e\alpha}\delta_{e\beta} + \varepsilon_{\alpha\beta}e^{i\phi_{\alpha\beta}})$ $(\alpha, \beta = e, \mu, \tau)$ represents the matter term in the effective Hamiltonian in the presence of NSIs. Here, A is the Wolfenstein matter term and is given by $A(\mathrm{eV}^2) = 0.76 \times 10^{-4}\rho(g/cc)E(GeV)$, ρ being the matter density and E, the neutrino energy. The chosen example values of NSI and sterile parameters are shown in the key. The remaining NSI parameters are equal to 0.

In this section, we demonstrate the capability of NC events to break degeneracies which would otherwise arise in CC events, vis a vis new physics scenarios. While we choose propagation based non-standard interactions (NSI) and a 3+1 sterile scenario to demonstrate our point, our conclusion will hold for any two new physics settings, one of which does not break 3+0 unitarity (in this example, the propagation NSI) and another one which does (3+1 sterile). A similar conclusion would hold, for example, for NSI in propagation and neutrino decay, or NSI in propagation and NSI in production or detection (which inherently violate unitarity by adding to or depleting the source neutrino beam).

Both NSI arising during propagation and extra sterile neutrino states affect ν_e CC events. From Fig. 2.7 (left panel) we see that there is a wide range of possible spectra that can arise either from propagation NSI or an extra sterile neutrino state (3+1 scenario). Shown also is the standard 3+0 scenario band. NSI affect the individual transition probabilities but the total oscillation probability of all the active flavours remains unity. On the other hand, in the presence of extra sterile states, the total oscillation probability of the active flavours becomes less than unity, leading to a depletion in NC events in the presence of sterile states compared to propagation NSI (the right panel of Fig. 2.7). Thus, NC events break the degeneracy seen in the CC event spectrum. We expect around 9345 NC total signal events in the case of 3+0 (or with propagation NSI present) in DUNE for 3.5 years of neutrino run. With 3+1 and sterile oscillation parameters corresponding to the right panel of Fig. 2.7, this number will deplete to $\sim$ (8306 – 8804) depending on the true values of the CP violating phases. Thus, a 6% - 11% reduction in the total NC signal event rate is possible for $\theta_{34} \approx 20°$. We do quantitative analyses in Sec. 2.4, to show that with a reduction in NC rates of this size, DUNE can distinguish between the 3+0 (or propagation NSI) and the 3+1 scenarios at a 90% C.L.

We note that as the sterile parameters become small, the 3+1 and 3+0 scenarios merge and become indistinguishable. In other words, the red band in the right panel of Fig. 2.7 will tend to grow narrower and merge with the green solid line. Thus, the 3+1 parameters need to be such that a measurable difference in the NC rate can be attained.

2.4 Constraints on the 3+1 paradigm: Sensitivity forecasts with DUNE

In this section, we demonstrate the sensitivity of the DUNE experiment to exclude the 3+1 scenario using a combined analysis of NC and CC measurements. We assume a 40 kt Liquid Argon detector and 3.5 years each of neutrino and anti-neutrino running. We have used the optimised beam profile, as described earlier in Section 2.2. The CC and NC events due to such a beam have been shown in Figs. 2.1 and 2.7 . We simulate data assuming that 3+0 is the true case i.e. we put the mixing parameters $\Delta m^2_{41}, \theta_{14}, \theta_{24}, \theta_{34}, \delta_{24}$ and δ_{34} equal to 0. Note that in such a situation δ_{13} is $\delta_{\rm CP}$. We assume the hierarchy to be normal, $\theta_{12} = 33.48°$, $\theta_{13} = 8.5°$ and $\theta_{23} = 45°$. The mass-squared differences Δm^2_{21} and $|\Delta m^2_{31}|$ have been taken to be $7.5 \times 10^{-5}\mathrm{eV}^2$ and $2.45 \times 10^{-3}\mathrm{eV}^2$ [92–94] respectively. The CP phase δ_{13} is assumed to be $-90°$, based on the recent hints from [95, 96]. We now fit this simulated data with events generated assuming the 3+1 scenario. We consider $\theta_{14} \in [0, 12°]$[13], $\theta_{34} \in [0, 50°]$[14], $\theta_{23} \in [40°, 50°]$, δ_{13} and $\delta_{34} \in [-180°, +180°]$ and $\Delta m^2_{41} \in [0.1, 10]$ eV^2. Previously, we argued that the results with NC data will not depend significantly on the parameters θ_{24} and δ_{24}. However, the same is not true of the CC events i.e. the $\nu_\mu \to \nu_e$ and $\nu_\mu \to \nu_\mu$ oscillation channels. Hence, in the fit, we vary $\theta_{24} \in [0, 4°]$[15] and $\delta_{24} \in [-180°, +180°]$. We assume the hierarchy to be known and hence do not consider the inverted hierarchy while fitting. We generate event spectra for various combinations of these 3+1 test oscillation parameters and then calculate the binned Poissonian $\Delta\chi^2$ between such test events spectra and the simulated 3+0 true events spectra (data). We have assumed 5% normalisation error for the signal events and 10% normalisation error for the background events. The $\Delta\chi^2$ are marginalised over these systematic uncertainties through the method of pulls.

In Fig. 2.8, we show the sensitivity of the DUNE experiment to exclude the 3+1 paradigm with NC and CC measurements. *We consider the test case of* $\Delta m^2_{41} = 1$ eV^2. In producing these plots, we have not considered the variation of the CP violating phases in the fit, so as to show the effect of the mixing angles only. That is, we show the results corresponding to test $(\delta_{13}, \delta_{24}, \delta_{34}) = (-90°, 0, 0)$. We show the 90% C.L. limits (corresponding to $\Delta\chi^2 = 4.61$ for a two-parameter fit) in the test θ_{14} - test θ_{34} plane for different values of test θ_{24}. The left panel in Fig. 2.8 corresponds to the choice of test $\theta_{24} = 0$ and the right panel corresponds to test $\theta_{24} = 4°$, as depicted in the figure titles. We show results for NC stand-

[13]The 90% C.L. allowed range for θ_{14} has been taken from [82].

[14]Note that, the allowed range of θ_{34} from [86] is $\theta_{34} \in [0, 23°]$ at 90% C.L. However, in order to show the individual contributions from various channels we consider larger values of θ_{34}.

[15]The results from IceCube [83] dictate the allowed range for θ_{24} at 90% C.L.

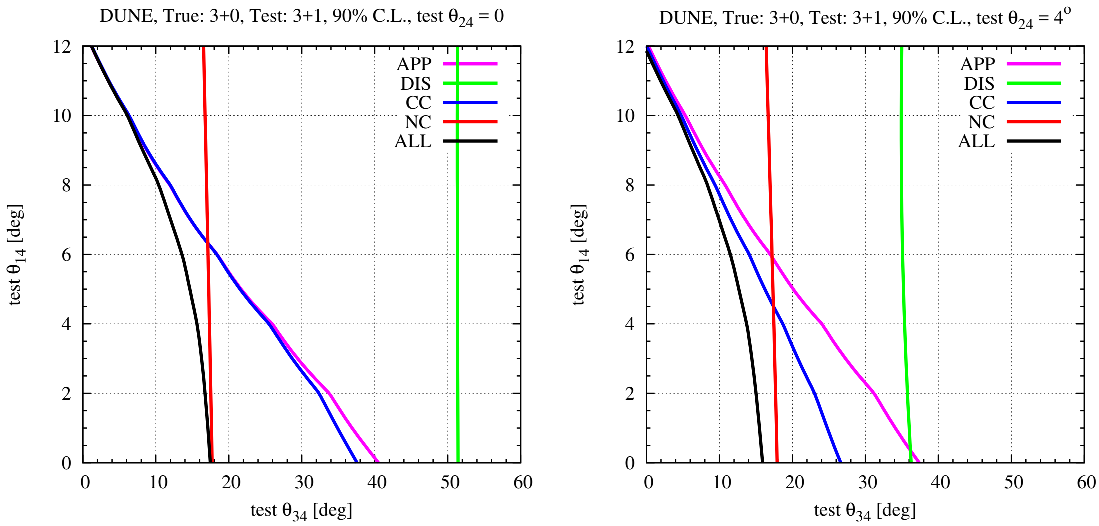

Figure 2.8: 90% ($\Delta\chi^2 = 4.61$) C.L. contour plots in the test θ_{14} - test θ_{34} plane for different choices of test θ_{24}. Left: test $\theta_{24} = 0$ and Right: test $\theta_{24} = 4°$. The true case has been taken to be 3+0 and the test case is 3+1. The value of test Δm^2_{41} is 1eV^2 for both the plots. The results are for the DUNE experiment with 3.5 years each of neutrino and anti-neutrino running. For these figures, test $(\delta_{13}, \delta_{24}, \delta_{34} = -90°, 0, 0)$ i.e. the $\Delta\chi^2$ has not been marginalised over the test CP phases. We show results for the NC standalone data, appearance standalone data, disappearance standalone data, appearance and disappearance data combined (CC) and finally, the CC and the NC data combined ("ALL").

alone data, appearance stand-alone data, disappearance stand-alone data, appearance and disappearance combined (i.e. CC data) and finally all data i.e. CC and NC combined. This helps to better understand the contribution that each type of data has in excluding the 3+1 scenario with respect to the given active-sterile mixing angle. The regions that lie towards the increasing values of test θ_{14} and test θ_{34} are the ones for which DUNE can exclude 3+1 at 90% C.L. An examination of the Fig. 2.8 allows us to draw some important conclusions:

- The NC data by itself constrains mainly the θ_{34} angle and this constraint has a small dependence on the test values of the mixing angles θ_{14} and θ_{24}. The most conservative exclusion of the θ_{34} angle corresponds to $\theta_{14} = 0$ where $\theta_{34} \gtrapprox 18°$ is excluded by the data. The strongest bound of $\theta_{34} \gtrapprox 16°$ corresponds to $\theta_{14} = 12°$.

- The appearance data are sensitive to all three active-sterile mixing angles. At $\theta_{34} = 0$, $\theta_{14} \lessapprox 12°$ is allowed for both $\theta_{24} = 0$ and $\theta_{24} = 4°$. However, the constraints on θ_{34} are somewhat weak and strongly-correlated with the values of test θ_{14}. The weakest constraints are obtained for $\theta_{14} = 0$, which excludes values corresponding to $\theta_{34} \gtrapprox 38°$.

- The disappearance data are mainly sensitive to θ_{24} and θ_{34}. The constraints are essentially independent of the value of test θ_{14}. The strongest constraint, of $\theta_{34} \gtrapprox 36°$ being ruled-out, occurs when test $\theta_{24} = 4°$.

- The combined NC+CC data are quite sensitive to θ_{34}. If $\theta_{24} = 4°$ and $\theta_{14} \sim 0$, then $\theta_{34} \gtrapprox 16°$ can be ruled out. For $\theta_{24} = 4°$ and $\theta_{14} \sim 12°$, DUNE data can rule out $\theta_{34} \gtrapprox 0$.

It is quite evident from the above discussions that the NC data have a marked advantage over the CC data in excluding the 3+1 paradigm when the mixing angles θ_{14} and θ_{24} are very small. If it so happens that the angles θ_{14} and θ_{24} are small but the angle θ_{34} is large, then, even though the appearance and the disappearance data would not show any hints of new physics, there would be a clear evidence of new physics in the NC data.

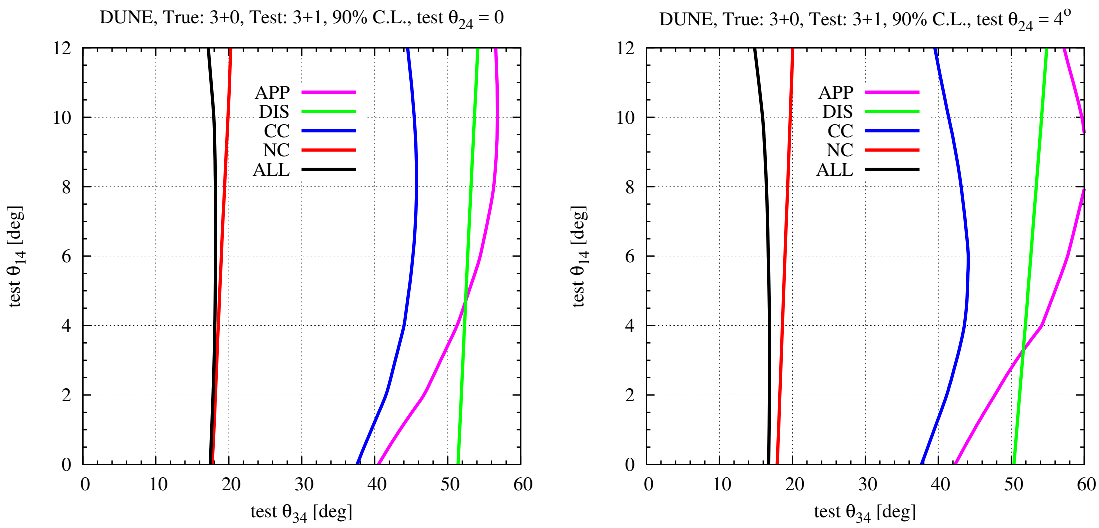

Figure 2.9: 90% ($\Delta\chi^2 = 4.61$) C.L. contour plots in the test θ_{14} - test θ_{34} plane for different choices of test θ_{24}. Left: test $\theta_{24} = 0$ and Right: test $\theta_{24} = 4°$. The true case has been taken to be 3+0 and the test case is 3+1. The value of test Δm^2_{41} is 1eV^2 for both the plots. The results are for the DUNE experiment with 3.5 years each of neutrino and anti-neutrino running. For these figures, the $\Delta\chi^2$ *has been* marginalised over the test CP phases. We show results for the NC standalone data, appearance standalone data, disappearance standalone data, appearance and disappearance data combined (CC) and finally, the CC and the NC data combined ("ALL").

In obtaining Fig. 2.8, effects of the three CP phases were not taken into account and each of the three of them were held fixed at their input true values. In Fig. 2.9, we repeat the same exercise as that in Fig. 2.8, except that, for each test combination of values of θ_{14}, θ_{24} and θ_{34}, we marginalise the $\Delta\chi^2$ over the three CP phases δ_{13}, δ_{24} and δ_{34} and select the smallest $\Delta\chi^2$. Thus, Fig. 2.9 correctly takes into account the lack of knowledge regarding the CP violating phases. It can be seen that the results due to CC appearance are significantly affected because of marginalisation over the CP phases. This physics point was emphasised in [91,97]. While for the plots in Fig. 2.8, a significant region of the given $\theta_{14} - \theta_{34}$ parameter space was ruled out by the appearance data; for the plots in Fig. 2.9, most of such $\theta_{14} - \theta_{34}$ region is allowed at 90% C.L. This holds true especially at the larger values of θ_{14}. Thus, with CC data alone, DUNE cannot be expected to provide significant constraints on θ_{34}. On the other hand, the effect of marginalisation over CP phases on the NC data is small. Thus, NC data can decisively constrain the mixing angle θ_{34} even when the CP phases are unknown, as can be seen in the plots in Fig. 2.9. Therefore, another advantage that the NC events have over CC is that they are more immune to the lack of knowledge regarding the CP phases. *Even with CP violating phases present, it would be easier to rule out a moderately large value of θ_{34} with the NC data compared to ruling out moderately large values of θ_{14} and θ_{24} with the CC data.* Taking into account the marginalisation over all the relevant mixing angles and the CP phases, the combined NC and CC data from DUNE can exclude the 3+1 paradigm for $\theta_{34} \gtrsim 18°$. With reference to Fig. 2.8 and Fig. 2.9, we note that in Fig. 2.8, the most conservative estimate of θ_{34} corresponds to $\theta_{14} = 0$. This is no longer true in Fig. 2.9 where the most conservative constraints on θ_{34} occur at larger values of θ_{14}. This difference is stark in the case of CC data which reinforces the importance of CP phases in the CC channels. For NC too, this argument holds true although the differences are much smaller in nature.

To show how the exclusion of the 3+1 paradigm depends on the mass-squared difference Δm^2_{41}, we repeat the exercise done in Fig. 2.8 for test Δm^2_{41} values ranging in $[0.1, 10]$ eV^2. We marginalise over the two mixing angles θ_{14} and θ_{24}, in addition to the CP phases, and

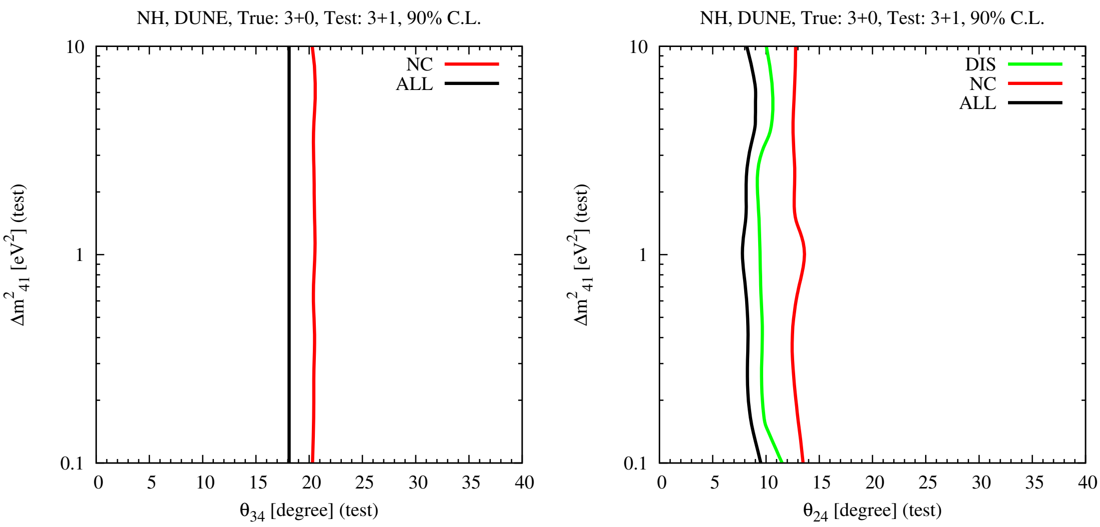

Figure 2.10: 90% ($\Delta\chi^2$ = 4.61) C.L. contour plots for 3+1 exclusion in the test Δm^2_{41} - test θ_{34} space (left) and test Δm^2_{41} - test θ_{24} space (right). The results are for the DUNE experiment with 3.5 years each of neutrino and anti-neutrino running. The true case has been taken to be 3+0 and the test to be 3+1. In the left panel, we show results with the NC data, and NC and CC data combined ("ALL"). In the right panel, we show results with the NC data, the disappearance data ("DIS") and the NC and CC data combined ("ALL").

report the minimum $\Delta\chi^2$ as a function of test Δm^2_{41} and test θ_{34}. The results are shown in the left panel of Fig. 2.10. Note that the other details regarding the simulation and assumptions on the oscillation parameters remain the same as those in Fig. 2.8. It is easy to see that the results do not depend much on the mass-squared difference Δm^2_{41}. At 90% C.L., $\theta_{34} \gtrsim 18°$ can be ruled out with the combined CC and NC data. With NC data alone, $\theta_{34} \gtrsim 20°$ can be ruled out at 90% C.L. NC data is most effective in constraining θ_{34}. On combining the NC data with the CC data an improvement of $\approx 2°$ is seen.

We show DUNE's ability to constrain the $\Delta m^2_{41} - \theta_{24}$ parameter space in the right panel of Fig. 2.10. We consider test Δm^2_{41} values ranging in $[0.1, 10]$ eV^2 and test θ_{24} values in $[0, 40°]$. In the fit, we marginalise over θ_{14} and θ_{34} and the three CP violating phases. It can be seen that most of the sensitivity to the exclusion of θ_{24} comes from the disappearance data. With the CC and NC data combined, DUNE can rule out $\theta_{24} \gtrsim 9° \pm 1°$ depending on the test value of Δm^2_{41}. The current results from IceCube already exclude $\theta_{24} \gtrsim 4°$ at 90% C.L. for test $\Delta m^2_{41} \approx 0.5$ eV^2 However, IceCube's θ_{34}-constraint is strongly correlated with the test value of Δm^2_{41} and it can be seen in [83] that for test $\Delta m^2_{41} \approx 10$ eV^2, the constraints from the IceCube data worsen to $\theta_{24} \gtrapprox 45^\circ$ at 90% C.L. DUNE, on the other hand, can provide a strong constraint on θ_{24} that is relatively independent of test Δm^2_{41}.

Chapter 3

Non Unitarity at DUNE and T2HK with Charged and Neutral Current Measurements

Neutrino oscillation remains one of the strongest hints of physics beyond the standard model. The smallness of neutrino masses is yet to be understood and there are many different models attempting to explain it. Non-unitarity (NU) of the neutrino mixing matrix [98–100] is yet another interesting departure from the standard three-neutrino paradigm. One way it appears in the theory is via the type-I seesaw mechanism [21,23,27] which gives masses to the neutrinos via the exchange of fermionic messengers. In the type-I seesaw, due to the presence of a Majorana mass term for heavy right handed neutrinos, we need a matrix bigger than the 3×3 PMNS mixing matrix for diagonalization of the mass matrix. This results non-unitarity of the PMNS matrix and it is discussed in detail in [61] and also in section 1.6. There are other variants of low-scale seesaw mechanism such as the inverse and linear seesaw [31, 32, 101, 102] where the masses of the right handed neutrinos are not so heavy compared the type-I seesaw and it can produce sizeable non unitarity in the leptonic mixing matrix [62, 63]. Generally, non unitarity of the leptonic mixing matrix may arise due to the effect of new physics at both high and low energy scales. At high energies, the non unitarity of the three flavor mixing matrix, called the indirect non-unitary effect [103–106], is because of the mixing of heavy right-handed neutrinos. On the other hand, direct non-unitary effects are manifested at lower energy scales i.e. an energy which is much below the electroweak breaking scale. The light SM gauge group singlet (or light sterile neutrinos) mixes with the active neutrino through mixing and also take part in neutrino oscillations. It was the LSND experiment [49] which for the first time claimed a signal consistent with oscillations driven by $\Delta m^2_{41} \sim 1$ eV^2. It found an excess of positrons which could be explained in terms of $\bar{\nu}_\mu \to \bar{\nu}_e$ oscillations driven by this mass-squared difference. If nature has such sterile states, it can also lead to non unitarity of the 3×3 leptonic mixing matrix. The non unitarity framework introduces new CP phases, which appear together with the standard CP phase in oscillation probabilities and hamper measurements at the far detectors of long baseline experiments [63, 98, 99, 107–112].

Most studies on non unitarity have been focused on CC measurements at the far detector of long-baseline neutrino experiments which generally measure $\nu_\mu \to \nu_e$ and $\nu_\mu \to \nu_\mu$ oscillations, both in neutrino and anti-neutrino modes [63, 107–111]. Recently, NC measurements have been explored at DUNE [71, 113] in the context of one light sterile neutrino [114, 115]. Constraints on one light sterile neutrino have already been derived at DUNE and T2HK [116] and can be found in [117–120]. However, the larger non unitarity framework is more general than the one encompassing just one extra light sterile neutrino.

Here in this chapter, we have incorporated NC measurements with CC measurements to derive the constraints on NU parameters. There already exist tight constraints on the NU parameters [61, 63, 121] that come from weak interaction universality and lepton flavour violating processes (LFV). There are also model independent direct bounds on NU parameters coming from zero distance experiment such as NOMAD [122, 123] and neutrino oscillation experiments [124, 125]. In this chapter, however, we derive complementary bounds on those parameters in presence of NC measurements at DUNE. We have also explored the effect of combining NC measurements with the CC measurements at DUNE to probe the bounds. In addition to that, we quantify the bounds that comes from T2HK and then combine it with DUNE to explore the enhanced effect.

3.1 The Non Unitarity Framework

In the presence of non unitarity due to heavy sterile neutrino, states in the mass basis ($|\nu_i >$) remain orthogonal to each other, while the low energy effective flavor states [1]($|\nu_\alpha\rangle$), are not orthogonal, can be represented as

$$|\nu_\alpha\rangle = N^*_{\alpha i}|\nu_i\rangle, \tag{3.1.1}$$

where N is a 3×3 general matrix [63] and can be represented as

$$N = N^{NU}U = \begin{bmatrix} \alpha_{11} & 0 & 0 \\ \alpha_{21} & \alpha_{22} & 0 \\ \alpha_{31} & \alpha_{32} & \alpha_{33} \end{bmatrix} U.$$

Here U is the standard unitary PMNS mixing matrix and it depends on three mixing angles (θ_{12}, θ_{13}, and θ_{23}) and one CP violating phase (δ_{cp}). N^{NU} contains the non unitarity part. Under the condition that all the diagonal elements of N^{NU} are unity and all the off-diagonal elements vanish, then N becomes the standard PMNS mixing matrix. The diagonal elements (α_{11}, α_{22} and α_{33}) of N^{NU} are real and the off-diagonal elements (α_{21}, α_{31} and α_{32}) are complex in general and can be expressed as $\alpha_{ij} = |\alpha_{ij}|e^{\phi_{ij}}$ for $i \neq j$. There

[1]For light sterile neutrinos, the flavor basis remains orthogonal (i.e. $\langle\nu_\alpha|\nu_\beta\rangle = \delta_{\alpha\beta}$) as all the mass eigenstates are kinematically accessible.

are three new CP phases ϕ_{21}, ϕ_{31} and ϕ_{32} that arise in the mixing matrix N in presence of non unitarity. The new phases, especially ϕ_{21} can play an important role in long-baseline experiments such as DUNE and T2HK. This affects the standard CP (δ_{cp}) sensitivity of these experiments significantly [107, 109]. For the later portion of the discussion, we denote $|\alpha_{ij}|$ as α_{ij} for notational simplicity and mention the CP phases (ϕ_{ij}) explicitly. In this section, we analyse the effect of non unitarity on the neutrino oscillation probability.

In the presence of non unitarity, the time evolution of the mass eigenstate in vacuum is

$$i\frac{d \mid \nu_i\rangle}{dt} = H \mid \nu_i\rangle, \tag{3.1.2}$$

where H is the free Hamiltonian in the mass basis and can be expressed as

$$H = \begin{bmatrix} 0 & 0 & 0 \\ 0 & \frac{\Delta m^2_{21}}{2E} & 0 \\ 0 & 0 & \frac{\Delta m^2_{31}}{2E} \end{bmatrix}.$$

Here E is the energy of the neutrinos and Δm^2_{21} and Δm^2_{31} are the solar and atmospheric mass squared differences respectively. After time t(≡L), the flavor state can be written as

$$|\nu_\alpha(t)\rangle = N^*_{\alpha i}|\nu_i(t)\rangle = N^*_{\alpha i}(e^{-iHt})_{ij}|\nu_j(t=0)\rangle. \tag{3.1.3}$$

Hence the transition probability from one flavor to another in presence of non unitarity can be written as

$$P(\nu_\alpha \to \nu_\beta) = |\langle \nu_\beta|\nu_\alpha(t)\rangle|^2 = |\sum_{k,j}^{3} N^*_{\alpha k} diag(e^{-i\Delta m^2_{k1} t/2E})_{kj} N_{\beta j}|^2. \tag{3.1.4}$$

In presence of matter the flavor eigenstates interact with matter coherently and the free Hamiltonian gets modified. In the presence of non unitarity, the interaction Lagrangian becomes

$$\mathcal{L}_{int} = -\frac{g}{2\sqrt{2}}(W_\mu \bar{l}_\alpha \gamma^\mu (1-\gamma_5) N_{\alpha i} \nu_i) - \frac{g}{2\cos(\theta_W)}(Z_\mu \bar{\nu}_i \gamma^\mu (1-\gamma_5)(N^\dagger \mathrm{N})_{ij} \nu_j) + h.c. \qquad (3.1.5)$$

Therefore in the mass basis, the total Hamiltonian (H_{mat}) [126] of the propagating neutrino is given by

$$H_{mat} = \begin{bmatrix} 0 & 0 & 0 \\ 0 & \frac{\Delta m^2_{21}}{2E} & 0 \\ 0 & 0 & \frac{\Delta m^2_{31}}{2E} \end{bmatrix} + N^T \begin{bmatrix} V_{CC} + V_{NC} & 0 & 0 \\ 0 & V_{NC} & 0 \\ 0 & 0 & V_{NC} \end{bmatrix} N^*, \qquad (3.1.6)$$

where $V_{CC} = \sqrt{2} G_F n_e$ and $V_{NC} = -\frac{1}{\sqrt{2}} G_F n_n$ are the charged current and neutral current matter potential respectively. Here n_e and n_n are the electron and neutron densities respectively [2]. The Hamiltonian H_{mat} is hermitian and we can diagonalize it by a unitary matrix (U_m) as:

$$H_{mat} = U_m \begin{bmatrix} a_1 & 0 & 0 \\ 0 & a_2 & 0 \\ 0 & 0 & a_3 \end{bmatrix} U_m^\dagger, \qquad (3.1.7)$$

where a_1, a_2 and a_3 are the eigenvalues of H_{mat}. Therefore, the transition probability ($\nu_\alpha \to \nu_\beta$) becomes

$$P(\nu_\alpha \to \nu_\beta) = |\langle \nu_\beta | \nu_\alpha(t) \rangle|^2 = |N^*_{\alpha i}(U_m diag(e^{-ia_1 t}, e^{-ia_2 t}, e^{-ia_3 t}) U_m^\dagger)_{ij} N_{\beta j}|^2. \qquad (3.1.8)$$

We note that most of the upcoming super beam neutrino experiments will measure their flux through near detector measurements. Therefore, in the presence of non unitarity the

[2]We assume that the electron (n_e) and neutron (n_n) densities are same for DUNE and T2HK and for simplicity also assume constant matter density (ρ = 2.95 gm/cc) for our simulated results.

expected events at the near detector differ from the actual events by a factor of $P(\nu_\alpha \rightarrow \nu_\alpha) = ((NN^\dagger)_{\alpha\alpha})^2$. For DUNE and T2HK, the beam comprises mainly of muon neutrinos, and hence the above factor, i.e. the normalization factor, becomes $((NN^\dagger)_{\mu\mu})^2 = ((\alpha_{22})^2 + |\alpha_{21}|^2)^2$. Depending on the values of α_{22} and $|\alpha_{21}|$, we will get different muon events compared to (simulated) events without NU at the near detector. *If* $\alpha_{22} \sim 0.95$ *and* $\alpha_{21} \sim 0$, *then there will be a mismatch of around* 20% *between the simulated and the actual events.* Thus, the near detector measurements can in principle put a tight constraint on the non unitarity parameter α_{22}.

Now, the ν_α events (R_α) in a detector which are located at a distance L from the ν_μ source, are given by

$$R_\alpha \sim \int dE \frac{d\Phi_\mu^{\rm source}(E)}{dE} \frac{P_{\mu\alpha}(E,L)}{L^2} \sigma_\alpha(E)\eta(E), \tag{3.1.9}$$

where $\dfrac{d\Phi_\mu^{\rm source}(E)}{dE}$ is the muon neutrino flux at the source, $\sigma_\alpha(E)$ is the detection cross section and $\eta(E)$ is the detection efficiency. The flux at source is unknown. We can measure it through near detector measurements or we can rely on Monte Carlo simulation of the flux. At near detector the muon events ($R_\mu(E)$) from ν_μ beam can be expressed as:

$$R_\mu(E)_{near} \sim \int dE \frac{d\Phi_\mu^{\rm source}(E)}{dE} (\frac{P_{\mu\mu}(E,L)}{L^2})_{near} \sigma_\mu(E)\eta(E).$$

Hence,

$$\frac{d\Phi_\mu^{\rm source}(E)}{dE} \propto R_\mu(E)_{near}/(P_{\mu\mu})_{near}.$$

In the standard case $(P_{\mu\mu})_{near} \simeq 1$ but for the non unitarity case $(P_{\mu\mu})_{near} = (NN^\dagger_{\mu\mu})^2 = (\alpha_{22}^2 + \alpha_{21}^2)^2$ which is different from unity. So, in presence of non unitarity, the measured flux at near detector will be different from the standard simulated flux by the factor $(P_{\mu\mu})_{near}$. Using the near detector flux measurements, the events at far detector can be expressed as:

$$\begin{aligned} R_\alpha(E)_{far} &\sim \int dE \frac{d\Phi_\mu^{\text{source}}(E)}{dE} (\frac{P_{\mu\alpha}(E,L)}{L^2})_{far} \sigma_\alpha(E) \eta(E), \\ &\propto \frac{R_\mu(E)_{near}}{(P_{\mu\mu})_{near}} (P_{\mu\alpha})_{far}. \end{aligned} \tag{3.1.10}$$

Now we can measure the transition probability by the ratio of far and near detector events as:

$$P_{\mu\alpha} \sim \frac{(R_\alpha)_{far}}{(R_\mu)_{near}} \sim \frac{(P_{\mu\alpha})_{far}}{(P_{\mu\mu})_{near}}. \tag{3.1.11}$$

For the standard case, $(P_{\mu\mu})_{near} \simeq 1$. Hence the measured oscillation probability ($P_{\mu\alpha}$) coincides with the actual oscillation probability $(P_{\mu\alpha})_{far}$. But for the non unitarity case, the measured oscillation probability ($P_{\mu\alpha}$) will be different from $(P_{\mu\alpha})_{far}$ due to the factor $(P_{\mu\mu})_{near}$. Therefore, in presence of non unitarity, the effect of flux measurements at the near detector can be included in the measured oscillation probability through the normalization factor $(P_{\mu\mu})_{near}$ [106] as in Eq. 3.1.11 and that factor plays an important role in constraining the NU parameters. In the disappearance channel, the NU parameter which causes the maximum effect in the probability cancels the effect of that NU parameter when we consider the normalization factor as discussed in [127]. It is also apparent from the disappearance plot of Fig. 3.1.

Now, if we use the simulated flux at the source, then using Eq. 3.1.9, we can directly calculate the transition probability. Hence, for the simulated flux, we do not need to consider the normalization factor $(NN^\dagger)^2_{\mu\mu}$ (arising from the near detector flux measurements) to measure the transition probability and the measured oscillation probability ($P_{\mu\alpha}$) will be same as $(P_{\mu\alpha})_{far}$. In this analysis, we have considered two cases i.e. one with the simulated flux at source where normalization factor is not required in the probability expression and the other with near detector measurements i.e. the normalization factor is present in the probability calculation.

In the presence of non unitarity, both the charged current and the neutral current events get modified. The neutral current events for the ν_μ beam in vacuum are proportional to

$$\begin{aligned} N^{NC}_{events} &\propto \sum_{j=1}^{3} |\sum_{i=1}^{3} A(W \to \mu^+ \nu_i) exp(-i\Delta m^2_{i1} L/2E) A(\nu_i Z \to \nu_j)|^2 \\ &= \sum_{j=1}^{3} |\sum_{i=1}^{3} N^*_{\mu i} exp(-i\Delta m^2_{i1} L/2E)(N^\dagger N)_{ji}|^2. \end{aligned} \tag{3.1.12}$$

In presence of matter the NC events will be proportional to

$$N^{NC}_{events} \propto \sum_{k=1}^{3} |\sum_{i,j=1}^{3} N^*_{\mu i}(U_m diag(e^{-ia_1 t}, e^{-ia_2 t}, e^{-ia_3 t})U^\dagger_m)_{ij}(N^\dagger N)_{kj}|^2, \tag{3.1.13}$$

where U_m and a_i's are defined in Eq. 3.1.7.

Light Sterile case:

The 3×3 PMNS mixing matrix will also become non unitary in the presence of light sterile neutrinos. As shown in [106], in this case, the leading charged current transition probability among the active flavors will remain the same as the non unitary case (due to the heavy sterile neutrinos) if the effect of the light sterile neutrino is averaged out in the detector. The active flavor states in the presence of light sterile neutrinos can be represented as

$$|\nu_\alpha\rangle = u^*_{\alpha l}|\nu_l\rangle = \sum_{i=1}^{3} N^*_{\alpha i}|\nu_i\rangle + \sum_{J=4}^{n} \Theta^*_{\alpha J}|\nu_J\rangle, \tag{3.1.14}$$

where u is a unitary mixing matrix and its dimension (n) depends on the number of sterile neutrinos. N represents the 3×3 active-light sub-block of u and Θ represents the $3\times n$ sub-block of u that mixes active and sterile states. The vacuum transition probability $\nu_\alpha \to \nu_\beta$

in presence of light sterile neutrino is given by

$$
\begin{aligned}
P(\nu_\alpha \to \nu_\beta) &= |\langle \nu_\beta | \nu_\alpha(t) \rangle|^2 = |u^*_{\alpha i} diag(e^{-i\Delta m^2_{i1} t/2E})_{ij} u_{\beta j}|^2 \\
&= |\sum_{i,j=1}^{3} N^*_{\alpha i} diag(e^{-i\Delta m^2_{i1} t/2E})_{ij} N_{\beta j} + \sum_{J,K=4}^{n} \Theta^*_{\alpha J} diag(e^{-i\Delta m^2_{J1} t/2E})_{JK} \Theta_{\beta K}|^2 \\
&= |\sum_{i,j=1}^{3} N^*_{\alpha i} diag(e^{-i\Delta m^2_{i1} t/2E})_{ij} N_{\beta j}|^2 + \mathcal{O}(\Theta^4). \qquad (3.1.15)
\end{aligned}
$$

The cross terms will vanish in the limit $\Delta m^2_{J1} L/2E >> 1$ (where $L \equiv t$) since the finite energy resolution of the detector will render $< \sin(\Delta m^2_{J1} L/2E) >=< \cos(\Delta m^2_{J1} L/2E) >= 0$. Therefore, if we neglect the correction corresponding to order (Θ^4), then the leading order transition probability $\nu_\alpha \to \nu_\beta$, will be same as Eq. 3.1.4.

In the presence of light sterile neutrinos, the neutral current events also change from their standard value. Only the active flavors participate in the neutral current events, and we have, for vacuum case and a ν_μ beam the proportionality to

$$
\begin{aligned}
N^{NC}_{events} &\propto \sum_{j=1}^{n} |\sum_{i=1}^{n} A(W \to \mu^+ \nu_i) exp(-i\Delta m^2_{i1} L/2E) A(\nu_i Z \to \nu_j)|^2 \\
&= \sum_{j=1}^{n} |\sum_{i=1}^{n} u^*_{\mu i} exp(-i\Delta m^2_{i1} L/2E) (\sum_{\rho=e,\mu,\tau} u^\dagger_{j\rho} u_{\rho i})|^2 \qquad (3.1.16) \\
&= \sum_{\rho=e,\mu,\tau} P(\nu_\mu \to \nu_\rho). \qquad (3.1.17)
\end{aligned}
$$

Now from Eq. 3.1.16, we can write

$$
N^{NC}_{events} \propto \sum_{j=1}^{n} |\sum_{i=1}^{n} u^*_{\mu i} exp(-i\Delta m^2_{i1} L/2E) (\sum_{\rho=e,\mu,\tau} u^\dagger_{j\rho} u_{\rho i})|^2
$$

$$
= \sum_{j=1}^{n} |\sum_{i=1}^{3} N^*_{\mu i} exp(-i\Delta m^2_{i1} L/2E) (\sum_{\rho=e,\mu,\tau} u^\dagger_{j\rho} N_{\rho i}) + \sum_{I=4}^{n} \Theta^*_{\mu I} exp(-i\Delta m^2_{I1} L/2E) (\sum_{\rho=e,\mu,\tau} u^\dagger_{j\rho} \Theta_{\rho I})|^2
$$

$$= \sum_{j=1}^{n} |\sum_{i=1}^{3} N^*_{\mu i} exp(-i\Delta m^2_{i1} L/2E)(\sum_{\rho=e,\mu,\tau} u^\dagger_{j\rho} N_{\rho i})|^2 + O(\Theta^4)$$

$$\simeq \sum_{j=1}^{3} |\sum_{i=1}^{3} N^*_{\mu i} exp(-i\Delta m^2_{i1} L/2E)(\sum_{\rho=e,\mu,\tau} N^\dagger_{j\rho} N_{\rho i})|^2 + \sum_{J=4}^{n} |\sum_{i=1}^{3} N^*_{\mu i} exp(-i\Delta m^2_{i1} L/2E)(\sum_{\rho=e,\mu,\tau} \Theta^\dagger_{J\rho} N_{\rho i})|^2$$

$$= \sum_{j=1}^{3} |\sum_{i=1}^{3} N^*_{\mu i} exp(-i\Delta m^2_{i1} L/2E)(N^\dagger N)_{ji}|^2 + \sum_{J=4}^{n} |\sum_{i=1}^{3} N^*_{\mu i} exp(-i\Delta m^2_{i1} L/2E)(\sum_{\rho=e,\mu,\tau} \Theta^\dagger_{J\rho} N_{\rho i})|^2 \quad (3.1.18)$$

Due to the presence of the Θ^2 term in Eq. 3.1.18, the neutral current events will not remain same as Eq. 3.1.12 in the leading order. Therefore, the NC analysis will be different for light and heavy sterile case to that order.

The constraints on the NU parameters due to heavy sterile are very tight [61, 109, 121]. The constraints derived by using precision measurements of electroweak processes are not applicable for light sterile neutrinos. Hence, oscillation experiments provide the best way to probe the NU in the presence of light sterile neutrinos. In the averaged out regime of light sterile neutrino corresponding to Eq. 3.1.15, the NU due to a heavy sterile is nearly same as light sterile neutrino. Therefore, we take the mass of the light sterile neutrino to be such that it averages out before reaching the near detector. Henceforth, in the rest of the chapter, we consider non unitarity that comes from light sterile neutrino. Using NC and CC measurements, we constrain NU parameters that also provide the complementary bounds of NU parameters due to the heavy sterile neutrino as the oscillation probabilities nearly same in both cases.

3.2 Experimental and Simulation details

In this work we present results for the DUNE and T2HK experiments. The configurations of DUNE experiment are discussed in the section 2.2. The specifications of T2HK experiment are as follows:

3.2.1 T2HK

Hyper-Kamiokande (HK) [116,128,129] is the upgraded version of the Super-Kamiokande (SK) [45] program in Japan. In this experiment, the fiducial mass of the SK detector will be increased by about twenty times. HK will have two 187 kt third generation Water Cherenkov detector modules which will be placed near the current SK site. The detector will be placed at a baseline of 295 km from the J-PARC proton accelerator research complex in Tokai, Japan. T2HK has almost similar physics goals as DUNE, such as measuring the neutrino mass hierarchy, the octant of θ_{23}, and determining the leptonic CP phase.

In our analysis we have considered a beam power of 1.3 MW and the 2.5^0 off-axis flux for T2HK. The total fiducial mass considered is 374 kt, corresponding to two tanks each of 187 kt. We have assumed a total run time of 10 years, of which the neutrino run will be for 2.5 years while the anti-neutrino run will be for 7.5 years. The assumed energy resolution is $15\%/\sqrt{E}$. As a check, we have matched the number of events used in this work with the TABLE III and TABLE IV of ref. [128]. The signal normalization error in $\nu_\mu(\bar{\nu}_\mu)$ disappearance and $\nu_e(\bar{\nu}_e)$ appearance channel are 3.9% (3.6%) and 3.2% (3.6%) respectively. The background and energy calibration errors assumed in this work are 10% and 5%, respectively for all channels.

Throughout the analysis, we have fixed the true values or the best fit values of the neutrino oscillation parameters as given in [44] unless stated. We fix the true values of the solar and the reactor mixing angles at $\theta_{12} = 33.82°$ and $\theta_{13} = 8.61°$ respectively. The assumed true value of the atmospheric mixing angle is $\theta_{23} = 49.7°$. The true value of the leptonic CP phase is fixed at $\delta_{cp} = 217^0$. The mass square differences considered in this work are $\Delta m^2_{21} = 7.39 \times 10^{-5}$ eV^2 and $\Delta m^2_{31} = 2.525 \times 10^{-3}$ eV^2 respectively. The 3σ bounds on the NU parameters are taken from the neutrino experiments only and can be found at [109][3]. We have prepared a non unitarity code for this work which provides results consistent

[3]Since in the averaged out limit of light sterile neutrino, the NU due to heavy sterile is same as light sterile neutrino and hence the bounds given in [109] is also applicable to our case.

with the MonteCUBES [130] non unitarity engine. The results presented in this work are generated by incorporating our non-unitarity code with GLoBES [67, 68].

3.3 Results

In this section, we present our results for DUNE and T2HK experiments. First, we discuss the effect of non unitarity on neutrino oscillation at the probability level and then at the χ^2 level.

3.3.1 Probability Plots

In Fig. 3.1 and Fig. 3.2, we show the effect of NU parameters on both the appearance and the disappearance probabilities at DUNE in presence of matter effects. We consider one NU parameter at a time to disentangle the effect of a particular parameter from the rest but in the χ^2 analysis we consider all the parameters as simultaneously varying. Again, to incorporate the near detector measurements, we have to consider the normalization factor $((NN^\dagger)_{\mu\mu})^2 = (\alpha_{22}^2 + \alpha_{21}^2)^2$ [4], in the transition probability as in Eq.3.1.11. But that is not the case for the simulated flux. We show the probability plots both with and without the normalization factor. Wherever we use the normalization factor, we specify it in the plots.

Fig. 3.1 shows the effects of the diagonal NU parameters on appearance and disappearance channels. The red line corresponds to the standard 3ν oscillation probability. The purple line corresponds to the case with $\alpha_{11} = 0.95$. It is seen that α_{11} has a significant effect on the appearance channel. The cyan solid (dashed) line shows the effect of α_{22} with (without) the normalization factor. In the appearance channel, α_{22} has a significant effect irrespective of the normalization factor. On the other-hand, normalization reduces the ef-

[4] Only α_{22} and α_{21} will arise in the normalization factor for the ν_μ beam. Therefore, we consider the normalization factor for α_{22} and α_{21}. We consider only one NU parameter at a time while generating the probability plots. Hence there is no difference between with and without normalization for other NU parameters.

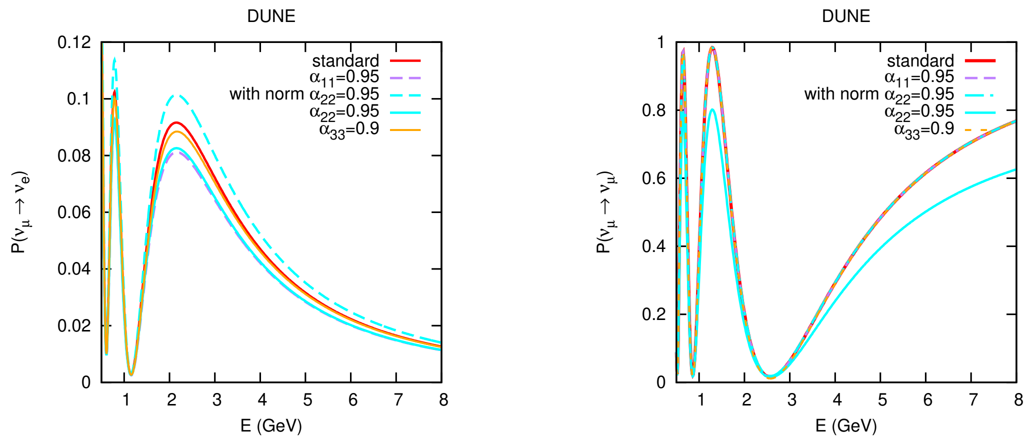

Figure 3.1: Effect of diagonal NU parameters on appearance and disappearance channels considering one parameter at a time. All the non diagonal parameters are kept at zero. The plots are shown for $\alpha_{11} = \alpha_{22} = 0.95$ and $\alpha_{33} = 0.9$.

fect of α_{22} on the disappearance channel. But the effect of α_{22} without the normalization is significant in the disappearance channel. Therefore, if we consider the simulated flux, then both the appearance and disappearance channels will get affected by α_{22}. The effect of α_{33} is very small on both the appearance and the disappearance channel and hence constraining it by these channels is not very fruitful.

In Fig. 3.2, we show the effect of non diagonal NU parameters on the oscillation probability while setting the diagonal parameters to unity. Since there is a phase associated with each non-diagonal parameter, we show the probability plots for a fixed value of the phase ϕ_{ij}. The top left panel shows the variation of α_{21} while the top right panel shows the variation of α_{31} and α_{32}. In the lower panel, we have shown the effect of all the three non diagonal parameters on the disappearance channel. Even a small value of α_{21} can change P($\nu_\mu \to \nu_e$) oscillation probability significantly almost for all the values of energy. The effect of the normalization factor is negligible in this case. If the phase ϕ_{21} is allowed to vary for a given value of α_{21}, the probability deviates from the standard 3ν case specially around the oscillation maxima. The other two non-diagonal parameters α_{31} and α_{32} has negligible effect on the appearance channel. But for larger values of α_{31} (say around 0.1), we can see a significant deviation from the standard case and a large phase dependency.

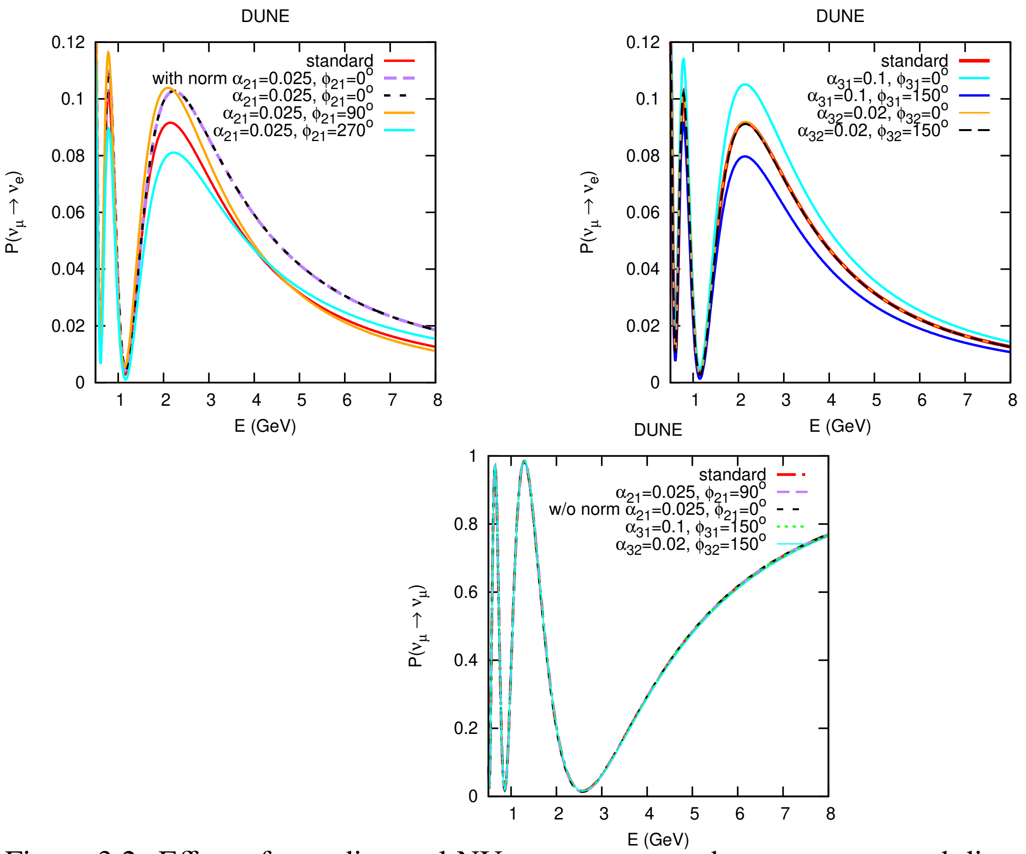

Figure 3.2: Effect of non-diagonal NU parameters on the appearance and disappearance channels.

From the plots in the lower panel, it is observed that the non diagonal parameters do not affect the measurements of the disappearance channel significantly. From all of these results, we can draw the following conclusions:

- Effects of α_{11} on the appearance channels are large compared to the disappearance channel.
- The effect of normalization is crucial for the α_{22} parameter. Depending on the normalization condition both the appearance and disappearance channel will contribute.
- The effect of α_{33} is very small on both the appearance and disappearance channel.
- Out of the three non diagonal parameters, α_{21} affects the appearance probability

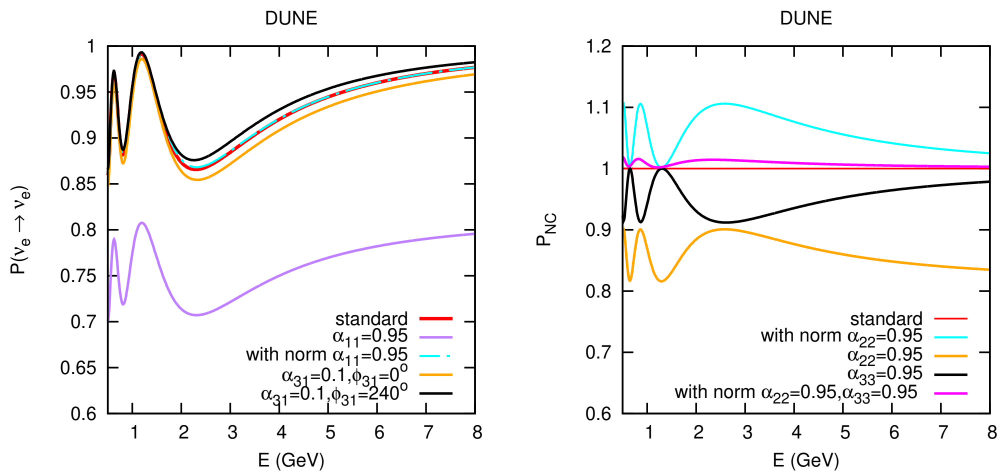

Figure 3.3: Effect of NU parameters on the Background neutrino oscillation ($\nu_e \to \nu_e$) and on the neutral current probability.

significantly. The effect is enhanced in presence of the phase. None of these parameters has any noticeable effect on disappearance probability.

In Fig. 3.3, we show the variation of P_{ee} as well as the NC measurements with energy as a function of NU parameters. The P_{ee} oscillation probability plays an important role in the background events. With the normalization,[5] although the effect of α_{11} on P_{ee} is negligible, yet the probability changes drastically for the same value of α_{11} if the normalization is switched off. The effect of normalization on P_{ee} channel plays an important role to constrain the α_{11} parameter as discussed in 3.3.3 and 3.3.4. The effect of α_{31} is small compared to α_{11} but it shows a mild CP dependence. From the right panel of Fig. 3.3, we observe that in the presence of α_{22} and α_{33}, the P_{NC} oscillation probability decreases significantly from unity. But with normalization factor (as α_{22}^4 is in the denominator) the NC probability becomes greater than unity. Therefore, when we consider both the parameters α_{22} (with norm) and α_{33} simultaneously there is a cancellation between α_{22} and α_{33} as shown by the pink line in the right panel of Fig. 3.3.

[5]For P_{ee} channel the normalization factor is α_{11}^4.

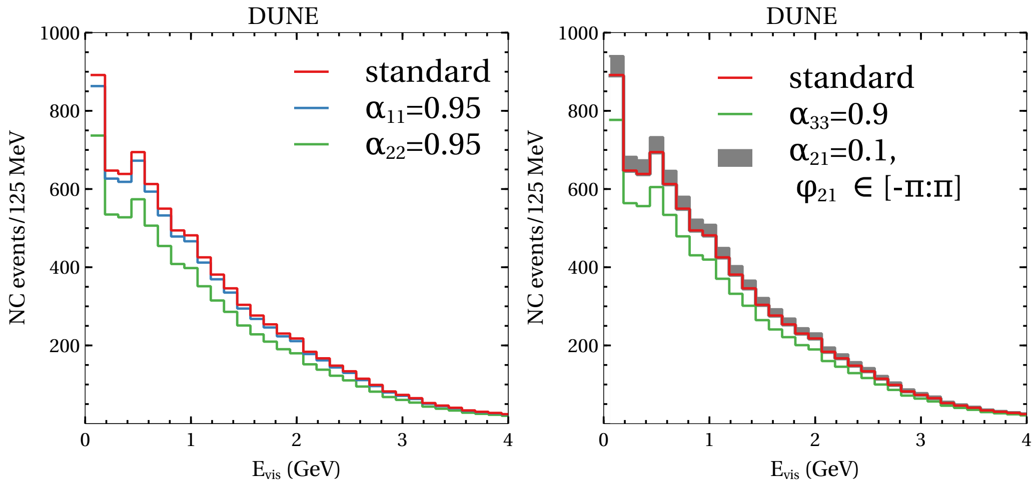

Figure 3.4: NC neutrino events in presence of one NU parameter at a time without the normalization factor.

3.3.2 NC event Plots

In Fig. 3.4, we show the NC events as a function of the visible energy (E_{vis}) in the detector in presence of NU parameter without the normalization factor. We consider one NU parameter at a time to show the effect of that particular parameter in the NC events. The red line corresponds to the expected number of events in the standard scenario. From the left panel, we observe that in presence of α_{22}, the NC events reduce significantly. Therefore, NC measurements are useful to constrain the α_{22} parameter. The effect of α_{11} is very mild on NC events as shown by the blue line in the left panel. In the right panel, we have shown the effect of α_{33}, α_{21} and ϕ_{21}. In presence of α_{33}, the events get suppressed compared to standard expected values. Hence, we can put an effective bound on α_{33} using NC measurements. The grey band corresponds to the case of varying ϕ_{21} in the full range keeping α_{21} at 0.1. The band crosses the standard events since we consider only α_{21} with ϕ_{21} variation keeping other parameters fixed to their standard model values. Now, α_{21} affects the NC events mildly and there are CP dependency in the events. Therefore, the NC events help to improve the bound on α_{21} slightly.

In the next subsection, we present our sensitivity plots to constraint the NU parameters.

3.3.3 χ^2 analysis

To quantify the effect of non unitarity at DUNE and T2HK, we have performed a χ^2 analysis. We define the χ^2 as:

$$\chi^2(\mathbf{n}^{\text{true}}, \mathbf{n}^{\text{test}}, f) = 2\sum_{i}^{N_{reco}}(n_i^{\text{true}} ln\frac{n_i^{\text{true}}}{n_i^{\text{fit}}(f)} + n_i^{\text{fit}}(f) - n_i^{\text{true}}) + f^2, \tag{3.3.1}$$

where $\mathbf{n}$ represents event rate vectors in N_{reco} bins of reconstructed energy and f is the nuisance parameter. n_i^{true} stands for the true events corresponding to standard three neutrino oscillation paradigm and $n_i^{\text{fit}}(f)$ represents the events corresponding to the new physics i.e. non unitarity. In the fit, we have marginalized over all the standard neutrino oscillation parameters in their 3σ allowed ranges. The standard CP phase (δ_{cp}) is marginalized over the full range. In addition to that, we have also marginalized over all the NU parameters in the ranges : $\alpha_{11} \in [1, 0.95], \alpha_{22} \in [1, 0.96], \alpha_{33} \in [1, 0.76], \alpha_{21} \in [0, 0.026], \alpha_{31} \in [0, 0.098]$ and $\alpha_{32} \in [0, 0.017]$. The unknown CP phases ϕ_{ij} are marginalized over the full range i.e. $\phi_{ij} \in [0°, 360°]$. In this way, we choose the minimum $\Delta\chi^2$ for a selective NU parameter by marginalizing over all the standard as well as the remaining NU parameters.

In Fig. 3.5, 3.6, and 3.7 we show the capability of DUNE, T2HK and their combination, to probe the NU parameters. We focus mainly on the diagonal NU parameters α_{11}, α_{22} and α_{33}, and off-diagonal parameter α_{21}. The bounds on the other two parameters i.e. α_{31} and α_{32} are not improved compared to the present bounds and hence those results are not included in this discussion. The results are shown for two specific cases: with normalization factor (w norm) and without normalization factor (w/o norm). The plots captioned as 'w norm' means that the norm factor is used for both background and signal. The term 'w/o ν_e BG norm' stands for the case where the norm factor is not used for the ν_e (and $\bar{\nu}_e$) background, but used for all other backgrounds. The term 'w/o norm' stands for the cases where norm factor is not used for both background and signal. In the top panel of Fig. 3.5

we have shown the sensitivity of α_{11} (upper panel) and α_{22} (lower panel) both for DUNE and T2HK. We have presented the results for CC measurements at T2HK and then for the combination of it with CC and NC measurements at DUNE, named as 'COMB'. In Fig. 3.6, we show the constraints for α_{21} and in Fig. 3.7, obtained constraints are shown for α_{33} both at DUNE and T2HK. We draw the following conclusions from this analysis:

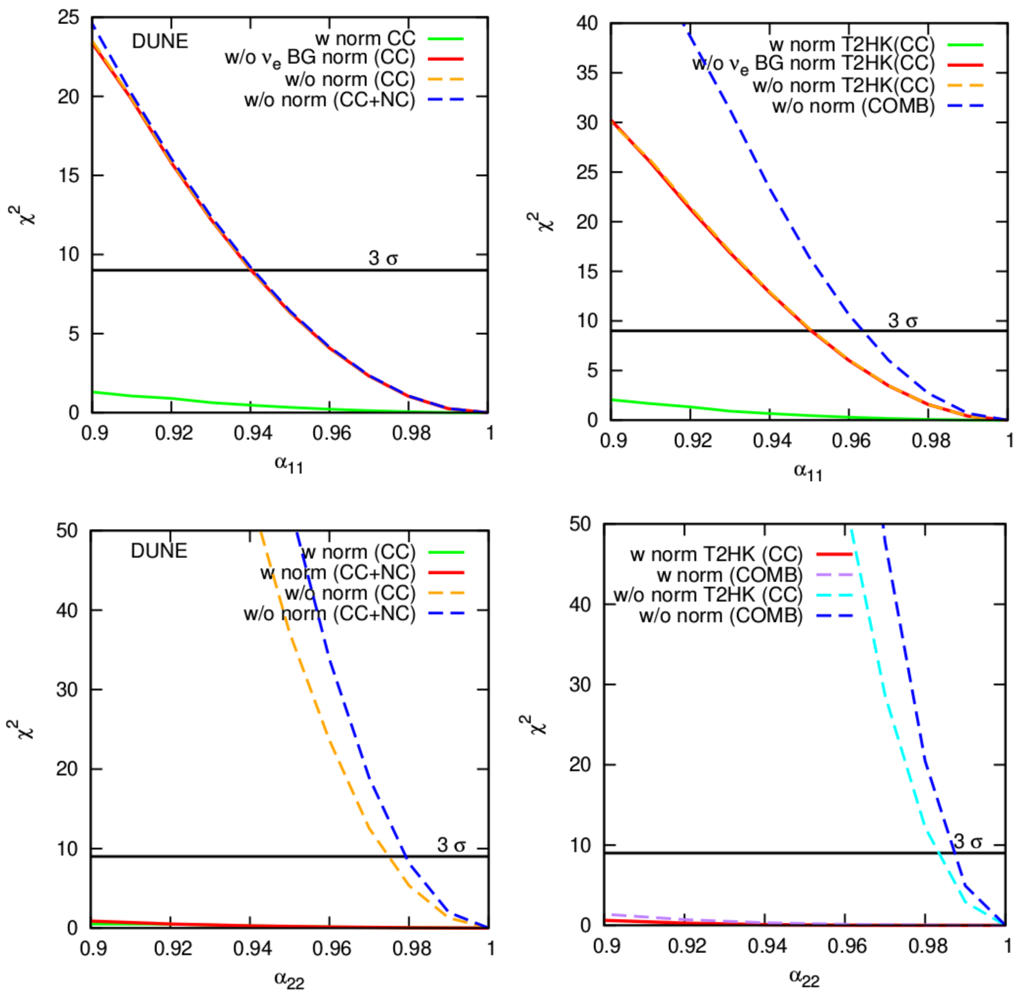

Figure 3.5: Constraints on α_{11} and α_{22} at DUNE and T2HK using CC measurements. We have also combined CC measurements at T2HK with the CC+NC measurements at DUNE. We call these combined results as 'COMB'.

Bound on α_{11}: It is observed from the upper panel of Fig. 3.5 that both DUNE and T2HK give loose constraints when we use the norm factor in the measurements. But, if the norm factor is not used in the ν_e (and $\bar{\nu}_e$) background, then we can see a significant enhancement in the sensitivity in both DUNE and T2HK. This enhancement is because of the decrease in ν_e (and $\bar{\nu}_e$) background due to the exclusion of the norm factor. This can also be confirmed from the probability plots in Fig. 3.3. Since the disappearance channel $\nu_e \rightarrow \nu_e$ depends only on α_{11} significantly hence the effect of marginalization of other parameters does not affect this channel. This point is also discussed in the subsection 3.3.4. Thus, it is important to point out that the ν_e (and $\bar{\nu}_e$) background is the main channel constraining the α_{11} parameter. The NC measurements of DUNE do not improve the bound on α_{11} and it is also apparent from the event discussions. From the plots we observe that DUNE can exclude all values of $\alpha_{11} \leq 0.94$ while T2HK can exclude all $\alpha_{11} \leq 0.95$ at 3σ CL. Thus, T2HK provides slightly better constraints on α_{11} compared to DUNE. Combinations of the two experiments can improve the constraint further and at 3σ CL, it can exclude all $\alpha_{11} \leq 0.965$.

Bound on α_{22}: We observe from the lower panel of Fig. 3.5 that the bound is very poor with norm for both DUNE and T2HK. Even after combining the two experiments, the bound on α_{22} does not improve with the norm factor. But it improves significantly when we do not include the norm factor. As shown in Fig. 3.4, the NC events at DUNE get reduced in presence of α_{22}. Therefore, when we add NC measurements with the CC measurements at DUNE, we observe a significant enhancement on the bound and all α_{22}, such that $\alpha_{22} \leq 0.978$ can be ruled out at 3σ CL. Finally, when we combine both the experiments we get better constraints on α_{22} and at 3σ CL, all $\alpha_{22} \leq 0.988$ can be ruled out. It is observed from Fig. 3.1 that the disappearance probability for α_{22} decreases significantly if the norm factor is not applied. Therefore, the constraint on α_{22} mainly comes from the disappearance channels.

Bound on α_{21}: From Fig. 3.6, we observe that the use of normalization factor does not affect the bounds on α_{21}, unlike α_{11} and α_{22}. But at DUNE, adding NC with CC

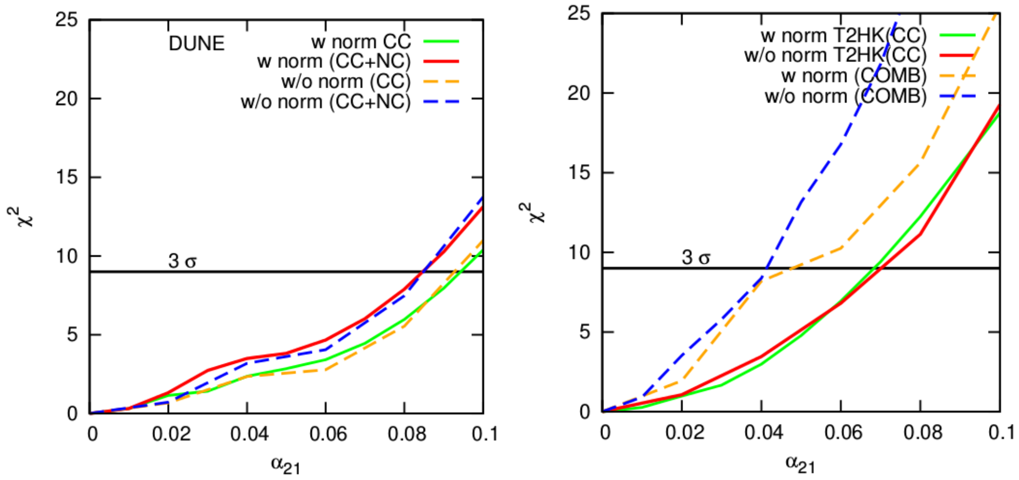

Figure 3.6: Constraints on α_{21} at DUNE and T2HK using the CC measurements. Also shown are the effects of combining CC and NC measurements at DUNE, and finally, the combination of DUNE (CC+NC) with the CC measurements at T2HK.

improves the constraints further. Combining T2HK with DUNE improves the constraints significantly from the individual results and at 3σ, the combined experiments can exclude all $\alpha_{21} \geq 0.04$ [6].

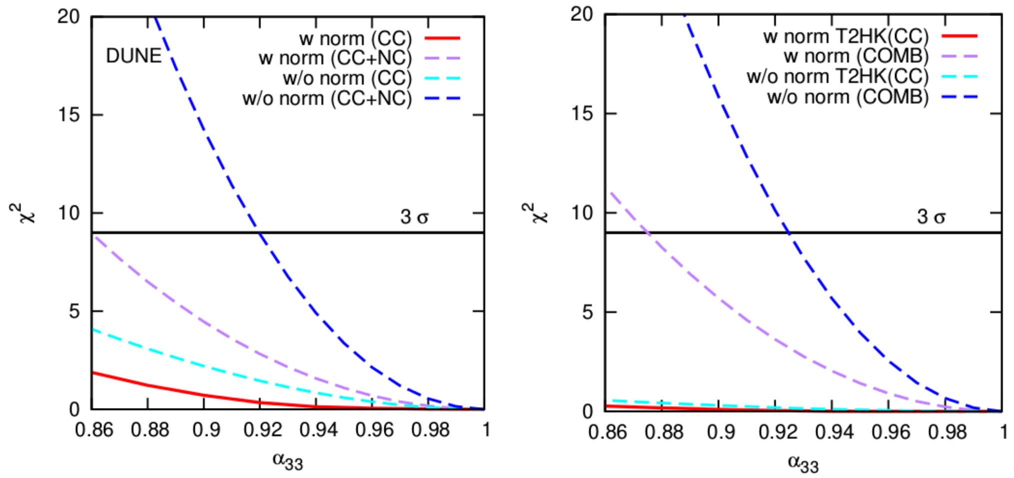

Figure 3.7: Constraints on α_{33} at DUNE and T2HK using CC measurements. We have also combined CC measurements at T2HK with the CC+NC measurements at DUNE.

Bound on α_{33}: From Fig. 3.7, we note that NC measurements at DUNE can improve the bounds on α_{33} compared to CC measurements. In presence of α_{33}, NC events decrease

[6] On α_{21}, tighter constraints can be achieved in short baseline experiments at Fermilab and related details can be found in [131].

significantly compared to the standard expected events as shown in Fig. 3.4. Therefore, combining CC measurements with NC measurements at DUNE improves the bound on α_{33} to a great extent. Without the norm factor, combining NC with CC measurements at DUNE constrains α_{33} such that at 3σ CL all values of $\alpha_{33} \leq 0.92$ are excluded. Use of the norm factor alleviates the sensitivity as the marginalization over α_{22} cancels the effect of α_{33} as shown by the pink line in the right panel of Fig. 3.3. For T2HK, CC measurements do not improve the bounds on α_{33}. DUNE CC measurements give better bounds on α_{33} compared to T2HK both with and without the norm factor due to the large matter effect. Combination of this with CC+NC measurements at DUNE slightly improves the bounds. The bound on α_{33} that comes from the combination is $\alpha_{33} \leq 0.925$ at 3σ CL.

The constraint on NU parameters derived in [109] rules out all $\alpha_{11} < 0.95$, $\alpha_{22} < 0.96$, $\alpha_{33} < 0.76$, and $\alpha_{21} > 0.026$ at $3\,\sigma$ CL. However, the combination of DUNE and T2HK can improve the bounds of diagonal NU parameters further. The combination of DUNE and T2HK without the norm factor can rule out all $\alpha_{11} < 0.965$, $\alpha_{22} < 0.988$, and $\alpha_{33} < 0.925$ at $3\,\sigma$ CL. But with the norm factor, the ability of DUNE and T2HK to constrain α_{11} and α_{22} is reduced significantly and we are not able to improve the constraints on these parameters. But with the norm factor, we can still improve the constraints on α_{33} significantly. The combination of DUNE and T2HK can rule out all $\alpha_{33} < 0.86$ at $3\,\sigma$ CL.

3.3.4 Effect of Marginalization and Normalization Factor

In Fig. 3.8, we have shown the ability of the appearance channels to constrain α_{11} parameter and also discuss the effect of marginalization of α_{21} parameter. In the left panel, we consider the appearance channels without any ν_e ($\bar{\nu}_e$) background but in the right panel, we show the effect of ν_e ($\bar{\nu}_e$) background in the χ^2 analysis. The solid line corresponds to the case where there is no normalization factor but the dotted line corresponds to the case with the normalization factor.

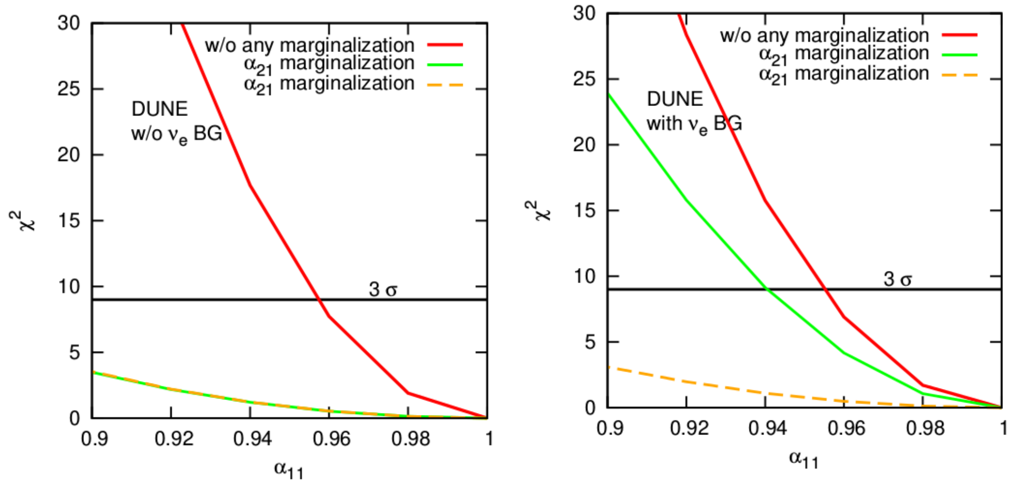

Figure 3.8: Constraint on α_{11} using the appearance channel. The solid line corresponds to the case without normalization factor and the doted line corresponds to the case with normalization factor.

We observe from the left panel that when we do not consider any marginalization then the appearance channels put tight constraint on α_{11}. But if we consider the marginalization over both α_{21} and ϕ_{21}, then the ability of the appearance channels to constrain α_{11} reduces drastically. In this case, the effect of normalization factor is not significant as shown by the green solid line and yellow dotted line. In the right panel, we have considered the ν_e ($\bar{\nu}_e$) background. Now, the disappearance channels ($\nu_e \to \nu_e$ or $\bar{\nu}_e \to \bar{\nu}_e$) do not depend on other parameters significantly except α_{11}. Therefore, when we perform the marginalization over α_{21} and ϕ_{21}, the contribution that comes from ν_e or $\bar{\nu}_e$ background is still significant as shown by the green solid line. But the use of the normalization factor cancels the effect of α_{11} on $\nu_e \to \nu_e$ (and $\bar{\nu}_e \to \bar{\nu}_e$) oscillation probability. Hence, with normalization it is not possible to put tight bounds on α_{11} as shown by the yellow doted line. The same argument holds for α_{22} where the main contribution comes from the disappearance channels $\nu_\mu \to \nu_\mu$ and $\bar{\nu}_\mu \to \bar{\nu}_\mu$ respectively.

Chapter 4

Effect of Non Unitarity on Neutrino Mass Hierarchy determination at DUNE, NOνA and T2K

The ordering of the neutrino masses is another critical unknown in the neutrino sector. In long baseline neutrino experiments, the earth matter effect plays an important role. The matter effect has opposite signs for the two hierarchies in the probability expression. So experiments like DUNE [78], NOνA [132], T2K [46, 47] etc. have the potential of distinguishing between the normal (NH, $m_3^2 - m_1^2 > 0$) and inverted (IH, $m_3^2 - m_1^2 < 0$) mass hierarchies.

There is an additional complication which may hamper the determination of the neutrino mass ordering - the possible presence of new physics like non unitarity which can give rise to additional CP phases. The new phases may mimic the leptonic CP phase and lead to further degeneracies. In this chapter, we explore the effect of non-unitarity on measurements of the neutrino mass ordering. This study has been performed in the context of the three long baseline (LBL) neutrino experiments T2K, NOνA and DUNE. We analyse the effect of non-unitary mixing on the oscillation probabilities for the given experiment baseline, and describe the mass hierarchy sensitivity for the individual experiments. We show that the hierarchy sensitivity decreases in the presence of non unitarity. The experiments are simulated using the standard long baseline package GLoBES [67, 68], which includes earth matter effects and relevant systematics for each experiment. We have used MonteCUBES [130] Non Unitarity Engine (NUE) with GLoBES while performing this analysis.

In the presence of non unitarity matrix, the electron neutrino appearance probability changes in vacuum, as explained in [63, 133]. The expression for $P_{\mu e}$ with NU can be written as

$$P_{\mu e} = (\alpha_{11}\alpha_{22})^2 P_{\mu e}^{3\times3} + \alpha_{11}^2\alpha_{22}|\alpha_{21}|P_{\mu e}^{I} + \alpha_{11}^2|\alpha_{21}|^2 \tag{4.0.1}$$

, where $P_{\mu e}^{3\times3}$ is the standard three flavor neutrino oscillation probability and $P_{\mu e}^{I}$ is the oscillation probability containing the extra phase due to non unitarity in the mixing matrix. $P_{\mu e}^{3\times3}$ above can be written as :

$$\begin{aligned} P_{\mu e}^{3\times3} = 4[\cos^2\theta_{12}\ \cos^2\theta_{23}\ \sin^2\theta_{12}\ \sin^2(\frac{\triangle m_{21}^2 L}{4E_\nu}) + \cos^2\theta_{13}\ \sin^2\theta_{13}\ \sin^2\theta_{23}\ \sin^2(\frac{\triangle m_{31}^2 L}{4E_\nu})] \\ + \sin(2\theta_{12})\ \sin\theta_{13}\ \sin(2\theta_{23})\ \sin(\frac{\triangle m_{21}^2 L}{2E_\nu})\ \sin(\frac{\triangle m_{31}^2 L}{4E_\nu})\ \cos(\frac{\triangle m_{31}^2 L}{4E_\nu} - I_{123}) \end{aligned} \tag{4.0.2}$$

And

$$\begin{aligned} P_{\mu e}^{I} = -2[\sin(2\theta_{13})\ \sin\theta_{23}\ \sin(\frac{\triangle m_{31}^2 L}{4E_\nu})\ \sin(\frac{\triangle m_{31}^2 L}{4E_\nu} + \phi_{21} - I_{123})] \\ - \cos\theta_{13}\ \cos\theta_{23}\ \sin(2\theta_{12})\ \sin(\frac{\triangle m_{21}^2 L}{2E_\nu})\sin(\phi_{21}) \end{aligned} \tag{4.0.3}$$

where $I_{123} = -\delta_{cp}$ and $\alpha_{21} = |\alpha_{21}|\exp(\phi_{21})$. Here we have observed that only four extra parameters from N^{NP} enter the vacuum probability expression for $P_{\mu e}$- the real parameters α_{11} and α_{22}, one complex parameter $|\alpha_{21}|$ and the phase associated with $|\alpha_{21}|$. In our analysis, we have not considered the effect of the third row elements of $\mathrm{N^{NP}}$ matrix (*i.e.*

α_{31}, α_{32} and α_{33}) as their contributions are negligible even in the presence of matter effect.

4.1 Simulation Parameters and Experiment details

In this chapter, we have studied the neutrino mass hierarchy sensitivity of three long baseline experiments- T2K (Tokai to Kamioka), NOνA (The NuMI[1] Off-axis ν_e Appearance experiment) and DUNE. The main goal of T2K is to observe $\nu_\mu \to \nu_e$ oscillations and to measure θ_{13} as well as leptonic CP violation while NOνA can measure the octant of θ_{23}, the neutrino mass hierarchy, θ_{13} and leptonic CP violation. DUNE, with its 1300 km baseline, can address all these issues with a higher degree of precision. Here, we fix the three-flavor neutrino oscillation parameters to their best fit values taken from [93]. Since the solar and reactor mixing angles are the most precisely measured, we take $\theta_{12} = 33.48^0$ and $\theta_{13} = 8.5^0$ respectively. For true NH (IH), the value of the two mass square differences are $\Delta m^2_{21} = 7.5\times10^{-5}$ eV^2 and $\Delta m^2_{31} = 2.457\times10^{-3}$ eV^2 (-2.449×10^{-3} eV^2) respectively. We consider the maximal value of θ_{23} as the true value i.e. $\theta_{23} = 45^o$. However, the physics conclusions drawn in this work are not going to change significantly even if we consider non maximal θ_{23} in 'data' and then marginalize it in 'fit' in the allowed 3σ range. The effect seen in the probability level at DUNE [See subsection 4.4.1] can be realized at more than 5σ CL only. This point is discussed in the text. The bounds on non unitarity parameters that we use in this work are: $\alpha^2_{11} \geq 0.989$, $\alpha^2_{22} \geq 0.999$ and $|\alpha_{21}|^2 \leq 0.0007$ at 90% C.L. [63]. The allowed range of ϕ_{21} is $[-\pi, \pi]$. We assume the limiting values of these NU parameters while generating the bi-probability and bi-event plots. In our χ^2 analysis, the central values of the allowed ranges are taken as the true values (unless stated).

[1]Neutrinos at the Main Injector

4.2 Bi-probability and Bi-event plots

In this section, we study the effect of non-unitarity at the probability level and explain the mass hierarchy degeneracy on the basis of bi-probability and bi-event plots. The bi-probability plots are shown in the P($\nu_\mu \to \nu_e$) - P($\bar{\nu_\mu} \to \bar{\nu_e}$) plane. In figure 4.1, the blue solid ellipse corresponds to the standard case with δ_{cp} varying from $-\pi$ to π. The gray and the cyan shaded regions (for Normal and Inverted Hierarchy respectively) correspond to the non-unitary case where the NU phase ϕ_{21} is also varied with δ_{cp} from $-\pi$ to π. The true values of the NU parameters (except ϕ_{21}) are fixed at their upper and lower bounds. For each δ_{cp}, due to the variation of ϕ_{21} in $[-\pi, \pi]$, we get a continuous band of ellipses. From figure 4.1, we draw the following conclusions:

- For DUNE at its peak energy i.e. $E = 2.5GeV$, it is observed that in the 3ν framework, ellipses corresponding to NH and IH are well separated. Even in the presence of NU there is no overlap between the ellipses that correspond to NH and IH. In the case of NOνA, there is some overlap between the blue ellipses corresponding to NH and IH and the overlap is more prominent in the presence of NU. In T2K, there is more overlap even for the 3ν case and with NU, the scenario worsens drastically. From this observation, we can conclude that only DUNE can discriminate between the two hierarchies at its peak energy even in the presence of NU.

The effect seen in figure 4.1 can also be verified from figure 4.2. These bi-event plots are generated assuming the peak energy of the three experiments i.e. for DUNE, E = 2.5 GeV, for NOνA, E = 1.6 GeV and for T2K, E = 0.6 GeV. But to draw some realistic conclusions, we consider the bi-event plots between the energy integrated total number of neutrino and anti-neutrino events (figure 4.3) for the three experiments. Here also, we fix the NU parameters to the boundary values and vary $\delta_{\rm CP}$ and ϕ_{21} from $-\pi$ to π.

- In DUNE, as in the bi-probability plots, the standard ellipses are well separated

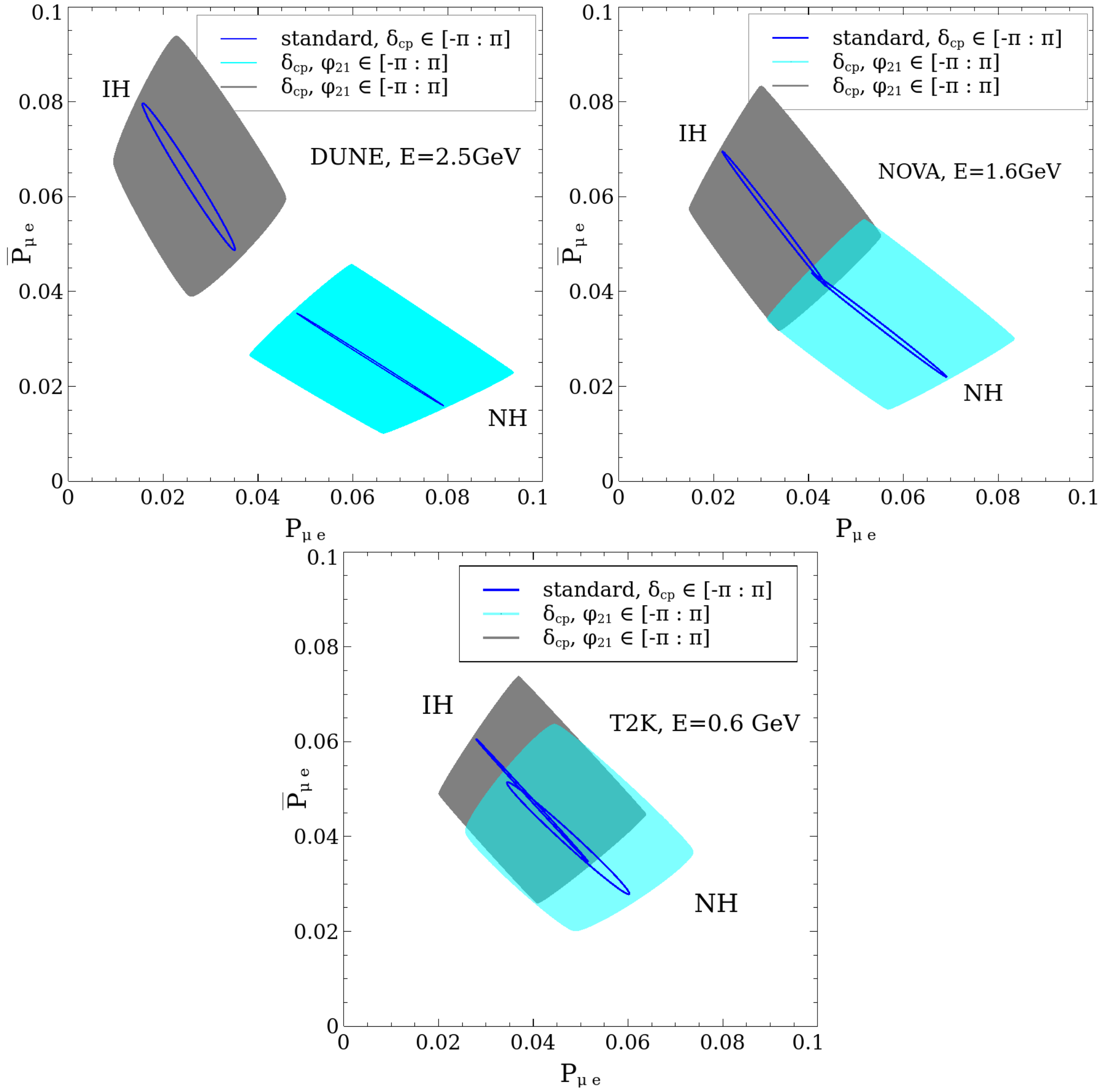

Figure 4.1: Bi-probability plots ($\bar{P}$ versus P): For DUNE, NOνA and T2k at their peak energy. The blue ellipse corresponds to the standard 3ν case and is obtained by varying $\delta_{\mathrm{CP}} \in [-\pi, \pi]$. The cyan and the gray bands show the effect of non unitarity for NH and IH when both the phase δ_{CP} and ϕ_{21} is varied from $-\pi$ to π and all other NU parameters are fixed at their limiting values i.e. $\alpha_{11} = 0.9945$, $\alpha_{22} = 0.9995$ and $|\alpha_{21}| = 0.0257$.

for NH and IH, indicating the ability of DUNE to resolve hierarchy degeneracy in the 3ν framework. But non unitarity induces a small degeneracy between the two hierarchies as there is a small overlapping region between the gray and the cyan bands. If we consider the co-ordinate (1000, 340) in the total events plot for DUNE, it lies in the overlapping region between the gray (IH) and the cyan (NH) band, and hence it is not possible to pinpoint the hierarchy near this co-ordinate. But due to the available spectral information as well as the high capability of the DUNE detector, DUNE may resolve the degeneracy seen in fig 4.3. On the other hand, a co-ordinate say (2000, 300) in the cyan band is far removed from the standard blue ellipse as well as the overlapping region, and hence any event corresponding to this point can be a hint of NU with NH. The situation gets worse in the case of NOνA and T2K. The standard 3ν ellipses that correspond to NH and IH show a similar behavior as the corresponding bi-probability plots. The overlapping is more prominent in the presence of NU. If the leptonic mixing matrix is non unitary, then these experiments are unable to discriminate between the two hierarchies. From this point of view, non unitarity of the leptonic mixing matrix has to be taken seriously.

- NOνA and T2K show another interesting feature. In NOνA, almost 50% of the standard ellipse in a particular hierarchy is a part of the NU induced band of ellipses in the opposite hierarchy. So in that region, any co-ordinate in the standard blue ellipse is not only a part of the standard NH ellipse, but also a part of both the gray and cyan bands. In T2K, similar behavior can be seen for a larger region of the parameter space.

From the above analysis, it is clear that in presence of NU, all the three experiments are incapable of discriminating between the two mass hierarchies. DUNE can tell us about the mass hierarchy when operating at its peak energy as seen from figure 4.1 and 4.2. Still there is tension between the two hierarchies in the presence of NU. In the next section, we discuss these issues in terms of sensitivity plots.

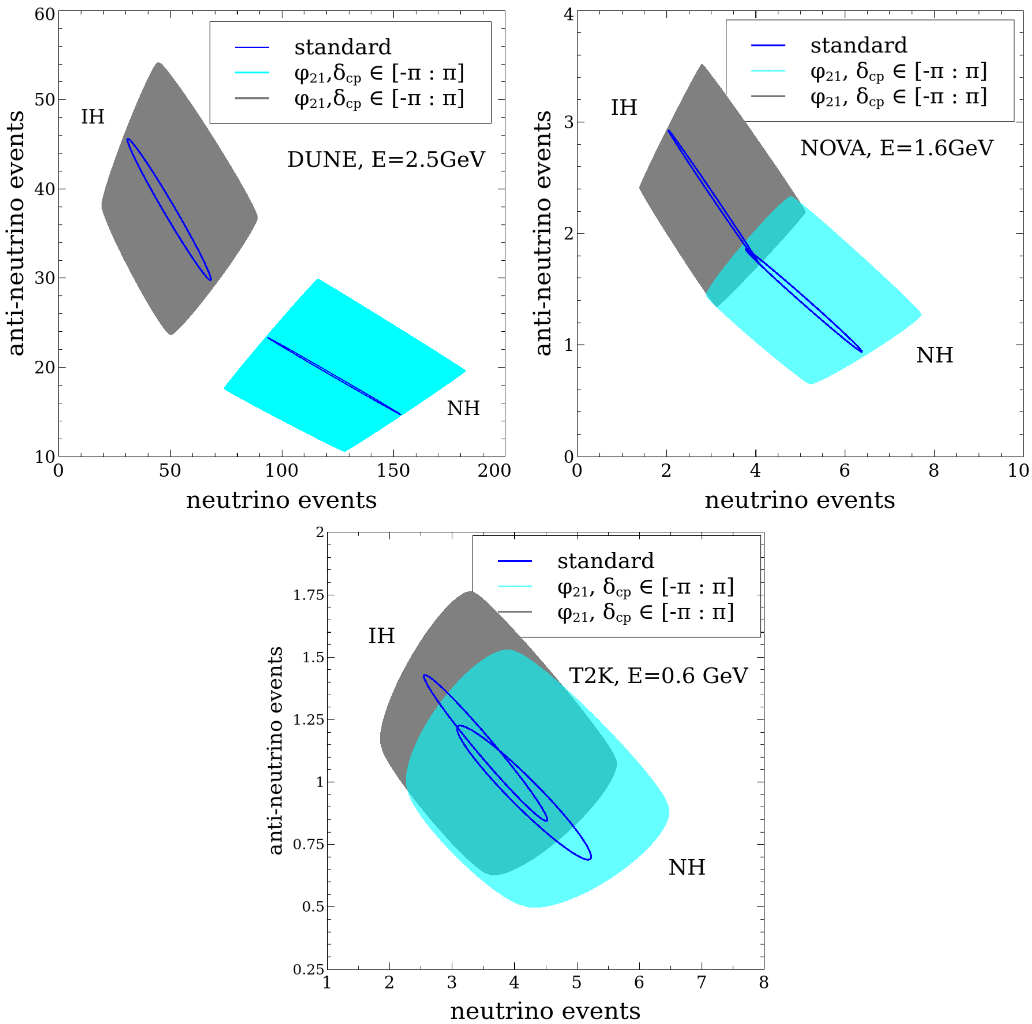

Figure 4.2: Bi-event plots For DUNE, NOνA and T2k at their peak energy. The blue ellipse corresponds to the standard 3ν case and is obtained by varying $\delta_{\mathrm{CP}} \in [-\pi, \pi]$. The gray and the cyan band show the effect of non unitarity when both the phase δ_{CP} and ϕ_{21} is varied from $-\pi$ to π and all other NU parameters are fixed to their limiting values.

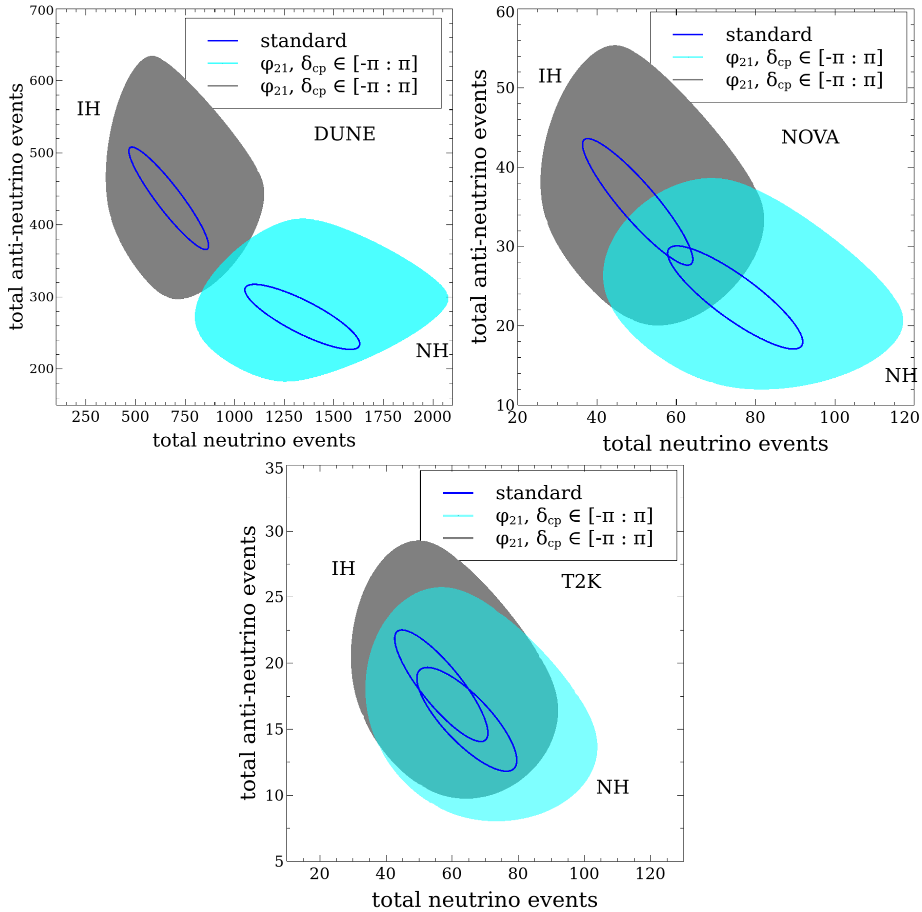

Figure 4.3: Energy dependent bi-event plots For DUNE, NOνA and T2k for their whole energy ranges i.e from 0.5 to 10 GeV, 0.4 to 4 GeV and 0.4 to 1.2 GeV respectively. All other variations are same as the previous plot (figure 4.2).

4.3 Sensitivity Studies

4.3.1 Statistical Details and χ^2 Analysis

The results presented in this section are based on χ^2 analysis where we have calculated $\Delta\chi^2$ by comparing the predicted spectra for the alternate hypothesis. For an assumed normal hierarchy as the true hierarchy, $\Delta\chi^2_{\rm MH}$ is defined as $\chi^2_{\rm NH} - \chi^2_{\rm IH}$. Similarly for an assumed true inverted hierarchy, $\Delta\chi^2_{\rm MH} = \chi^2_{\rm IH} - \chi^2_{\rm NH}$. Now, in terms of event rates, we can define it as:

$$\chi^2(\mathbf{n}^{\text{true}}, \mathbf{n}^{\text{test}}, f) = 2\sum_{i}^{N_{reco}}\sum_{j=1}^{2}(n_{i,j}^{\text{true}} ln\frac{n_{i,j}^{\text{true}}}{n_{i,j}^{\text{test}}(f)} + n_{i,j}^{\text{test}}(f) - n_{i,j}^{\text{true}}) + f^2, \tag{4.3.1}$$

where $\mathbf{n}$ represents event rate vectors in N_{reco} bins of reconstructed energy and f is the nuisance parameter. Here $n_{i,j}^{\text{true}}$ and $n_{i,j}^{\text{test}}(f)$ are the event rates that correspond to data and fit in the i^{th} bin. $j = 1$ is for neutrinos and $j = 2$ for anti-neutrinos. The number of bins are different for each experiment i.e. for DUNE there are 39 bins each of width 250 MeV in the energy range 0.5 to 10 GeV, for NOνA there are 28 bins of width 125 MeV in the energy range 0.5 to 4 GeV and for T2K, we have 20 bins of width 40 MeV in the range 0.4 to 1.2 GeV.

In the χ^2 calculation for the standard 3ν case, we have marginalised over the whole range of δ_{cp} from $-\pi$ to π in the 'fit'. To measure the hierarchy sensitivity, we fix our 'data' in a particular hierarchy and test the opposite hierarchy in the 'fit'. We have also marginalised over Δm^2_{31} in the 'fit' in its allowed 3σ ranges i.e. for an assumed NH as the true hierarchy, we vary Δm^2_{31} in the 'fit' assuming IH. Then we calculate the minimized χ^2 (i.e. χ^2_{min}) for each true δ_{cp} assuming the best fit values of the oscillation parameters as the true values. In the presence of NU, in addition to δ_{CP} and Δm^2_{31}, we have marginalised over all the non unitarity parameters in the 'fit' in their allowed ranges assuming the central values as the true values. For a particular true value of δ_{cp} we show the maximum and the minimum of χ^2_{min} which is obtained corresponding to a variation of the new phase ϕ_{21} in the 'data' from $-\pi$ to π.

4.3.2 Mass Hierarchy Sensitivity

Here we present our results for the mass hierarchy sensitivity of the three experiments in the presence of NU. We compare our results with the standard three flavor case. We also show the combined hierarchy sensitivity of the T2K and NOνA experiments in the presence of NU. In the plots, the blue line corresponds to the standard hierarchy sensitivity of these experiments while the gray band shows the effect of NU. The green line corresponds to the special case where ϕ_{21} is zero in both 'data' and 'fit' i.e. it shows the effect of the three absolute NU parameters α_{11}, α_{22} and $|\alpha_{21}|$. We have shown the sensitivity plots for both the hierarchies. We have combined both ν_e appearance and ν_μ disappearance channels in both the ν and $\bar{\nu}$ modes to utilize the full potential of each experiment towards mass hierarchy measurements. We can make the following observations from these plots:

- It is seen in the bi-probability and bi-event plots for DUNE that the ellipses corresponding to both the hierarchies are well separated in the standard three flavor case. figure 4.4 shows that for an assumed NH as the true hierarchy, DUNE can exclude the wrong hierarchy (i.e. IH in this case) at more than 5σ C.L. for all the true values of δ_{cp}. But in the presence of NU, for the true NH case, the mass hierarchy sensitivity decreases in the lower half plane (LHP, from $-\pi$ to 0) compared to the standard scenario. In the upper half plane (UHP, from 0 to π), the sensitivity with NU increases compared to the standard case for some fraction of true δ_{cp}, especially near $\delta_{cp} = \pi$.

  The effect of marginalizing over a large parameter space brings the χ^2 down and hence in the presence of NU, the mass hierarchy sensitivity decreases. In the case of NOνA, the hierarchy sensitivity in the standard scenario is already less than 3σ except near $\delta_{\mathrm{CP}} = -\pi/2$, while that of T2K is less than 2σ. In the presence of NU, this sensitivity further decreases especially in the LHP for an assumed true NH. IN the UHP, the hierarchy sensitivity in the presence of NU increases for some true combinations of δ_{CP} and ϕ_{21}, but the increase is not so significant.

- The dark red line of figure 4.4 and 4.5, representing the special case of true $\phi_{21} = 0$, lies within the gray band for all the three experiments as expected. In DUNE, the green plot, showing the sensitivity when both true and test $\phi_{21} = 0$ (if there is no

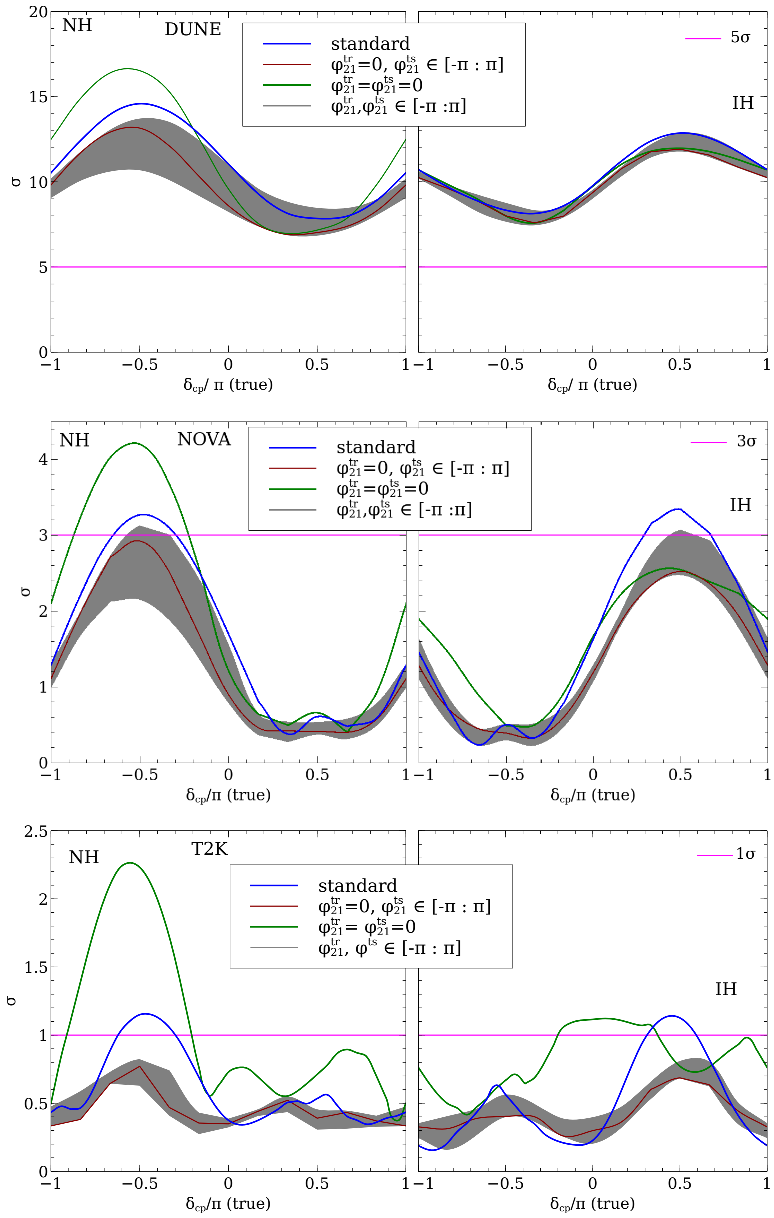

Figure 4.4: Mass hierarchy sensitivity plots for DUNE (5+5), NoνA (3+3) and T2K (3+3) for both the hierarchies. The blue line represents the standard mass hierarchy sensitivity. The gray band corresponds to the variation of true δ_{CP} and ϕ_{21} (both ϕ_{21}^{tr} (true) and ϕ_{21}^{ts} (test)) from $[-\pi, \pi]$. The dark red line represents the case when $\phi_{21}^{tr} = 0$ but ϕ_{21}^{ts} is varied from $[-\pi, \pi]$. The green line shows the effect of the non zero absolute parameters for $\phi_{21}^{tr} = \phi_{21}^{ts} = 0$. For all the cases with NU, we assume the central values of the NU parameters as the true values.

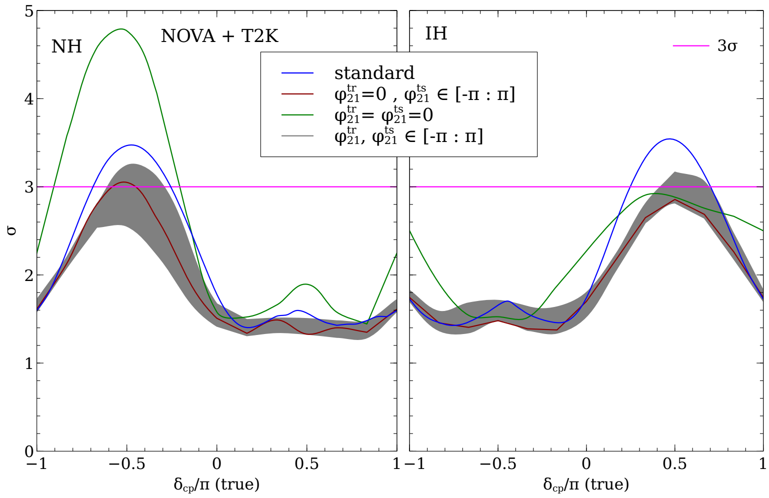

Figure 4.5: Mass hierarchy sensitivity plots for the combination of NOνA (3+3) and T2K (3+3) in both the hierarchies. The blue line represents the standard mass hierarchy sensitivity. The gray band corresponds to the true variation of $\delta_{\rm CP}$ and ϕ_{21} from $[-\pi, \pi]$.

new physics phase), shows higher sensitivity for $\delta_{\rm CP} \in [-\pi, -\pi/6]$ and $\delta_{\rm CP} > 1.45\pi$ than the standard case for an assumed true NH. But in between $\delta_{\rm CP} \in [-\pi/6, 1.45\pi]$ the green plot dips below the standard 3ν scenario. In the case of NOνA, the green plot drops compared to the standard 3ν sensitivity only for a small fraction of $\delta_{\rm CP}$ around 0 and 1.5π for an assumed true NH. The sensitivity shoots up to 3σ for more than 70% of true $\delta_{\rm CP}$ in the LHP. In the case of T2K, the green line is always higher than the standard sensitivity for assumed true NH. For more than 70% of true $\delta_{\rm CP}$ in the LHP, sensitivity is higher than 1σ.

- For an assumed true IH, DUNE can exclude NH for all values of true δ_{cp} at more than 5σ C.L.. Even in the presence of NU, DUNE can resolve the neutrino mass hierarchy at more than 5σ C.L. irrespective of the true hierarchy. But in the case of NOνA and T2K, the sensitivity decreases with NU and T2K is the most affected.

- Figure 4.5 shows the combined hierarchy sensitivity of T2K and NOνA. The sensitivity increases slightly compared to their individual sensitivities. In the presence of NU, some fraction of $\delta_{\rm CP}$ around $-\pi$ (π) has a sensitivity more than 3σ in the NH (IH) case. We have not combined DUNE data with T2K and NOνA as its individual sensitivity is more than 5σ.

4.3.3 Mass Hierarchy Discovery Reach

In this section, we show the mass hierarchy discovery reach of these experiments in the presence of NU. As the DUNE experiments can rule out the wrong hierarchy with more than 5σ C.L. even in the presence of NU, here we present the discovery potential of T2K and NOνA and their combinations only. We have generated these results assuming the maximum deviation from unitarity, i.e. the true values of the NU parameters are fixed at their boundary values. The contours are shown in $\delta_{\rm CP} - \phi_{21}$ (true) parameter space and are drawn at 1 d.o.f.. The regions bounded by the contours are the allowed regions in this parameter space.

In figure 4.6, we show the MH discovery reach of NOνA and T2K for both NH and IH. For each true Δm^2_{31} in NH (IH), we vary test Δm^2_{31} in IH (NH). We observe that NOνA can probe NH at 3σ C.L. for some true combinations of $\delta_{\rm CP}$ and ϕ_{21}. The region outside the blue contours is the excluded region where 3σ discovery of MH is not possible. The 3σ allowed region shrinks for the case where assumed true hierarchy is inverted. In the case of T2K, only a 1σ discovery is possible with NU for both the hierarchies. In figure 4.7, we have presented our results for the combined case. Here we observe that adding T2K data with NOνA can slightly improve the discovery potential of NOνA. The size of the blue contours increases slightly for both the hierarchies compared to NOνA, which in turn means that for more true values of $\delta_{\rm CP}$ and ϕ_{21}, the combined setup can discover MH at 3σ C.L..

In fig.4.8, we have shown the effect of marginalisation on θ_{23} for maximal and non maximal true θ_{23} and have observed that the physics conclusions drawn in this work are not going to change with non maximal true θ_{23}. Also from the contour plots in the lower panel, it is confirmed that the NU effect seen in probability level at DUNE (subsection 4.4.1) can be lifted by combining appearance and disappearance channels both in neutrino and anti-neutrino mode.

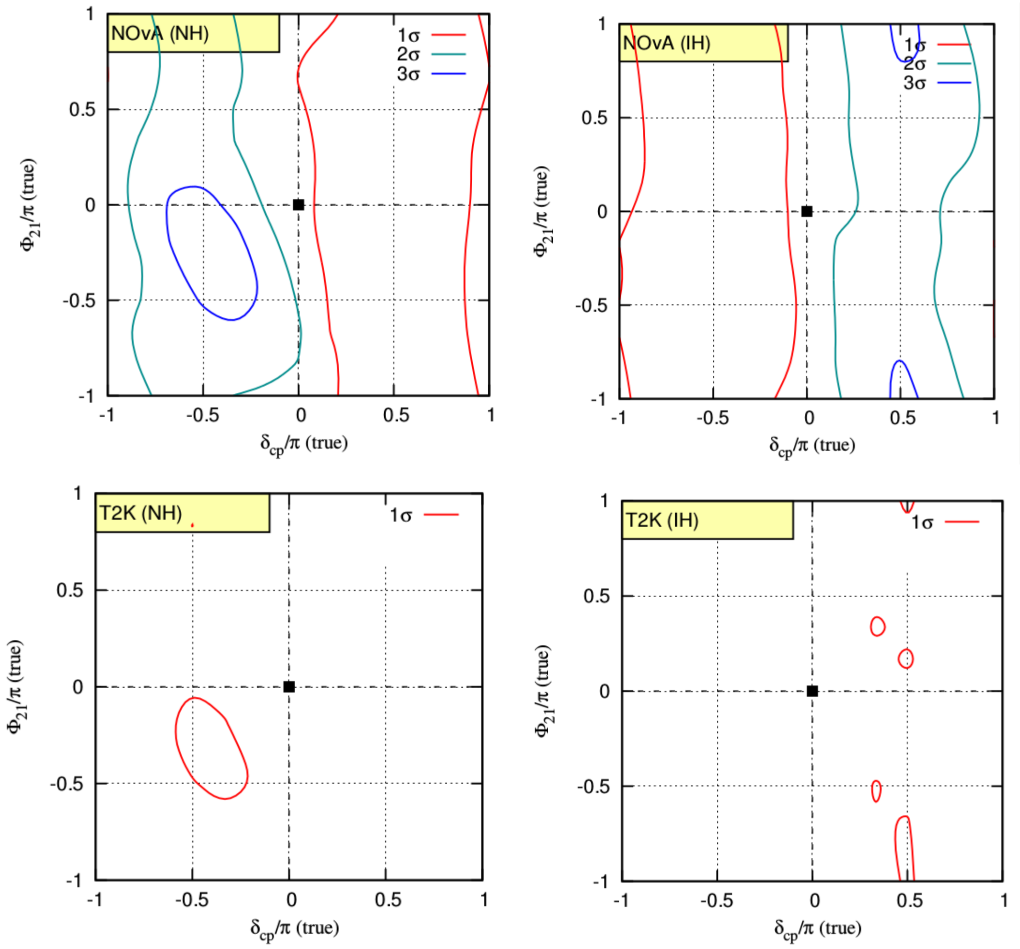

Figure 4.6: Mass hierarchy discovery potential of NOνA (3+3) and T2K (3+3) for both the hierarchies. Here we assume the boundary values of the NU parameters as the true values i.e.α_{11} = 0.9945, α_{22} = 0.9995 and $|\alpha_{21}|$ = 0.0257.

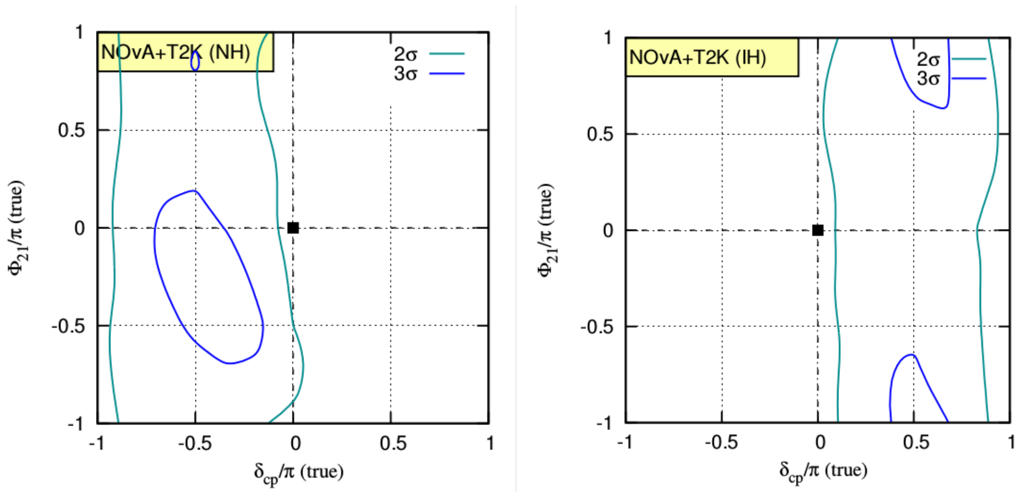

Figure 4.7: Mass hierarchy discovery potential of the combined experiments : We combine NovνA (3+3) and T2K (3+3) data in both the hierarchies. Here also, we assume the boundary values of the NU parameters as the true values i.e.α_{11} = 0.9945, α_{22} = 0.9995 and $|\alpha_{21}|$ = 0.0257.

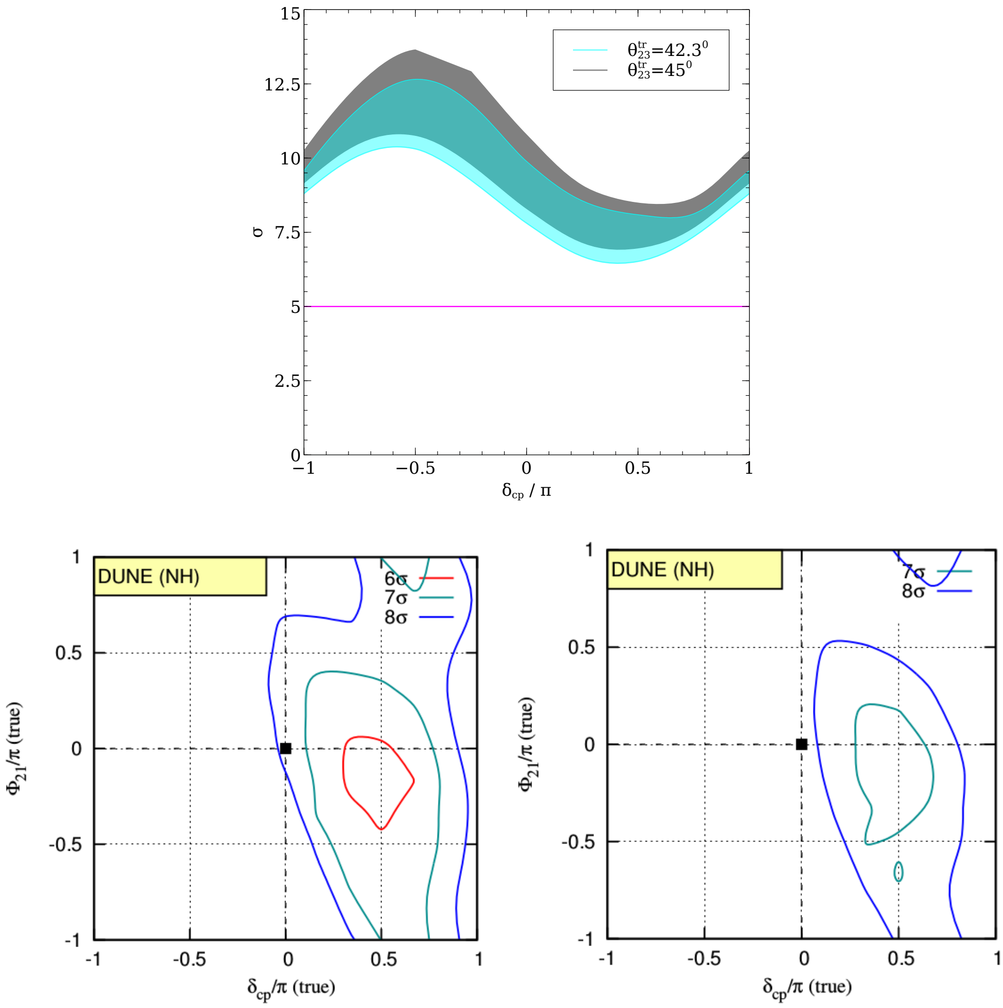

Figure 4.8: Here, the upper panel shows the mass hierarchy sensitivity of DUNE for true $\theta_{23} = 45^0$ and $\theta_{23} = 42.3^0$ marginalising θ_{23} in the allowed 3σ range in fit. The lower panel shows the contour plots for $\theta_{23} = 38.3^0$ (left) and $\theta_{23} = 42.3^0$ (right) in the true $\delta_{CP} - \phi_{21}$ parameter space.

4.4 Results

In this chapter, we have attempted to analyse the mass hierarchy sensitivity of the long-baseline experiments T2K, NOνA and DUNE in the presence of non-unitarity. Below we summarize the salient results of this work:

- The presence of non-unitarity leads to a strong degeneracy between the standard 3ν case and the NU induced case in estimating the neutrino mass hierarchy for all three superbeam experiments at the level of oscillation probabilities. An analysis of the bi-probability plots of the three experiments shows that only DUNE can discriminate between the two hierarchies at its peak energy even in the presence of NU, while T2K and NOνA show significant overlaps between the NH and IH ellipses. Also, for certain values of δ_{cp} and the NU phase in all three experiments, it is not possible to specify whether the value arises from the standard case or the NU induced case.

- From the bi-event plots for the three experiments, we observe that if analyzed at the peak energies of the respective experiments, DUNE can distinguish between the hierarchies even in the presence of NU, while NOνA and T2K are unable to do so because of their shorter baselines and less matter effects. If an integration over the energy ranges of the experiments is taken into account, then DUNE also suffers from a small overlap between the hierarchies with NU. Further, for NOνA and T2K in the presence of NU, there is a degeneracy in the same hierarchies between the standard and the NU induced hierarchy measurements, as well as a degeneracy between NH (IH) in the 3ν scenario and IH (NH) in the NU induced scenario. Also, with NU any of these experiments may misinterpret a non unitary event as a standard 3ν event. Thus at the event level, all the three experiments are incapable of discriminating between the mass hierarchies with NU, except for DUNE at its peak energy.

- The results for the sensitivity to the mass hierarchy show that with NH as the true hierarchy, DUNE can exclude the wrong hierarchy at more than 5σ C.L. for all true values of δ_{cp}. But in the presence of NU, for the true NH case, the mass hierarchy sensitivity decreases in the LHP ($-\pi$ to 0) compared to the standard scenario. In the UHP (0 to π), the sensitivity with NU increases compared to the standard case for some combination of true δ_{cp} and ϕ_{21}, especially near $\delta_{cp} = \pi/2$. In the case of NOνA, the hierarchy sensitivity in the standard scenario is already less than 3σ except near $\delta_{\rm CP} = -\pi/2$, while that of T2K is less than 2σ. In the presence of NU, this sensitivity further decreases especially in the LHP for an assumed true NH. IN the UHP, the hierarchy sensitivity in the presence of NU increases for some true combinations of $\delta_{\rm CP}$ and ϕ_{21}, but the increase is not significant.

- For true IH, DUNE can exclude NH for all values of true δ_{cp} at more than 5σ C.L. Even in the presence of NU, DUNE can resolve the neutrino mass hierarchy at more than 5σ C.L. irrespective of the true hierarchy. But in the case of NOνA and T2K, the sensitivity decreases with NU and T2K is the most affected.

- The combined hierarchy sensitivity of T2K and NOνA increases slightly compared to their individual sensitivities. In the presence of NU, some fraction of $\delta_{\rm CP}$ around $-\pi/2$ ($\pi/2$) has a sensitivity more than 3σ in the NH (IH) case.

- Finally, the mass hierarchy discovery reach of NOνA and T2K is studied and it is observed that NOνA can probe NH at 3σ C.L. for some true combinations of $\delta_{\rm CP}$ and ϕ_{21}. The 3σ allowed region shrinks for the case true IH. In the case of T2K, only 1σ discovery is possible with NU for both the hierarchies. Adding T2K data with NOνA can slightly improve the discovery potential of NOνA. The combined setup can discover MH at 3σ C.L.. for a greater range of true values of $\delta_{\rm CP}$ and ϕ_{21}. We have not studied the discovery reach for DUNE since it has already been observed that it can rule out the wrong hierarchy at more than 5σ C.L. even with NU.

- We have carefully checked our results (figure 4.4 and 4.6) for non maximal θ_{23} values (with the present best fit value and and a benchmark value of $\theta_{23} = 38.3^0$ as the true value), marginalizing over the whole allowed range of θ_{23} in the fit for DUNE (for true NH). In figure 4.8, we depict the DUNE hierarchy sensitivity showing the comparison between maximal and non-maximal θ_{23} (best fit value $\theta_{23} = 42.3^0$). In the lower panel, we have shown the contour plots for true $\theta_{23} = 42.3^0$ (left) and true $\theta_{23} = 38.3^0$ (right). We have chosen $\theta_{23} = 38.3^0$ just to show the maximal possible correlation between ϕ_{21} and δ_{cp} The contour plot with $\theta_{23} = 42.3^0$ is consistent with the sensitivity plot shown in the upper panel. We observe from the upper panel that the differences between the sensitivity for maximal and non-maximal θ_{23} are very small and in all cases, the capability of DUNE to exclude the wrong IH is much more than 5σ for all true values of δ_{cp}. This is also the reason why the whole $\delta_{cp} - \phi_{21}$ parameter space is excluded for DUNE for assumed true NH/IH at more than 5σ C.L., as confirmed by the contour plots in the lower panel. The reason for this is as follows: the probability plots shown in subsection 4.4.1 are only in the ν mode. But when we combine both ν and $\bar{\nu}$ in appearance and disappearance modes to calculate the sensitivity, NU hampers the sensitivity at DUNE at a higher confidence level only. And also, as pointed out in Section III, the physics conclusions drawn here remain unchanged even if we consider non maximal θ_{23} in 'data' and then marginalize it in 'fit' in the allowed 3σ range.

We conclude that the presence of non-unitarity in the neutrino mass matrix can significantly affect the potential of the experiments NOνA and T2K to resolve the neutrino mass hierarchy. The experiment DUNE is less affected due to its longer baseline and consequent large matter effects, which results in a resolution of the hierarchy degeneracy for DUNE even in the presence of non-unitarity at its peak operating energy. It is worthwhile to analyze other long baseline experiments to understand more thoroughly the effect of non-unitarity on their capability for determining the mass hierarchy.

4.4.1 Effect of θ_{23} Variation

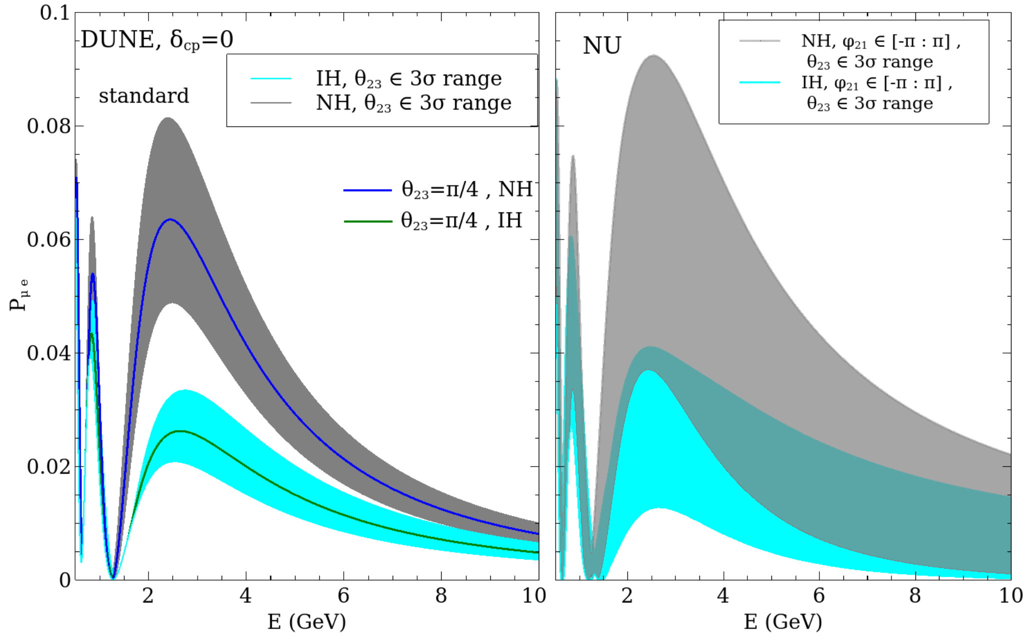

Figure 4.9: $P_{\mu e}$ vs Energy plots for DUNE to show the effect of θ_{23} variation. In the left (right) panel, we show the variation in standard (with NU) case. We consider the boundary values of the NU parameters here. The blue (green) line represents the $P_{\mu e}$ vs E for $\theta_{23} = 45^0$ in NH (IH). The gray (cyan) band shows the variation of θ_{23} in 3σ allowed range in NH (IH) mode.

In this study we have assumed the maximal value of the atmospheric neutrino mixing angle θ_{23}. However it can be shown at the probability level that there is a significant effect of varying θ_{23} on the oscillation probability, which has the potential of affecting the results for the hierarchy sensitivity. To demonstrate this we present in figure 4.9 the probability $P_{\mu e}$ as a function of the neutrino energy for DUNE, incorporating a variation in θ_{23} depicted by the grey (cyan) band for true NH (IH) in the figure. Here we have compared the standard case with the NU case for $\delta_{CP} = 0$. In the left panel, we vary θ_{23} over its current 3σ range for both the hierarchies and see that the probabilities for NH and IH are still well separated. But in the presence of NU (right panel), if we vary over θ_{23}, there is a large overlapping region between the probabilities for NH and IH. This indicates that a more rigorous procedure should be followed to take into account the current uncertainty in θ_{23} while performing this analysis though the conclusion drawn above remains unchanged.

Chapter 5

Correlations and degeneracies among the NSI parameters with tunable beams at DUNE

In the previous chapter, we consider two new physics scenarios namely light sterile neutrino and non unitarity of the leptonic mixing matrix. In this chapter we consider how we can improve bounds on NSI parameters using tunable beams at DUNE. In a seminal paper in 1978, Wolfenstein first proposed the possibility that NSI could be responsible for conversion of a given neutrino flavour to another even if neutrinos were massless [17]. However, thanks to the wealth of data accumulated by a variety of oscillation experiments covering different energies and baselines, we now have a fairly clear picture that neutrino oscillations occur due to nonzero neutrino masses.

On the theoretical side, neutrino oscillations require non-zero masses while neutrinos are massless in the SM. This implies that one needs to go beyond the SM in order to explain the results of oscillation experiments. The minimal way is to have a new physics model which can give rise to nonzero neutrino masses but the interactions are still described by SM. Once we invoke new physics to accommodate neutrino masses, it is only natural to consider the possibility that the neutrino interactions are described by NSI (as was proposed by Wolfenstein [17]). Clearly, a dominant contribution from such interactions is ruled out by the present data [44, 134–136]. However a subdominant contribution cannot be ruled out given the present accuracy of the neutrino oscillation experiments. Therefore, the idea proposed by Wolfenstein does not hold true in totality in the current times yet his insight remains in the form of subdominant effects due to NSI on neutrino oscillations.

The fact that parameter degeneracies crop up in the presence of standard interactions (SI) has been well recognized since the past two decades or so [90, 137–141]. Identification and resolution of parameter degeneracies is crucial for a clean determination of the oscillation parameters. Besides, any new physics sector (such as NSI considered in the present work) introduces a multitude of parameter degeneracies apart from those in the standard case and the structure of parameter degeneracies is far more complex. There has been a vast body of work done on NSI and neutrino oscillations. For a comprehensive recent review on the topic of NSI in the context of neutrino oscillations, we refer the reader to [142].

It should be noted that the studies carried out so far on constraining NSI terms on DUNE has invariably utilized the standard low energy (LE) flux that peaks around the first oscillation maximum for $P_{\mu e}$ *i.e.*, around $2-3$ GeV. We advance in this direction by incorporating different beam tunes at DUNE and understand the role of beam tunes in constraining the NSI parameters. In a recent work, high energy beams have been shown to be helpful in distinguishing the NSI scenario from the standard three neutrino scenario [143]. While the new physics context of the present study is that of propagation NSI, our approach is valid for a variety of new physics models.

The chapter is organised as follows. In Sec. 5.1, we give the theoretical introduction to neutral current (NC) NSI which is the new physics scenario considered in the this chapter. We also mention the present constraints on the NSI terms. In Sec. 5.2, we describe the numerical simulation procedure as well as introduce the beam tunes used. In

Oscillation Parameter	Best-fit value	3σ range
θ_{12} [°]	34.5	31.5 - 38.0
θ_{13} [°]	8.45	8.0 - 8.9
θ_{23} [°]	47.7	41.8 - 50.7
δ/π	-0.68	$[-1, -0.06]$ and $[0.87, 1]$
Δm^2_{21} [10^{-5} eV^2]	7.55	7.05 - 8.14
Δm^2_{31} [10^{-3} eV^2]	+2.50	2.41 - 2.60

Table 5.1: Neutrino mass and mixing parameters obtained from the global fit to neutrino oscillation data [134, 135]

.

subsection 5.3.1, we first discuss the impact of individual NSI terms on the behaviour of probabilities ($P_{\mu e}$ and $P_{\mu\mu}$) as functions of δ. In subsections 5.3.2 and 5.3.3, we analyze the behaviour of the probability difference between NSI and SI as a function of energy as well as δ. In Sec. 5.4, we do a comparative $\Delta\chi^2$ analysis to discuss in detail how the higher energy beams in conjunction with the standard low energy beam impact the sensitivities of parameters. In section 5.5 and 5.6, we have given the relevant probability expressions that aid in understanding our results. Section 5.7 contains the SI-NSI event difference plot for some representative choice of parameters.

5.1 Model : Nonstandard interaction during propagation

The new physics scenario considered in the present work is that of propagation NSI which impacts the propagation of neutrinos. Such a scenario can be described by a dimensionsix operator involving four fermions,

$$\mathcal{L}_{NSI} = -2\sqrt{2}G_F \varepsilon^{fC}_{\alpha\beta}(\bar{\nu}_\alpha\gamma^\mu P_L \nu_\beta)(\bar{f}\gamma_\mu P_C f) \tag{5.1.1}$$

where $\alpha, \beta = e, \mu, \tau$ indicate the neutrino flavor, f denotes the matter fermions, e, u, d. The new NC interaction terms can impact the neutrino oscillation physics via flavour changing interaction or flavour preserving interaction. From a phenomenological point of view, only the sum (incoherent) of all the individual contributions (from different scatterers such as e, u or d) contributes to the coherent forward scattering of neutrinos on matter. Normalizing to n_e, the effective NSI parameter for neutral Earth matter[1] is given by

$$\varepsilon_{\alpha\beta} = \sum_{f=e,u,d} \frac{n_f}{n_e}\varepsilon^f_{\alpha\beta} = \varepsilon^e_{\alpha\beta} + 2\varepsilon^u_{\alpha\beta} + \varepsilon^d_{\alpha\beta} + \frac{n_n}{n_e}(2\varepsilon^d_{\alpha\beta} + \varepsilon^u_{\alpha\beta}) = \varepsilon^e_{\alpha\beta} + 3\varepsilon^u_{\alpha\beta} + 3\varepsilon^d_{\alpha\beta} \tag{5.1.2}$$

where n_f is the density of fermion f in medium crossed by the neutrino and n refers to neutrons. Also, $\varepsilon^f_{\alpha\beta} = \varepsilon^{fL}_{\alpha\beta} + \varepsilon^{fR}_{\alpha\beta}$ which encodes the fact that NC type NSI matter effects are sensitive to the vector sum of NSI couplings. Only the vector part adds up coherently. Contribution of the axial vector part depends on the spin of the particle. Hence it will not contribute in the coherent process as the net spin of the system is zero.

In the presence of NSI, the Hamiltonian in the effective Schrodinger -like equation governing neutrino evolution can be expressed as

$$\mathcal{H} = \frac{1}{2E}\left\{U\begin{pmatrix} 0 & & \\ & \Delta m^2_{21} & \\ & & \Delta m^2_{31}\end{pmatrix}U^\dagger + a(x)\begin{pmatrix} 1+\varepsilon_{ee} & \varepsilon_{e\mu} & \varepsilon_{e\tau} \\ \varepsilon_{e\mu}{}^\star & \varepsilon_{\mu\mu} & \varepsilon_{\mu\tau} \\ \varepsilon_{e\tau}{}^\star & \varepsilon_{\mu\tau}{}^\star & \varepsilon_{\tau\tau}\end{pmatrix}\right\}, \tag{5.1.3}$$

where Δm^2_{ij} are the mass-squared differences. Here $a(x) = 2\sqrt{2}EG_F n_e(x)$ is the standard charged current (CC) potential due to the coherent forward scattering of neutrinos, n_e is

[1]For neutral Earth matter, there are two nucleons (one proton and one neutron) per electron.

the electron number density and $\varepsilon_{\alpha\beta}$ ($\equiv |\varepsilon_{\alpha\beta}|\, e^{i\varphi_{\alpha\beta}}$) are complex NSI parameters. U is the PMNS three flavour neutrino mixing matrix.

We now mention the constraints on the NC NSI parameters. The combination that enters oscillation physics is given by Eq. 5.1.2. Assuming that the errors on individual NSI terms are uncorrelated, model-independent bounds on NC NSI terms $\varepsilon_{\alpha\beta}$ were given in Ref. [144]. In particular, one obtains the following:

$$\varepsilon_{\alpha\beta} \lesssim \left\{ \sum_{C=L,R} [|\varepsilon^{eC}_{\alpha\beta}|^2 + 3|\varepsilon^{uC}_{\alpha\beta}|^2 + 3|\varepsilon^{dC}_{\alpha\beta}|^2] \right\}^{1/2} , \tag{5.1.4}$$

which leads to

$$|\varepsilon_{\alpha\beta}| \;<\; \begin{pmatrix} 4.2 & 0.33 & 3.0 \\ 0.33 & 0.068 & 0.33 \\ 3.0 & 0.33 & 21 \end{pmatrix} . \tag{5.1.5}$$

for neutral Earth matter. The values of $\varepsilon^{eC}_{\alpha\beta}$, $\varepsilon^{uC}_{\alpha\beta}$, and $\varepsilon^{dC}_{\alpha\beta}$ are derived using neutrino scattering experiments, LEP data, atmospheric neutrino experiments as in [145–147]. Direct experimental constrains from neutrino experiments on NSI parameters are more restrictive. The SK NSI search in atmospheric neutrinos crossing the Earth found no evidence in favour of NSI and the study led to upper bounds on NSI parameters [148] given by $|\varepsilon_{\mu\tau}| < 0.033$, $|\varepsilon_{\tau\tau} - \varepsilon_{\mu\mu}| < 0.147$ (at 90% CL) in a two flavour hybrid model [59]. The off-diagonal NSI parameter $\varepsilon_{\mu\tau}$ is constrained $-0.20 < \varepsilon_{\mu\tau} < 0.07$ (at 90% CL) from MINOS data in the framework of two flavour neutrino oscillations [149, 150].

In what follows, we shall adopt a numerical approach to discuss the impact of various NSI parameters. For the sake of simplicity and clarity, we consider one NSI parameter at a time. Wherever analytic description is feasible, we give approximate analytic expressions which are valid in the present context and additional plots which help in understanding the results obtained numerically (for more details, see section 5.5 and 5.6).

5.2 Simulation procedure and beam tunes

In order to simulate DUNE, we use the GLoBES package [67, 68] with the most recent DUNE configuration file provided by the collaboration [77] and implement the density profile given by Preliminary Reference Earth Model (PREM) [151]. We assume a total runtime of 7 years with 3.5 years in the neutrino mode and another 3.5 years in the antineutrino mode.

Parameter	LE	ME
Proton beam	$E_{p^+} = 80$ GeV	$E_{p^+} = 120$ GeV
	1.07 MW	1.2 MW
Focusing	2 NuMI horns, 230kA, 6.6 m apart	
Target location	-25 cm	-1.0 m
Decay pipe length	204 m	250 m
Decay pipe diameter	4 m	4 m

Table 5.2: Beamline parameters assumed for the different design fluxes used in our sensitivity calculations [77, 152]. The target is a thin Be cylinder 2 interaction lengths long. The target location is given with respect to the upstream face of Horn 1. The LBNF neutrino beamline decay pipe length has been chosen to be 194 m. Decay pipe lengths of up to 250 m could be accommodated on the Fermilab site and were an option in previous designs of the beamline.

We consider two beam tunes obtained from a G4LBNF simulation [153,154] of the LBNF beam line using NuMI-style focusing.

LE beam The standard ν_μ beam which peaks around a relatively lower energy of ~ 2.5 GeV (corresponding to the first oscillation maximum for the $\nu_\mu \to \nu_e$ appearance channel) is referred to as an LE beam in our analyses. It is generated by an 80 GeV proton beam delivered at 1.07 MW with protons on target (pot) of 1.47×10^{21}.

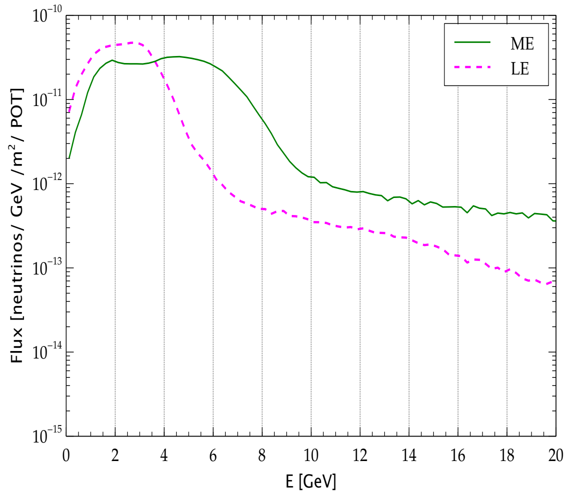

Figure 5.1: The neutrino fluxes (LE and ME) used in the present work. LE beam refers to the standard flux generated by an 80 GeV proton beam as used in [77]. ME beam refers to the flux peaking at a higher energy. See Table 5.2 for more details.

ME beam The second beam is has the characteristic that it is larger at higher energies ($\gtrsim$ 4 GeV onwards) and we refer to this beam as medium energy (ME) beam. The ME beam is generated by a 120 GeV proton beam delivered at 1.2 MW with a pot of 1.1×10^{21}.

Both the LE and ME fluxes are shown in Fig. 5.1. The LE flux peaks around 1.5 GeV to 3.5 GeV but after that it falls off rapidly. In contrast, the ME flux is almost flat from 2 - 6 GeV and after that it falls off but at a much slower rate compared to the LE flux and it remains substantially higher than the LE flux even beyond 6 GeV. At $\sim$ 2.5 GeV, the ME flux is $\sim 25 - 35\%$ smaller than the LE flux. Hence, in our analyses of probing the NSI parameters, we use a combination of LE and ME flux together, so as to extract information on new physics from both the lower energy ($1-3$ GeV) and the higher energy ($\gtrsim$ 4 GeV) regime as much as possible. We compare the results with those obtained using the LE beam only for the same total runtime of the experiment. The beamline parameters assumed for the different design fluxes used in our sensitivity calculations are given in Table 5.2.

Our analysis includes both appearance ($\nu_\mu \to \nu_e$) and disappearance ($\nu_\mu \to \nu_\mu$) channels, simulating both signal as well as background. The simulated background includes contamination of antineutrinos (neutrinos) in the neutrino (antineutrino) mode, and also misinterpretation of flavors, as discussed in detail in [77]. To analyze the NSI scenario, we utilise the GLoBES extension called **snu.c** which is described in [70, 155].

To calculate the sensitivity with which the NSI parameters can be probed, one can define the (statistical) χ^2 as follows [2]:

$$\chi^2(\mathbf{n}^{\text{true}}, \mathbf{n}^{\text{test}}) = 2 \sum_{i}^{N_{reco}} \sum_{j} (n_{i,j}^{\text{true}} ln \frac{n_{i,j}^{\text{true}}}{n_{i,j}^{\text{test}}(f)} + n_{i,j}^{\text{test}}(f) - n_{i,j}^{\text{true}}). \tag{5.2.1}$$

where **n** represents event rate vectors in N_{reco} bins of reconstructed energy. Here, the SI case is treated as *true* while the NSI parameters are allowed to vary in the *test* data set. The sum over the number of channels (j) runs over the $\nu_\mu \to \nu_e$ and $\nu_\mu \to \nu_\mu$ channels and the corresponding antineutrino channels, $\bar{\nu}_\mu \to \bar{\nu}_e$ and $\bar{\nu}_\mu \to \bar{\nu}_\mu$. The index i indicates the sum over all the energy bins ranging from $E = 0 - 20$ GeV. We have a total of 71 bins of non-uniform widths (64 bins with uniform bin width of 125 MeV in the energy range $E = 0 - 8$ GeV and 7 bins with variable width beyond 8 GeV) [77]. The detector configuration, efficiencies, resolutions and systematic uncertainties for DUNE are listed in Table. 5.3.

Detector details	Normalisation error		Energy calibration error	
	Signal	Background	Signal	Background
DUNE Runtime (yr) = 3.5 ν + 3.5 $\bar{\nu}$ 40 kton, LArTPC	ν_e : 5% ν_μ : 5%	ν_e : 10% ν_μ : 10%	ν_e : 2% ν_μ : 5%	ν_e : 10% ν_μ : 10%

Table 5.3: Detector configuration, efficiencies, resolutions and systematic uncertainties for DUNE.

[2]The definition of the χ^2 in Eq. 5.2.1 includes only statistical effects for the purpose of understanding. The systematic effects have of course been taken into account in our numerical results obtained using GLoBES.

We have used the standard oscillation parameters in Table 5.1, taken from Ref. [134, 135]. For the neutrino mass hierarchy, we assume a spectrum corresponding to normal hierarchy in the true dataset. Since DUNE has no sensitivity to the solar parameters and since θ_{13} is rather well measured by current reactor and long baseline experiments, we keep these values fixed to their current best-fit values, while marginalizing over θ_{23} (in the present 3σ range) and δ ($[-\pi, \pi]$), if not plotting them. In addition, we marginalize over the atmospheric mass-squared splitting, Δm^2_{31}, allowing for the two possible mass hierarchies. When studying a non-diagonal NSI parameter, $\varepsilon_{\alpha\beta}$, we also marginalize over its corresponding phase, $\varphi_{\alpha\beta}$ in the range $[-\pi, \pi]$. Therefore, if we study two non-diagonal complex parameters simultaneously, we marginalize over a total of five parameters.

In our analysis, we consider two diagonal NSI parameters and three off-diagonal NSI parameters with both their moduli and phases. If we also include the yet unknown CP phase, δ, we have a total of nine parameters. We depict $\Delta\chi^2$ correlations among these nine parameters ($\delta, \varepsilon_{ee}, |\varepsilon_{e\mu}|, \varphi_{e\mu}, |\varepsilon_{e\tau}|, \varphi_{e\tau}, |\varepsilon_{\mu\tau}|, \varphi_{\mu\tau}, \varepsilon_{\tau\tau}$) considering them pairwise at a time and the number of such combinations is 36.

5.3 A scan of parameter space at the level of probability

In order to obtain insight into the correlations and degeneracies among the various NSI and SI parameters that may impact the signals at DUNE, the first step is, naturally, to look at the relevant oscillation probabilities. We consider the following oscillation channels that are accessible[3] at DUNE :

1. Appearance channel : $\nu_\mu \to \nu_e$ ($\bar{\nu}_\mu \to \bar{\nu}_e$)

2. Disappearance channel : $\nu_\mu \to \nu_\mu$ ($\bar{\nu}_\mu \to \bar{\nu}_\mu$).

[3] $\nu_\mu \to \nu_\tau$ is also in principle there, but the signal is extremely tiny.

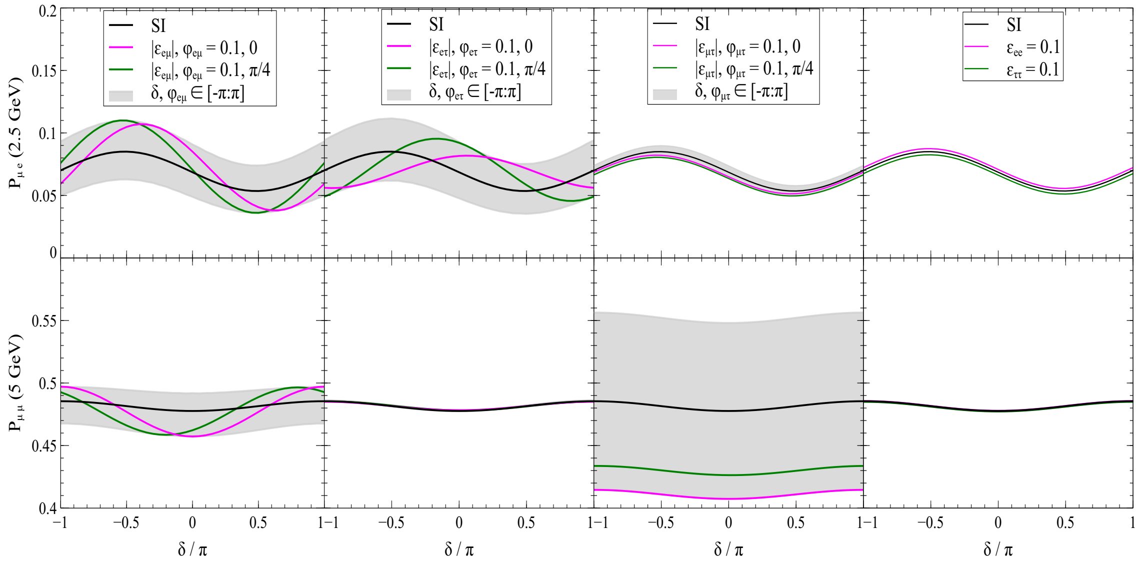

Figure 5.2: $P_{\mu e}$ (top row) and $P_{\mu\mu}$ (bottom row) at fixed baseline (L = 1300 km) and fixed energy values (E = 2.5 GeV for $P_{\mu e}$ and E = 5 GeV for $P_{\mu\mu}$) plotted as a function of the CP phase, δ. The strength of all NSI terms is taken to be the same (= 0.1).

In what follows, we consider the relevant parameters that include two of the diagonal NSI parameters ($\varepsilon_{ee}, \varepsilon_{\tau\tau}$) and the moduli and phases of the three off-diagonal NSI parameters ($\varepsilon_{e\mu}$,$\varepsilon_{e\tau}$,$\varepsilon_{\mu\tau}$). A detailed assessment of the role of individual NSI terms on the different oscillation channels has been carried out in [156,157]. Based on the analyses in [156,157], we can conclude that among all NSI parameters, $\varepsilon_{e\mu}$ and $\varepsilon_{e\tau}$ mainly impact the appearance channel ($\nu_\mu \to \nu_e$) while ε_{ee} has a milder impact. It is clear that $\varepsilon_{e\mu}$ enters $\nu_\mu \to \nu_e$ channel. The almost maximal mixing in the $2-3$ sector ensures that $\varepsilon_{e\tau}$ also impacts this channel with similar strength as $\varepsilon_{e\mu}$ (see section 5.5 and the discussion in Sec. IV of [156]). Similarly, the disappearance channel ($\nu_\mu \to \nu_\mu$) is more sensitive to the presence of NSI parameter $\varepsilon_{\mu\tau}$ (see section 5.6 and the discussion in Sec. IV of [156]).

In the following sub-sections, we perform a scan of the parameter space at the probability level. We first discuss the fixed energy and fixed baseline snapshots of probabilities (subection 5.3.1). We then discuss SI-NSI degeneracies in the context of DUNE as a function of energy keeping δ fixed at the best-fit value (subsection 5.3.2). Further, we go on to the discussion of SI-NSI degeneracies as a function of δ (keeping the energy fixed) in subection 5.3.3.

5.3.1 Snapshots of $P_{\mu e}$ and $P_{\mu\mu}$ at fixed energy and fixed baseline

In Fig. 5.2, we fix the baseline at 1300 km and show the impact of NSI parameters [4] on snapshots of $P_{\mu e}$ and $P_{\mu\mu}$ as a function of δ at certain (appropriately chosen) fixed energy values. This aids in identification of parameters that may have the largest impact at the level of probabilities, though at specific energy values. For the $\nu_\mu \to \nu_e$ channel (top row in Fig. 5.2), we choose the fixed value of energy to be $E = 2.5$ GeV. This value corresponds to the first oscillation maximum for $P_{\mu e}$. On the other hand, $P_{\mu\mu}$ is very close to zero at 2.5 GeV while it is substantial at higher values of energy. Hence we depict curves for $P_{\mu\mu}$ (bottom row in Fig. 5.2) at 5 GeV. The grey bands show the variation of the probability when the relevant phases $(\delta, \varphi_{\alpha\beta})$ are allowed to vary in the range $[-\pi, \pi]$. As a reference, the SI case is shown as a solid black line in all the plots.

As far as $P_{\mu e}$ at 2.5 GeV (top row) is concerned, we note that the effect of $\varepsilon_{e\mu}$ or $\varepsilon_{e\tau}$ is more pronounced when compared to the other NSI terms. The presence of $\varepsilon_{e\mu}$ or $\varepsilon_{e\tau}$ modifies the overall amplitude and the location of the peaks/dips of the probabilities while the presence of a nonzero $\phi_{e\mu}$ or $\phi_{e\tau}$ brings in additional phase shifts. We note that $\varepsilon_{\mu\tau}$ has a much smaller effect on $P_{\mu e}$. ε_{ee} and $\varepsilon_{\tau\tau}$ also have a miniscule effect on the amplitude of $P_{\mu e}$. On the other hand, $P_{\mu\mu}$ at 5 GeV (bottom row) gets affected most by the presence of the $\varepsilon_{\mu\tau}$ term. $\varepsilon_{e\tau}, \varepsilon_{ee}, \varepsilon_{\tau\tau}$ have practically no impact on $P_{\mu\mu}$. $\varepsilon_{e\mu}$ induces some phase dependence on $P_{\mu\mu}$.

In what follows, we generalise the above discussion and study the energy dependence of the SI-NSI degeneracies for $P_{\mu e}$ and $P_{\mu\mu}$ and also vary the NSI terms instead of keeping their values fixed.

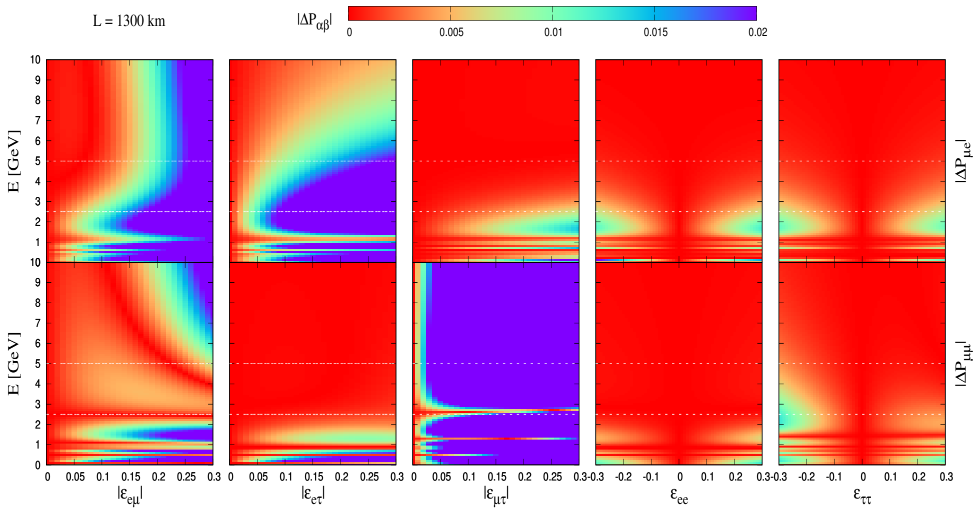

Figure 5.3: Heatmaps corresponding to $|\varDelta P_{\mu e}|$ (top row) and $|\varDelta P_{\mu\mu}|$ (bottom row) in the two-dimensional plane of individual NSI term ($\varepsilon_{\alpha\beta}$) and energy. The NSI phases are set to zero. The dashed white lines indicate the value of energy at 2.5 GeV and 5 GeV.

5.3.2 Energy dependence of the SI-NSI degeneracies

To quantify the impact of NSI terms, let us define a quantity, $|\varDelta P_{\alpha\beta}| = |P^{NSI}_{\alpha\beta} - P^{SI}_{\alpha\beta}|(\alpha, \beta = e, \mu)$, which is absolute value of probability difference between the SI and NSI scenarios.

Our results are given in Fig. 5.3 in the form of heatmaps as functions of energy and the strength of the NSI parameter for $|\varDelta P_{\mu e}|$ (top row) and $|\varDelta P_{\mu\mu}|$ (bottom row). The NSI phases are taken to be zero and the standard oscillation parameters have been pinned to their best-fit values (see Table 5.1). If we carefully examine the top row of Fig. 5.3, we note that $|\varDelta P_{\mu e}|$ is mostly affected by $|\varepsilon_{e\mu}|$ and $|\varepsilon_{e\tau}|$. Note that, the impact of $|\varepsilon_{e\mu}|$ or $|\varepsilon_{e\tau}|$ is most prominent around $2-3$ GeV. One can derive a useful conclusion here regarding difference in impact of $|\varepsilon_{e\mu}|$ and $|\varepsilon_{e\tau}|$ on $|\varDelta P_{\mu e}|$. As we go beyond ~ 4 GeV, $|\varepsilon_{e\tau}|$ gradually makes $|\varDelta P_{\mu e}|$ smaller (red region), while $|\varepsilon_{e\mu}|$ makes $|\varDelta P_{\mu e}|$ stay at a high value (blue region) which is almost independent of energy. This, in turn, suggests that one may be able to probe $\varepsilon_{e\mu}$ more effectively than $\varepsilon_{e\tau}$ by use of higher energy beam tune. The other NSI terms $\varepsilon_{\mu\tau}, \varepsilon_{ee}$ or $\varepsilon_{\tau\tau}$ do not induce much change, keeping $|\varDelta P_{\mu e}| \lesssim 0.005$ for most of

[4]The moduli of all the NSI parameters have been chosen to be equal to 0.1 (allowed by present constraints [144, 158]). For reasons of clarity and simplicity, we take one NSI parameter non-zero at a time.

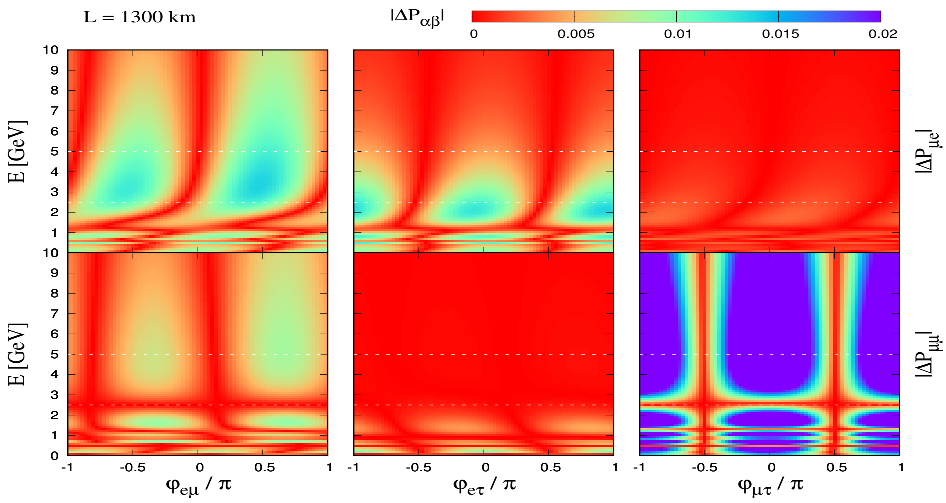

Figure 5.4: Heatmaps for $|\Delta P_{\mu e}|$ (top row) and $|\Delta P_{\mu\mu}|$ (bottom row) are shown as the function of a NSI phase $\varphi_{\alpha\beta}$ (taken one at a time) as the energy is changed, keeping the baseline fixed at 1300 km. The associated NSI amplitudes ($\varepsilon_{\alpha\beta}$) were kept fixed at 0.05. The two horizontal dashed white lines correspond to the energies 2.5 GeV and 5 GeVs.

the energy range.

From the bottom row of Fig. 5.3 corresponding to $|\Delta P_{\mu\mu}|$, we note that $\varepsilon_{\mu\tau}$ plays an important role. $|\Delta P_{\mu\mu}|$ is large (blue) in most of the energy range as long as $|\varepsilon_{\mu\tau}| \gtrsim 0.02$. This is to be contrasted with other NSI terms, as even a small value of $\varepsilon_{\mu\tau}$ can induce a large impact on $|\Delta P_{\mu\mu}|$. As can be noted, a higher energy beam may be able to probe $\varepsilon_{\mu\tau}$ via this channel effectively. If we look at the impact of $|\varepsilon_{e\mu}|$ and $|\varepsilon_{e\tau}|$, we note that $|\varepsilon_{e\mu}|$ gradually makes $|\Delta P_{\mu\mu}|$ larger at $E \gtrsim 5$ GeV (indicated by blue region on the top right side of the panel) while $|\varepsilon_{e\tau}|$ does not seem to impact $|\Delta P_{\mu\mu}|$. Thus, for the disappearance channel as well, it appears that the higher energy beam may prove more useful in probing $\varepsilon_{e\mu}$ than $\varepsilon_{e\tau}$. For an analytic understanding of the energy dependence of $\Delta P_{\alpha\beta}$ in the presence of NSI, see section 5.5 and 5.6.

We next consider the case of nonzero phases $\varphi_{\alpha\beta}$. In Fig. 5.4, heatmaps corresponding to $|\Delta P_{\mu e}|$ (top row) and $|\Delta P_{\mu\mu}|$ (bottom row) in the two-dimensional plane of individual NSI phase ($\varphi_{\alpha\beta}$) and energy are shown. The moduli of NSI terms ($|\varepsilon_{e\mu}|, |\varepsilon_{e\tau}|$ or $|\varepsilon_{\mu\tau}|$) were kept fixed at 0.05. From Fig. 5.4, we note that $|\Delta P_{\mu e}|$ (top row) is most affected by $\phi_{e\mu}$

or $\phi_{e\tau}$ while $\phi_{\mu\tau}$ has almost no effect. Around $2-4$ GeV, $\phi_{e\mu}$ and $\phi_{e\tau}$ produce similar qualitative features indicating SI-NSI degeneracy (red band) occurring at a pair of values given by $\phi_{e\mu} \approx 0, \pm\pi$ and $\phi_{e\tau} \approx -0.6\pi, 0.4\pi$. At energies beyond 4 GeV, $|\varDelta P_{\mu e}|$ is very small ($\sim$ 0) almost uniformly in the presence of $\phi_{e\tau}$ while in the presence of $\phi_{e\mu}$, it still exhibits a relatively high value ($0.005-0.01$) in large region of the parameter space. For a quantitative understanding of this feature, we refer the reader to section 5.5.

For $|\varDelta P_{\mu\mu}|$, Fig. 5.4 (bottom row) shows that it is affected most significantly by $\phi_{\mu\tau}$, showing sharp SI-NSI degeneracy around $\phi_{\mu\tau} \approx \pm\pi/2$. This arises because of the fact that $|\varDelta P_{\mu\mu}| \propto \cos\phi_{\mu\tau}$ (See Eq. 5.6.3 in section 5.6). We also note that $|\varDelta P_{\mu\mu}|$ remains close to zero in the presence of $\phi_{e\tau}$ and shows moderate variation for in the presence of $\phi_{e\mu}$.

Finally, we would like to mention that the qualitative features of Fig. 5.4 remain unchanged even if the moduli of the relevant off-diagonal NSI terms ($|\varepsilon_{e\mu}|$, $|\varepsilon_{e\tau}|$ or $|\varepsilon_{\mu\tau}|$) are increased.

5.3.3 δ-dependence of SI-NSI degeneracies

In Figs. 5.5 and 5.6 we depict the heatmaps for $|\varDelta P_{\mu e}|$ and $|\varDelta P_{\mu\mu}|$ in the $\delta - \varepsilon_{\alpha\beta}$ plane. In these plots, the first (second) row corresponds to a fixed energy of 2.5 (5) GeV. We can derive the following conclusions in connection with $P_{\mu e}$ (see also section 5.5) :

- In the case of $\nu_\mu \to \nu_e$ channel (Fig. 5.5), the NSI terms $\varepsilon_{e\mu}$ and $\varepsilon_{e\tau}$ have relatively larger impact than the other NSI parameters. For $\varepsilon_{e\mu}$ and $\varepsilon_{e\tau}$, the degenerate regions ($|\varDelta P_{\mu e}| \lesssim 0.05$) are narrowly concentrated around a pair of values of δ (see Table 5.4 below) These sharp SI-NSI degenerate regions exist even for 5 GeV but at somewhat different values of δ. For $\varepsilon_{e\tau}$, the degenerate region seems to be larger at 5 GeV in contrast to 2.5 GeV. This is not seen in the case of $\varepsilon_{e\mu}$ (this observation is consistent with Fig. 5.3). Note that the locations of SI-NSI degenerate regions is roughly independent of the size of $|\varepsilon_{e\mu}|$ and $|\varepsilon_{e\tau}|$. For $|\varepsilon_{\mu\tau}|$, the degenerate region is

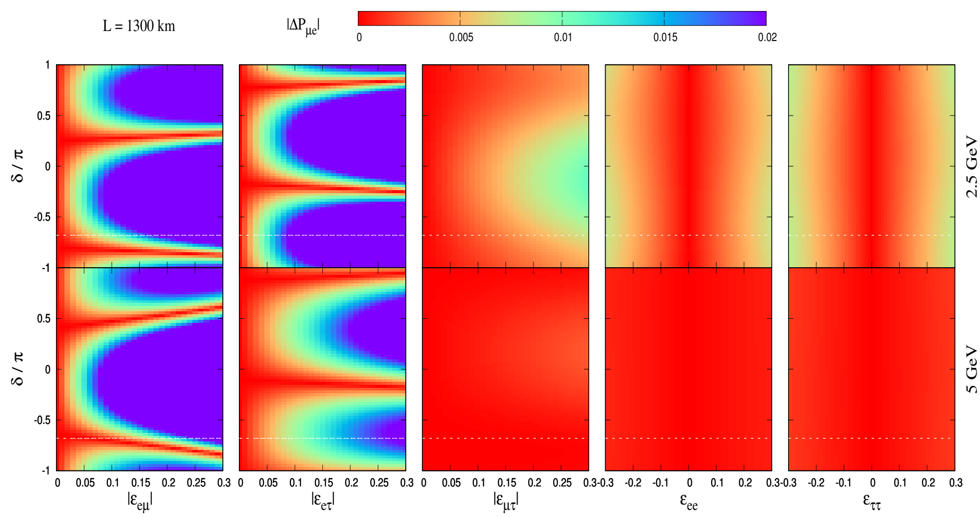

Figure 5.5: Heatmaps for $|\Delta P_{\mu e}|$ are shown for a fixed baseline of 1300 km in the parameter space of $\delta - \varepsilon_{\alpha\beta}$ for two fixed energies: 2.5 GeV (top row) and 5 GeV (bottom). A single NSI parameter was considered at a time and the associated NSI phases were taken to be zero. The dashed horizontal white line corresponds to the bestfit value of the Dirac CP phase δ ($\approx -0.68\pi$) taken from Table 5.1.

E	$\Delta P_{\mu e}(\lvert\varepsilon_{e\mu}\rvert) \approx 0$	$\Delta P_{\mu e}(\lvert\varepsilon_{e\tau}\rvert) \approx 0$
2.5 GeV	$0.25\pi, -0.8\pi$	$0.8\pi, -0.2\pi$
5 GeV	$0.4\pi, -0.6\pi$	$0.95\pi, -0.15\pi$

Table 5.4: The values of δ where $|\Delta P_{\mu e}|$ almost vanishes in the presence of $\varepsilon_{e\mu}$ or $\varepsilon_{e\tau}$ (red spikes) in Fig. 5.5.

broader and shows a soft feature of peaking at $\delta \approx \pm\pi$ for 2.5 GeV. For ε_{ee} and $\varepsilon_{\tau\tau}$, the degenerate regions have similar structure showing no CP phase dependence.

- For the $\nu_\mu \to \nu_\mu$ channel (Fig. 5.6), as mentioned earlier, it is more appropriate to look at 5 GeV (the bottom row). As expected, $\varepsilon_{\mu\tau}$ has the largest impact and its effect is independent of the CP phase, δ (see also section 5.6). The impact of $\varepsilon_{e\mu}$ is also important with two sharp peaks occurring around $\delta \approx \pm\pi/2$. The other terms such as $\varepsilon_{e\tau}, \varepsilon_{ee}, \varepsilon_{\tau\tau}$ have almost no effect at 5 GeV (here also the results are consistent with Fig. 5.3).

To complete the discussion, we now discuss the effect of non-zero phases. We keep the moduli of the respective NSI terms fixed at $|\varepsilon_{\alpha\beta}| = 0.05$ and plot heatmaps corresponding

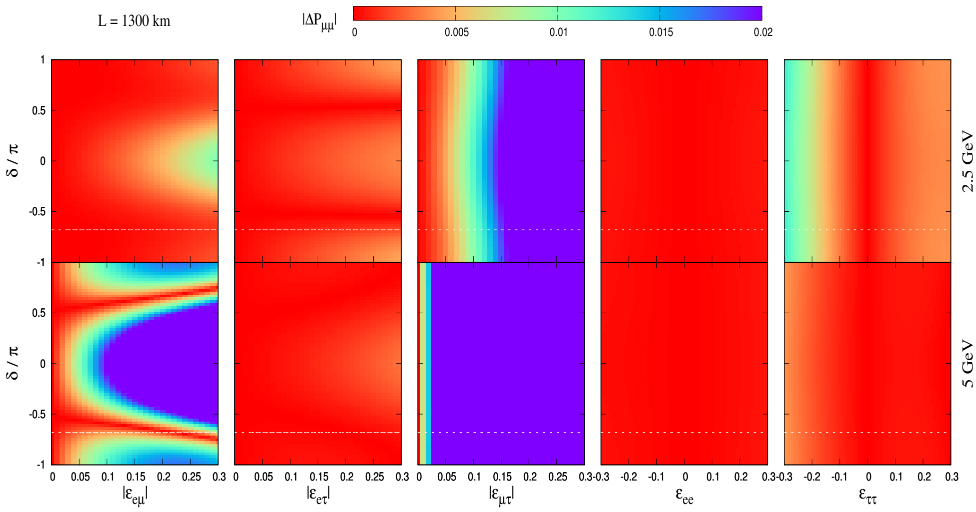

Figure 5.6: Similar to Fig. 5.5 but for the $\nu_\mu \to \nu_\mu$ channel.

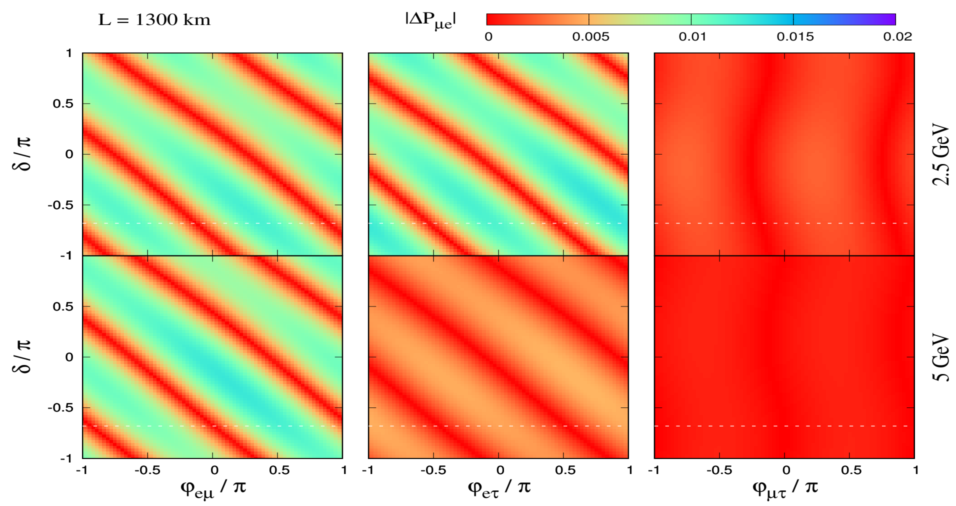

Figure 5.7: Heatmaps for $|\varDelta P_{\mu e}|$ are shown for a fixed baseline of 1300 km in the parameter space of $\delta - \varphi_{\alpha\beta}$ for two values of energies, 2.5 GeV (top row) and 5 GeV (bottom row). Note that $|\varepsilon_{\alpha\beta}|$ was fixed to 0.05. The dashed horizontal white line corresponds to the bestfit value of the Dirac CP phase δ ($\approx -0.68\pi$) taken from Table 5.1.

to $|\varDelta P_{\mu e}|$ and $|\varDelta P_{\mu\mu}|$ in the $\varphi_{\alpha\beta} - \delta$ plane in Fig. 5.7 and Fig. 5.8 respectively. As before, we show our results for two different values energy, 2.5 GeV (top row) and 5 GeV (bottom row). We make the following observations from these plots:

- In the case of the $\nu_\mu \to \nu_e$ channel (Fig. 5.7), we see degenerate regions in the case of $\varphi_{e\mu}$ and $\varphi_{e\tau}$ (where $|\varDelta P_{\mu e}| \lesssim 0.005$) slanted at an angle of 135^o. In the case of $\varphi_{\mu\tau}$,

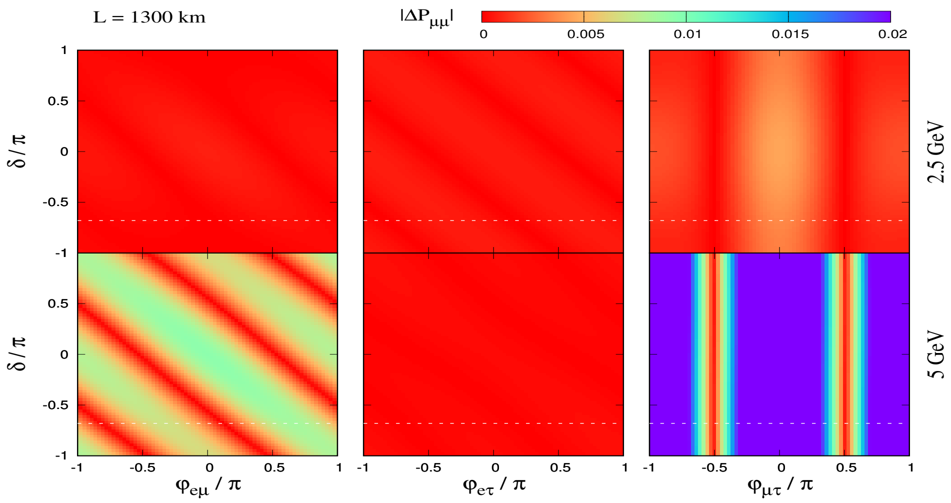

Figure 5.8: Similar to Fig. 5.7 but for the $\nu_\mu \to \nu_\mu$ channel.

$|\varDelta P_{\mu e}|$ remains close to zero and stays within $\lesssim 0.005$ in the entire $\varphi_{\mu\tau} - \delta$ space [5]. For 5 GeV, the pattern remains very similar for $\phi_{e\mu}$, but the extent of degeneracy increases for $\phi_{e\tau}$, as expected from our previous analyses.

From the analytic expressions given in section 5.5 (Eq. 5.5.1 and 5.5.2), we can note that the SI-NSI degeneracy in the presence of $\phi_{e\mu}$ or $\phi_{e\tau}$ for a fixed non-zero moduli of the corresponding NSI term, arises from the following:

$$\sin(\delta + \phi_{e\mu} - \gamma_1^{e\mu}) \approx 0 \text{ (for } \phi_{e\mu}) \quad \text{and} \quad \sin(\delta + \phi_{e\tau} + \gamma_1^{e\tau}) \approx 0 \text{ (for } \phi_{e\tau})$$
$$\implies \delta + \phi_{e\mu} \approx n\pi + \gamma_1^{e\mu} \quad \text{and} \quad \delta + \phi_{e\tau} \approx n\pi - \gamma_1^{e\tau}\text{ , with } n = 0, \pm 1, \pm 2, \ldots \tag{5.3.1}$$

Here $\gamma_1^{e\mu} = \tan^{-1}(\frac{\tan^2\theta_{23}}{\varDelta} + \cot\varDelta)$ and $\gamma_1^{e\tau} = \tan^{-1}(\frac{1}{\varDelta} - \cot\varDelta)$. We note that Eqns. 5.3.1 show equations of straight lines with a slope of 135^o and equal intercepts on the δ and $\varphi_{\alpha\beta}$ axes [6]. Furthermore, the various intercepts (corresponding to different n) on the $\varphi_{\alpha\beta}$ or δ axes are separated by π which is also seen in Fig. 5.7.

[5]In general, $\varepsilon_{\mu\tau}$ has milder impact on the $P_{\mu e}$. The effect of the associated NSI phase $\phi_{\mu\tau}$ is, thus, small. If we take somewhat larger value of $|\varepsilon_{\mu\tau}|$, $|\varDelta P_{\mu e}|$ would increase slightly but the qualitative feature of $|\varDelta P_{\mu e}(\phi_{\mu\tau})|$ would still remain similar.

[6]$x/a + y/b = 1$ is a general equation of straight line with intercepts a and b on the x and y axes respectively.

- In case of the $\nu_\mu \to \nu_\mu$ channel (Fig. 5.8), we focus on the bottom row. Here $\phi_{e\mu}$ shows the SI-NSI degenerate regions roughly mimicking straight lines at 135^o slope, whereas $\phi_{e\tau}$ shows no effect. $\phi_{\mu\tau}$ manifests itself by rendering $|\Delta P_{\mu\mu}|$ to a much larger value ($\gtrsim$ 0.02) for most of the parameter space, but there exist two sharp degenerate regions occurring at $\phi_{\mu\tau} \approx \pm\pi/2$ with no δ dependence.

5.4 Probing the NSI parameter space at the level of χ^2

In the present section, we numerically explore the NSI parameter space at the level of χ^2 using the standard LE as well as ME beam tunes. Our main results are summarized in Fig. 5.9 where we depict contours at a confidence level (c.f.) of 99%. The solid cyan (black hatched) contours correspond to LE (LE + ME) beams. More specifically, the regions enclosed by these contours depict the regions where there is SI-NSI degeneracy for those pair of parameters. Below, we discuss some noteworthy features as can be observed from Fig. 5.9:

1. Let us first consider the panels with $\varepsilon_{e\mu}$ (either $|\varepsilon_{e\mu}|$ or $\phi_{e\mu}$ or both) which are shown in light yellow colour. We note that use of different beam tunes (ME in conjunction with the LE beam) offers visible improvement of results (shrinking of contours) in these pairs of parameters. This is one of the key results of the present article. In order to explain the observed pattern, let us recollect from Figs. 5.3 and 5.4 that the presence of $|\varepsilon_{e\mu}|$ or $\phi_{e\mu}$ leads to large difference between SI and NSI scenarios even at larger values of energies *i.e.*, $E \gtrsim 4$ GeV. Thus, with the LE+ME option we are able to place tighter constraints on the parameter space corresponding to parameters $|\varepsilon_{e\mu}|$ and $\phi_{e\mu}$.

   From Eq. 5.2.1, the $\Delta\chi^2$ in the presence of two NSI parameters, say, a and b, can be

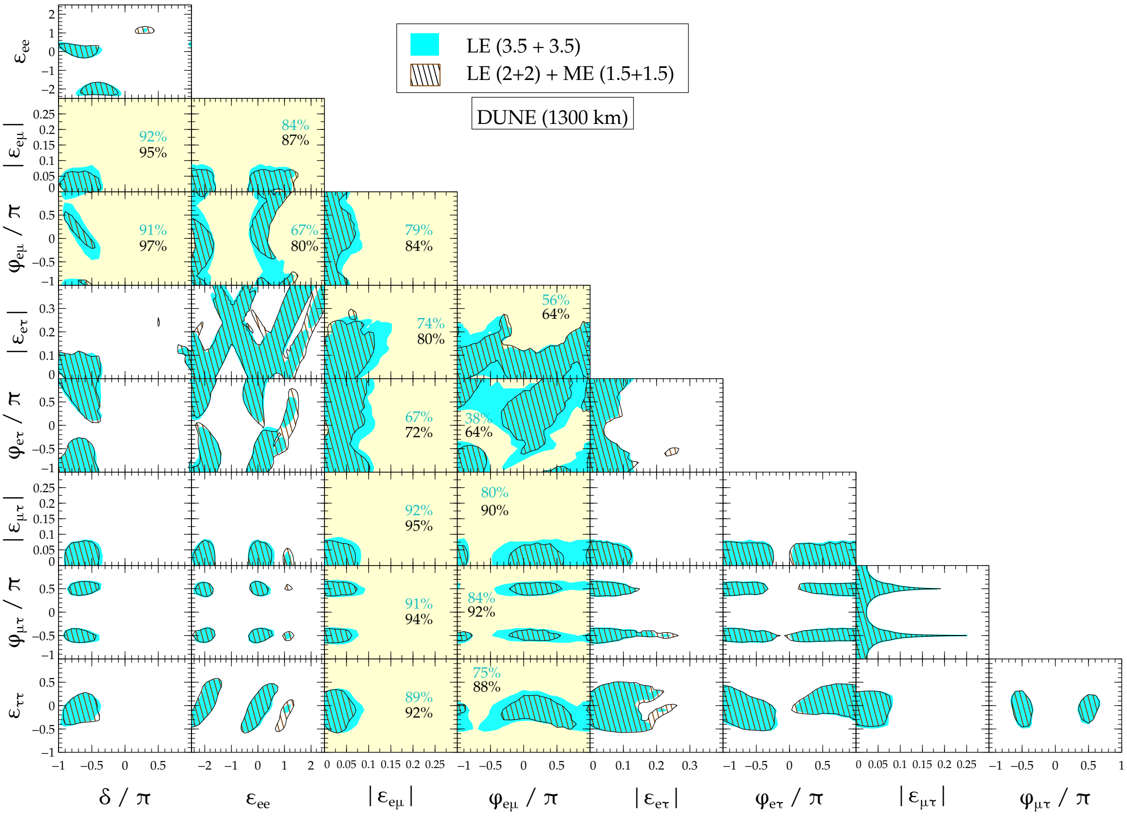

Figure 5.9: A comparison of the sensitivity of DUNE to probe the NSI parameters at 99% confidence level when a standard low energy (LE) beam tune is used (cyan region) and when a combination of low and medium energy (LE + ME) beam tune is used (black hatched region), keeping the total runtime same (3.5 years of ν + 3.5 years of $\bar{\nu}$ run) for both scenarios. In the latter case, the total runtime is distributed between the LE beam (2 years of ν + 2 years of $\bar{\nu}$) and the medium energy beam (1.5 years of ν + 1.5 years of $\bar{\nu}$). The panels with a light yellow (white) background indicate significant improvement (no improvement) by using LE + ME beam over using LE only. The numbers in the light yellow shaded panels correspond to the area lying outside the contour for the two cases (cyan for LE and black for LE+ME) expressed as a percentage of the total parameter space plotted. These numbers quantify the improvement over the LE only option when the ME beam tune is used in conjunction with the LE beam tune in these panels.

written as [7]:

$$
\begin{aligned}
\Delta\chi^2(a,b) &\sim \Delta\chi^2_{\mu e}(a,b) + \Delta\chi^2_{\mu\mu}(a,b) \\
&\sim \text{Min} \sum_{\text{energy}} \Big[|\Delta P_{\mu e}(a)| + |\Delta P_{\mu e}(b)| + |\Delta P_{\mu\mu}(a)| + |\Delta P_{\mu\mu}(b)| \Big]. \qquad (5.4.1)
\end{aligned}
$$

[7]For the ease of understanding, we write neutrino contribution only. The dependence on flux and cross-section has been omitted for clarity in understanding the dependence on probabilities.

For *e.g.*, if we focus on the $|\varepsilon_{e\mu}|$-$|\varepsilon_{e\tau}|$ plane, we have

$$\varDelta\chi^2(|\varepsilon_{e\mu}|,|\varepsilon_{e\tau}|) \sim \text{Min} \sum_{\text{energy}} \Big[|\varDelta P_{\mu e}(|\varepsilon_{e\mu}|)| + |\varDelta P_{\mu e}(|\varepsilon_{e\tau}|)| + |\varDelta P_{\mu\mu}(|\varepsilon_{e\mu}|)| + |\varDelta P_{\mu\mu}(|\varepsilon_{e\tau}|)| \Big], \tag{5.4.2}$$

where the sum is over all the energy bins ($0-20$ GeV) and the minimization is performed over $\delta, \theta_{23}, \varDelta m^2_{31}, \phi_{e\mu}, \phi_{e\tau}$. From the probability level discussion (Fig. 5.3), we can assess the impact of the NSI terms $|\varepsilon_{e\mu}|$ and $|\varepsilon_{e\tau}|$ on $P_{\mu e}$ and $P_{\mu\mu}$. In the case of $|\varDelta P_{\mu e}|$, at low values of energy, the impact of the two NSI parameters is quite similar. But, at higher energies, the effects due to $|\varepsilon_{e\mu}|$ tend to be larger than effects due to $|\varepsilon_{e\tau}|$. This means that ME beam is expected to alter the degenerate region more in the case of $|\varepsilon_{e\mu}|$ and less in the case of $|\varepsilon_{e\tau}|$. That the smaller contribution from the disappearance channel is in the same direction as the larger contribution from the appearance channel (with $|\varepsilon_{e\mu}|$ and $|\varepsilon_{e\tau}|$ acting in opposite directions) can also be seen from the plot.

2. We next consider the remaining panels in which we see that there is very little or no improvement of results after using the ME beam along with the LE beam. If we look at the pair of parameters, $|\varepsilon_{e\tau}| - \varepsilon_{ee}, \phi_{e\tau} - \varepsilon_{ee}, \varepsilon_{\tau\tau} - \varepsilon_{ee}, \phi_{e\tau} - |\varepsilon_{e\tau}|$ and $\varepsilon_{\tau\tau} - |\varepsilon_{e\tau}|$ in particular, we note that the degenerate regions get enlarged slightly. This is because of the fact that the the presence of $\varepsilon_{e\tau}$, unlike $\varepsilon_{e\mu}$, actually adds to the SI-NSI degeneracy at higher energies (see Figs. 5.3 and 5.4 and the discussions in Sec. 5.3.2).

3. For the panels with $|\varepsilon_{\mu\tau}|$ and $\phi_{\mu\tau}$ as one of the parameters, there is very marginal improvement (except when $|\varepsilon_{e\mu}|$ or $\phi_{e\mu}$ is present) in the degenerate contours using the LE+ME beam. To see how the $\varDelta\chi^2$ arises in panels showing the parameter space associated with $|\varepsilon_{\mu\tau}|$, let us take for example, the pair of parameters, $|\varepsilon_{\mu\tau}|$ and $|\varepsilon_{e\tau}|$

and express the $\varDelta\chi^2$ (Eq. 5.4.1) as

$$\varDelta\chi^2(|\varepsilon_{\mu\tau}|, |\varepsilon_{e\tau}|) \sim \text{Min} \sum_{\text{energy}} \Big[|\varDelta P_{\mu e}(|\varepsilon_{\mu\tau}|)| + |\varDelta P_{\mu e}(|\varepsilon_{e\tau}|)| + |\varDelta P_{\mu\mu}(|\varepsilon_{\mu\tau}|)| + |\varDelta P_{\mu\mu}(|\varepsilon_{e\tau}|)| \Big], \tag{5.4.3}$$

where the sum is over all the energy bins (0 – 20 GeV) and the minimization is carried over $\delta, \theta_{23}, \varDelta m^2_{31}, \phi_{\mu\tau}, \phi_{e\tau}$. Now, from Eq. 5.6.3, we know that in leading order, $|\varDelta P_{\mu\mu}(\varepsilon_{\mu\tau})|$ is independent of δ and is directly proportional to $\cos\phi_{\mu\tau}$. Minimization over $\phi_{\mu\tau} \in [-\pi, \pi]$ will always then find the constant, energy-independent value of $\phi_{\mu\tau} \approx \pm\pi/2$ which makes the $\varDelta\chi^2$ contribution due to $P_{\mu\mu}$ vanishingly small[8]. Thus, even when $|\varepsilon_{\mu\tau}|$ is present, the $\varDelta\chi^2$ receives a dominant contribution from the $\nu_\mu \to \nu_e$ channel. This is more clear from the panels showing the parameter space associated to $\phi_{\mu\tau}$ (*i.e.*, where $\phi_{\mu\tau}$ is not marginalised). The magnitude of $\varDelta\chi^2$ in such panels is dominantly contributed by the $\nu_\mu \to \nu_\mu$ channel for all values of $\phi_{\mu\tau} \not\approx \pm\pi/2$. But around $\phi_{\mu\tau} \approx \pm\pi/2$, the contribution from the $\nu_\mu \to \nu_\mu$ becomes very small and the $\nu_\mu \to \nu_e$ channel dominates, as we have also verified numerically. This explains the appearance of degenerate contours at $\phi_{\mu\tau} \approx \pm\pi/2$ as well.

4. All the parameter spaces showing ε_{ee} (entire 2nd column and the top panel of the 1st column) have an additional degeneracy around $\varepsilon_{ee} \approx -2$, in addition to the true solution at $\varepsilon_{ee} \approx 0$. This extra solution comes due to the marginalisation over the opposite mass hierarchy. Similar degeneracy has also been observed in previous studies: in [159–161] (in the context of NSI) and also in [162] in the context of Lorentz violating parameters.

[8] On the other hand this does not happen for $\varepsilon_{e\mu}$ and $\varepsilon_{e\tau}$ for the following reason. Eqns. 5.5.1 and 5.5.2 tell us that in leading order, $|\varDelta P_{\mu e}(\varepsilon_{e\mu})| \propto \sin(\delta + \phi_{e\mu} - \gamma_1^{e\mu})$ and $|\varDelta P_{\mu e}(\varepsilon_{e\tau})| \propto \sin(\delta + \phi_{e\tau} + \gamma_1^{e\tau})$ where $\gamma_1^{e\mu}$ and $\gamma_1^{e\tau}$ are energy-dependent quantities. Thus, unlike in the case of $|\varDelta P_{\mu\mu}(\varepsilon_{\mu\tau})|$, there does not exist a unique energy-independent phase value which would make its contribution to $\varDelta\chi^2$ to ~ 0.

5.5 Analytic understanding of the behaviour of $\varDelta P_{\mu e}$

Here we look at the expressions for probability difference between SI and NSI and make an attempt in understanding how the individual NSI parameters affect the SI-NSI degeneracy. We calculate these expressions by making use of the probability expressions from [156] upto first order in $\varepsilon_{\alpha\beta}$'s. Using the expressions for $P_{\mu e}$ in presence of a single NSI parameter ($|\varepsilon_{e\mu}|$, $|\varepsilon_{e\tau}|$ or ε_{ee}) we arrive at the following three equations:

$$
\begin{aligned}
&\varDelta P_{\mu e}(\varepsilon_{e\mu}) = P_{\mu e}^{NSI}(\varepsilon_{e\mu}) - P_{\mu e}^{SI} \\
&\underbrace{\approx -4A\varDelta \sin\varDelta |\varepsilon_{e\mu}| s_{13} s_{2(23)} c_{23} D_1^{e\mu} \sin(\delta + \phi_{e\mu} - \gamma_1^{e\mu})}_{\mathrm{I}} + \underbrace{2A\varDelta \sin\varDelta |\varepsilon_{e\mu}| \alpha s_{2(12)} s_{2(23)} s_{23} D_2^{e\mu} \sin(\phi_{e\mu} + \gamma_2^{e\mu})}_{\mathrm{II}} \\
&+ O(\varepsilon_{e\mu}^2) \\
&\approx 2A\varDelta \sin\varDelta |\varepsilon_{e\mu}| s_{2(23)} \Big[- 2 s_{13} c_{23} D_1^{e\mu} \sin(\delta + \phi_{e\mu} - \gamma_1^{e\mu}) + \alpha s_{2(12)} s_{23} D_2^{e\mu} \sin(\phi_{e\mu} + \gamma_2^{e\mu}) \Big],
\end{aligned}
\tag{5.5.1}
$$

&

$$
\begin{aligned}
&\varDelta P_{\mu e}(\varepsilon_{e\tau}) = P_{\mu e}^{NSI}(\varepsilon_{e\tau}) - P_{\mu e}^{SI} \\
&\underbrace{\approx 4A\varDelta \sin\varDelta |\varepsilon_{e\tau}| s_{13} s_{2(23)} s_{23} D_1^{e\tau} \sin(\delta + \phi_{e\tau} + \gamma_1^{e\tau})}_{\mathrm{I}} + \underbrace{(- 2A\varDelta \sin\varDelta |\varepsilon_{e\tau}| \alpha s_{2(12)} s_{2(23)} c_{23} D_2^{e\tau} \sin(\gamma_2^{e\tau} - \phi_{e\tau}))}_{\mathrm{II}} \\
&+ O(\varepsilon_{e\tau}^2) \\
&\approx 2A\varDelta \sin\varDelta |\varepsilon_{e\tau}| s_{2(23)} \Big[2 s_{13} s_{23} D_1^{e\tau} \sin(\delta + \phi_{e\tau} + \gamma_1^{e\tau}) - \alpha s_{2(12)} c_{23} D_2^{e\tau} \sin(\gamma_2^{e\tau} - \phi_{e\tau}) \Big],
\end{aligned}
\tag{5.5.2}
$$

where,

$$
\begin{aligned}
D_1^{e\mu} &= [\sin^2\varDelta + (\tan^2\theta_{23} \frac{\sin\varDelta}{\varDelta} + \cos\varDelta)^2]^{1/2} & \gamma_1^{e\mu} &= \tan^{-1}(\frac{\tan^2\theta_{23}}{\varDelta} + \cot\varDelta) \\
D_2^{e\mu} &= [\sin^2\varDelta + (\cot^2\theta_{23} \frac{\varDelta}{\sin\varDelta} + \cos\varDelta)^2]^{1/2} & \gamma_2^{e\mu} &= \tan^{-1}(\frac{\cot^2\theta_{23}\varDelta}{\sin^2\varDelta} + \cot\varDelta) \\
D_1^{e\tau} &= [\sin^2\varDelta + (\frac{\sin\varDelta}{\varDelta} - \cos\varDelta)^2]^{1/2}; & \gamma_1^{e\tau} &= \tan^{-1}(\frac{1}{\varDelta} - \cot\varDelta)
\end{aligned}
$$

$$D_2^{e\tau} = [\sin^2\varDelta + (\frac{\varDelta}{\sin\varDelta} - \cos\varDelta)^2]^{1/2} \qquad\qquad \gamma_2^{e\tau} = \tan^{-1}(\frac{\varDelta}{\sin^2\varDelta} - \cot\varDelta).$$

Here $A = a/\varDelta m^2_{31} = 2\sqrt{2}EG_F n_e/\varDelta m^2_{31}$. By making the substitution $A \to A(1+\varepsilon_{ee})$ [163] we also have,

$$\begin{aligned}
\varDelta P_{\mu e}(\varepsilon_{ee}) &= P^{NSI}_{\mu e}(\varepsilon_{ee}) - P^{SI}_{\mu e} \\
&\approx \underbrace{s^2_{2(13)}s^2_{23}\Big[\frac{\sin^2[\{1-A(1+\varepsilon_{ee})\}\varDelta]}{\{1-A(1+\varepsilon_{ee})\}^2} - \frac{\sin^2\{(1-A)\varDelta\}}{(1-A)^2}\Big]}_{\mathrm{I}} \\
&+ \underbrace{\Big\{\alpha^2 s^2_{2(12)}c^2_{23}\Big[\frac{\sin^2\{A(1+\varepsilon_{ee})\varDelta\}}{\{A(1+\varepsilon_{ee})\}^2} - \frac{\sin^2(A\varDelta)}{A^2}\Big] + \alpha s_{2(13)}s_{2(12)}s_{2(23)}\Big[\frac{\sin[\{1-A(1+\varepsilon_{ee})\}\varDelta]}{1-A(1+\varepsilon_{ee})}.\frac{\sin\{A(1+\varepsilon_{ee})\varDelta\}}{A(1+\varepsilon_{ee})} - \frac{\sin\{(1-A)\varDelta\}}{1-A}.\frac{\sin(A\varDelta)}{A}\Big]\cos(\delta+\varDelta)\Big\}}_{\mathrm{II}},
\end{aligned} \tag{5.5.3}$$

where $\varDelta = \dfrac{\varDelta m^2_{31}L}{4E}$.

When $\varDelta P_{\mu e}$ becomes close to zero, it becomes difficult to separate NSI from SI and we have a SI-NSI degeneracy. We plot the terms in Eq. 5.5.1, Eq. 5.5.2 and Eq. 5.5.3 as functions of δ for an energy of 2.5 GeV and also at a higher energy of 5 GeV in Fig. 5.10 with fixed values of the NSI amplitude and zero NSI phase as indicated in the figure. For $\varepsilon_{e\mu}$ or $\varepsilon_{e\tau}$, the second term (blue) is very small (scaled down by the additional factor $\alpha \sim 10^{-2}$ compared to the first term) and also independent of the CP phase δ. It is the first term (green) which mainly dictates the behaviour of $\varDelta P_{\mu e}$ in presence of $\varepsilon_{e\mu}$ or $\varepsilon_{e\tau}$. We note the locations (see Table 5.5) where the overall value of $\varDelta P_{\mu e}$ (red) becomes zero in Fig. 5.10. These locations are indeed consistent with the locations of the *red spikes* in Fig. 5.5 as listed in Table 5.4. The origin of these special values of δ can easily be understood as follows.

On a closer inspection of the first term in Eq. 5.5.1 and Eq. 5.5.2, we observe that it is proportional to $D_1^{e\mu}$ for $\varepsilon_{e\mu}$ and to $D_1^{e\tau}$ for $\varepsilon_{e\tau}$. From Fig. 5.11 (left panel), we observe that around 2.5 GeV both $D_1^{e\mu}$ and $D_1^{e\tau}$ have similar magnitude [9]. But as the energy increases further $D_1^{e\mu}$ keeps on increasing while $D_1^{e\tau}$ decreases. This indicates that at higher energies, $|\Delta P_{\mu e}(|\varepsilon_{e\mu}|)|$ increases while $|\Delta P_{\mu e}(|\varepsilon_{e\tau}|)|$ becomes smaller. This explains why the degeneracy increases for higher energy in presence of $\varepsilon_{e\tau}$ compared to $\varepsilon_{e\mu}$ in the ν_e appearance channel, as observed from our simulation earlier(see Fig. 5.3).

On a related note, let us also try to understand the role of $\varphi_{\alpha\beta}$ in Fig. 5.4 with variation in energy. In Fig. 5.11 (right panel) we show the variation of the phase arguments $\gamma_1^{e\mu}$ and $\gamma_1^{e\tau}$ (appearing in the first terms of Eq. 5.5.1 and Eq. 5.5.2) with energy. Around 2.5 GeV, $\gamma_1^{e\mu} \approx \gamma_1^{e\tau}$. At higher energies, $\gamma_1^{e\mu} > \gamma_1^{e\tau}$, but both remains positive. Both of them tends to get plateaued at $E \gtrsim 4$ GeV or so, with $\gamma_1^{e\mu}/\pi \sim 0.3$ and $\gamma_1^{e\tau}/\pi \sim 0.1$ on an average to a crude approximation. Since $|\Delta P_{\mu e}(\varepsilon_{e\mu})| \propto \sin(\delta + \phi_{e\mu} - \gamma_1^{e\mu})$ approximately, we can guess that with a given b.f. value of $\delta \approx -0.7\pi$ we will have a degeneracy around $\phi_{e\mu}/\pi \approx 0, \pm\pi$ at energies $\gtrsim 4$ GeV. Similarly, since $|\Delta P_{\mu e}(\varepsilon_{e\tau})| \propto \sin(\delta + \phi_{e\tau} + \gamma_1^{e\tau})$ approximately, we will have a degeneracy around $\phi_{e\mu}/\pi \approx 0.6, -0.4$ at energies $\gtrsim 4$ GeV. A look at Fig. 5.4 (top row: first and second columns) indeed shows that the heatmaps for $|\Delta P_{\mu e}|$ looks similar around 2.5 GeV and at energies $\gtrsim 4$ GeV, the degenerate regions (red bands) become independent of energy and are located at the $\phi_{e\mu}$ (or $\phi_{e\tau}$) values just predicted above.

E	$\Delta P_{\mu e}(\lvert\varepsilon_{e\mu}\rvert) \approx 0$	$\Delta P_{\mu e}(\lvert\varepsilon_{e\tau}\rvert) \approx 0$
2.5 GeV	$0.22\pi, -0.82\pi$	$0.76\pi, -0.16\pi$
5 GeV	$0.4\pi, -0.63\pi$	$0.92\pi, -0.1\pi$

Table 5.5: The values of δ (obtained from Fig. 5.10) where $\Delta P_{\mu e}(|\varepsilon_{e\mu}|)$ and $\Delta P_{\mu e}(|\varepsilon_{e\tau}|)$ (the red curves in Fig. 5.10) becomes zero, giving rise to SI-NSI degeneracy.

[9]Recall that the b.f. value of θ_{23} in our analysis is not maximal, rather 47.7^o. Even then the octant does not appear to play a significant role despite the presence of the extra $\tan^2\theta_{23}$ factor in the definition of $D_1^{e\mu}$.

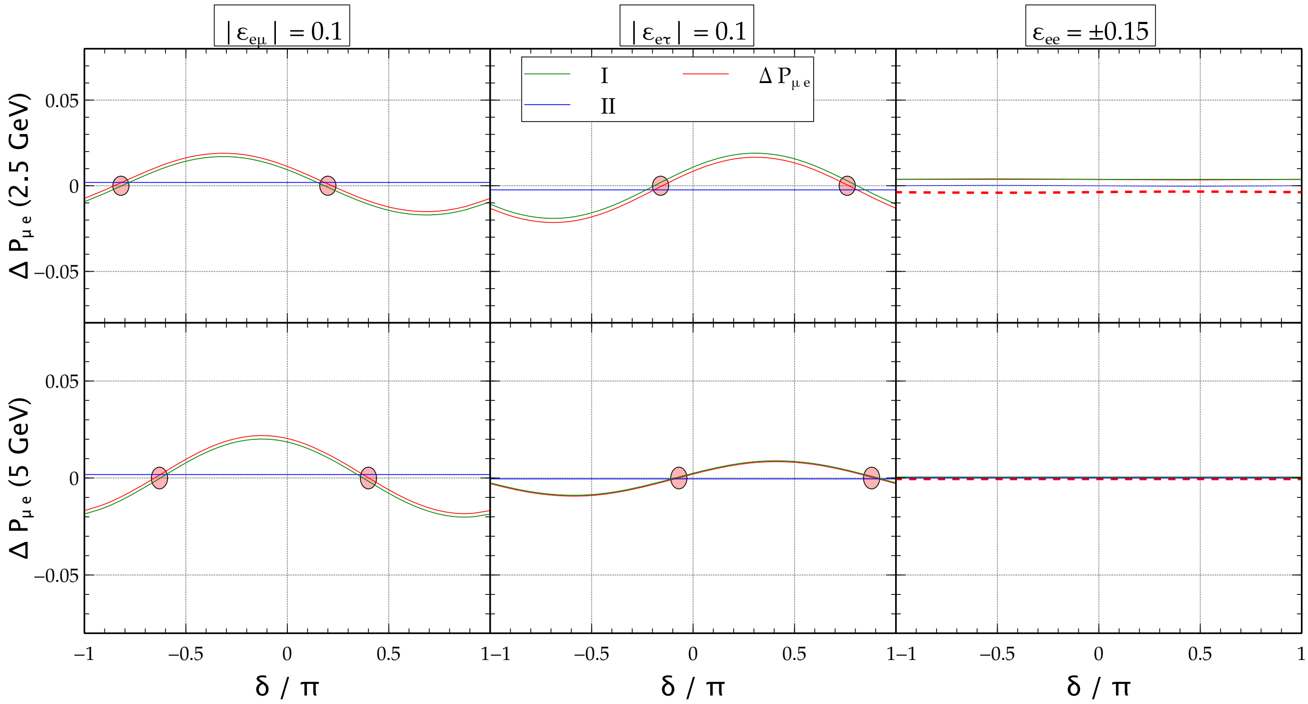

Figure 5.10: The terms (denoted by green, blue and cyan curves) in the RHS of Eq. 5.5.1 (first column), 5.5.2 (second column) and 5.5.3 (third column) are plotted as functions of δ for two fixed energies 2.5 GeV (top row) and 5 GeV (bottom row). The overall $\varDelta P_{\mu e}$ is represented by the red curve and the small red circles denote where it becomes zero.

5.6 Probability analysis for $P_{\mu\mu}$

Proceeding along similar lines as section 5.5, we derive the expressions for $P^{NSI}_{\mu\mu} - P^{SI}_{\mu\mu}$.

$$
\begin{aligned}
\varDelta P_{\mu\mu}(|\varepsilon_{e\mu}|) &= P^{NSI}_{\mu\mu}(|\varepsilon_{e\mu}|) - P^{SI}_{\mu\mu} \\
&\approx \underbrace{-4s^3_{23}\frac{A}{1-A}|\varepsilon_{e\mu}|\Big[As_{23}|\varepsilon_{e\mu}| + 2s_{13}\cos\delta\Big]X}_{\mathrm{I}} \\
&\underbrace{+\quad 4s_{2(23)}\frac{Y}{A(1-A)}\Big[\alpha s_{13}s_{2(12)}\cos\delta - (\alpha s_{2(12)} + Ac_{23}|\varepsilon_{e\mu}|)D(|\varepsilon_{e\mu}|)\cos(\delta - \theta(|\varepsilon_{e\mu}|))\Big]}_{\mathrm{II}}
\end{aligned}
\tag{5.6.1}
$$

$$
\varDelta P_{\mu\mu}(|\varepsilon_{e\tau}|) = P^{NSI}_{\mu\mu}(|\varepsilon_{e\tau}|) - P^{SI}_{\mu\mu}
$$

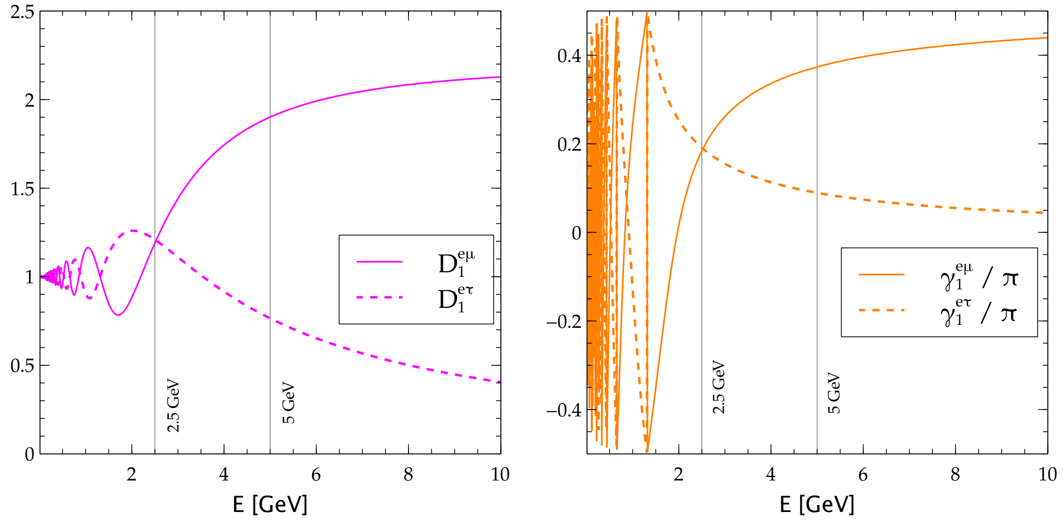

Figure 5.11: $D_1^{e\mu}$ and $D_1^{e\tau}$ are plotted as functions of energy (left panel). $\gamma_1^{e\mu}$ and $\gamma_1^{e\tau}$ are plotted as functions of energy in the right panel. The standard oscillation parameters are at their b.f value (Table 5.1).

$$
\begin{aligned}
&\approx \underbrace{-4s_{23}^2 c_{23}\frac{A}{1-A}|\varepsilon_{e\tau}|\Big[Ac_{23}|\varepsilon_{e\tau}| + 2s_{13}\cos\delta\Big]X}_{\mathrm{I}} \\
&\underbrace{+ \quad 4s_{2(23)}\frac{Y}{A(1-A)}\Big[\alpha s_{13}s_{2(12)}\cos\delta - (\alpha s_{2(12)} - As_{23}|\varepsilon_{e\tau}|)D(|\varepsilon_{e\tau}|)\cos(\delta-\theta(|\varepsilon_{e\tau}|))\Big]}_{\mathrm{II}}
\end{aligned}
\tag{5.6.2}
$$

where,

$$X = c_{23}^2 \varDelta \sin 2\varDelta + \frac{\sin^2(1-A)\varDelta}{(1-A)} - 2c_{23}^2 \cos A\varDelta \sin\varDelta \frac{\sin(1-A)\varDelta}{(1-A)}$$

$$Y = c_{23}^2 \sin^2 A\varDelta + s_{23}^2 \sin^2(1-A)\varDelta - s_{23}^2 \sin^2\varDelta - c_{2(23)}A\sin^2\varDelta$$

$$D(|\varepsilon_{e\mu}|) = \left\{s_{13}^2 + A^2 s_{23}^2|\varepsilon_{e\mu}|^2 + 2As_{13}s_{23}|\varepsilon_{e\mu}|\cos\delta\right\}^{1/2} \quad ; \quad \theta(|\varepsilon_{e\mu}|) = \arctan\frac{As_{23}|\varepsilon_{e\mu}|\sin\delta}{s_{13} + As_{23}|\varepsilon_{e\mu}|\cos\delta}$$

$$D(|\varepsilon_{e\tau}|) = \left\{s_{13}^2 + A^2 c_{23}^2|\varepsilon_{e\tau}|^2 + 2As_{13}c_{23}|\varepsilon_{e\tau}|\cos\delta\right\}^{1/2} \quad ; \quad \theta(|\varepsilon_{e\tau}|) = \arctan\frac{Ac_{23}|\varepsilon_{e\tau}|\sin\delta}{s_{13} + Ac_{23}|\varepsilon_{e\tau}|\cos\delta}.$$

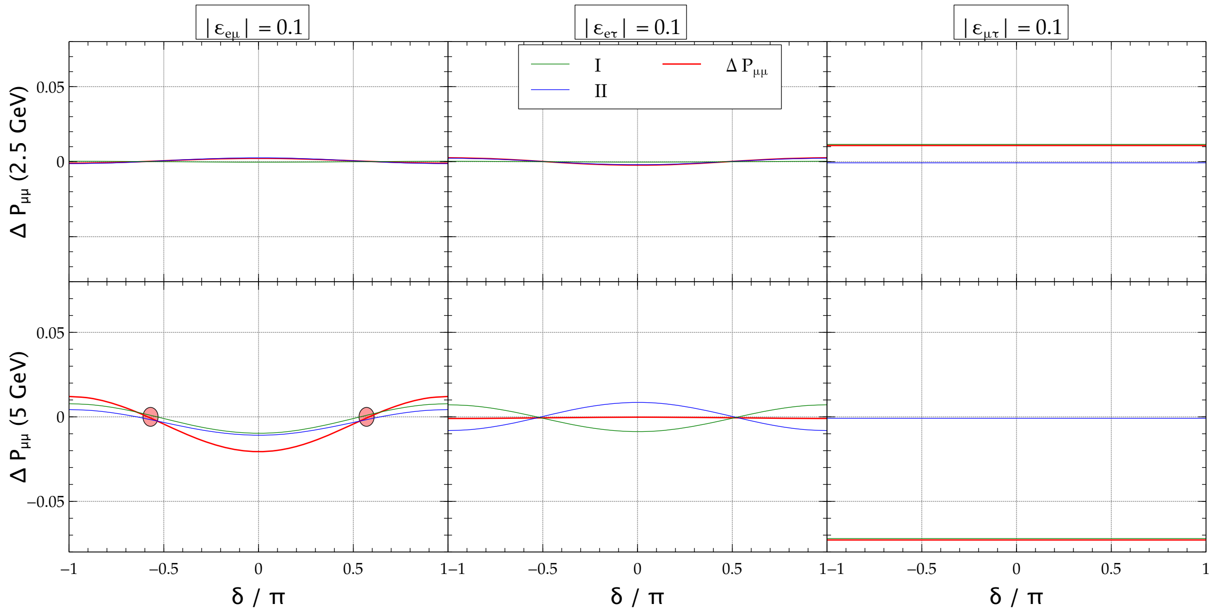

Figure 5.12: The terms (denoted by green, blue and cyan curves) in the RHS of Eq. 5.6.1 (first column), 5.6.2 (second column) and 5.6.3 (third column) are plotted as functions of δ for two fixed energies 2.5 GeV (top row) and 5 GeV (bottom row). The overall $\varDelta P_{\mu\mu}$ (sum of the three terms) is represented by the red curve and the small red circles denote where it becomes zero.

$$\varDelta P_{\mu\mu}(\varepsilon_{\mu\tau}) \approx \underbrace{(-2|\varepsilon_{\mu\tau}|A\varDelta s^3_{2(23)} \sin 2\varDelta \cos\phi_{\mu\tau})}_{\mathrm{I}} + \underbrace{(-4A|\varepsilon_{\mu\tau}|c^2_{2(23)} s_{2(23)} \sin^2\varDelta \cos\phi_{\mu\tau})}_{\mathrm{II}}$$
$$\approx -4|\varepsilon_{\mu\tau}|A s_{2(23)} \sin\varDelta \cos\phi_{\mu\tau}[\varDelta s^2_{2(23)} \cos\varDelta + c^2_{2(23)} \sin\varDelta]. \tag{5.6.3}$$

In Fig. 5.12, we plot the terms of Eq. 5.6.1, 5.6.2 and 5.6.3 for two fixed energies 2.5 GeV and 5 GeV as functions of δ. We have already observed before that for the disappearance channel, it is the higher energy range that contributes more. To understand $\varDelta P_{\mu\mu}$, we will thus refer to the more relevant bottom row of Fig. 5.12. It is clear from the figure (first and second column) that the two terms for $\varDelta P_{\mu\mu}$ act in the same direction for $\varepsilon_{e\mu}$ (thereby increasing the overall $|\varDelta P_{\mu\mu}|$), but show opposite behaviour for $\varepsilon_{e\tau}$, leading to an overall very small $\varDelta P_{\mu\mu}$ through cancellation in the latter case. Looking back at Eqns. 5.6.1 and 5.6.2, we note that both term I and II are roughly proportional to $\cos\delta$. But due to the presence of a relative sign in the coefficient of $A|\varepsilon_{e\tau}|$ in the second term, this behaves in almost opposite direction of the first. [10] This has an interesting consequence that $\Delta P_{\mu\mu}(\varepsilon_{e\tau})$ is significantly small at higher energies unlike $\Delta P_{\mu\mu}(\varepsilon_{e\mu})$. This is also manifestly evident from our simulation (Fig. 5.3: bottom row, first and second columns). Additionally, in Fig. 5.6 (bottom row, first and second column) we have also observed the appearance of two red peaks around $\pm\pi/2$ for $\varepsilon_{e\mu}$ and mostly reddish region (implying very small $\Delta P_{\mu\mu}$) in presence of $\varepsilon_{e\tau}$.

Finally, we see from Eq. 5.6.3 and the corresponding third column of Fig. 5.12 that $\Delta P_{\mu\mu}(\varepsilon_{\mu\tau})$ is independent of the CP phase δ and its value is quite significant (except around 2.5 GeV) compared to that in presence of $\varepsilon_{e\mu}$ or $\varepsilon_{e\tau}$. This corroborates the observations in Fig. 5.3 (bottom row, third column) and Fig. 5.6 (third column).

5.7 SI-NSI difference at the level of event rates in the context of DUNE

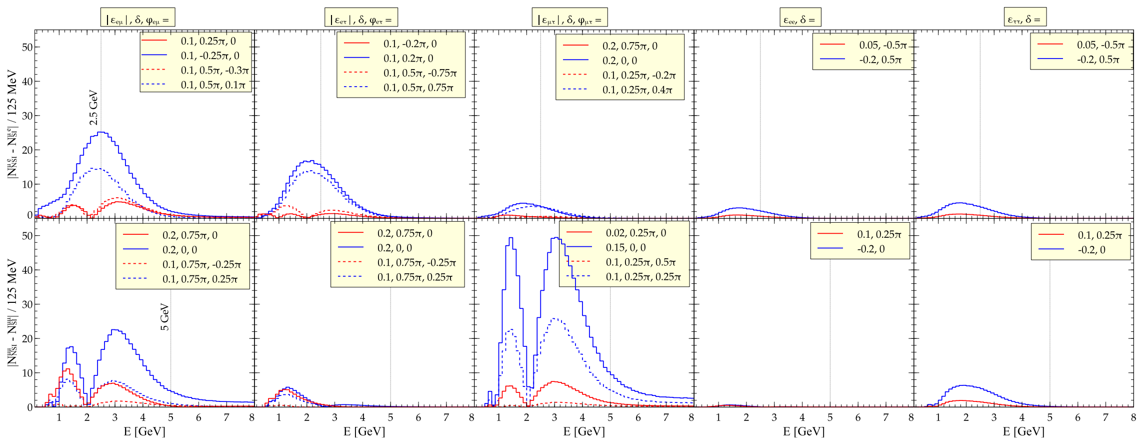

Figure 5.13: SI-NSI difference at the level of event rates for $\nu_\mu \to \nu_e$ channel (top row) and $\nu_\mu \to \nu_\mu$ channel (bottom row) and for different NSI parameters. The LE flux has been used.

In order to illustrate the SI-NSI degeneracy at the level of event rates, we can define the

---

[10] $s_{13} \sim 0.15, \qquad A s_{23}|\varepsilon_{e\mu}| \sim A c_{23}|\varepsilon_{e\tau}| \sim 0.03, \qquad D(|\varepsilon_{e\mu}|) \sim D(|\varepsilon_{e\tau}|) \lesssim 0.15$
$\alpha s_{13} s_{2(12)} \sim 0.004, \qquad \alpha s_{2(12)} \sim 0.027, \qquad \theta(|\varepsilon_{e\mu}|) \sim \theta(|\varepsilon_{e\tau}|) \lesssim 10^{o}$
Thus in the first term of the Eq. 5.6.1 and Eq. 5.6.2, $\cos\delta$ part is dominating and in the second term, $\theta(\varepsilon_{\alpha\beta})$ is very small,- making the overall $\Delta P_{\mu\mu}$ approximately proportional to $\cos\delta$ for ease of understanding.

following quantity

$$\Delta N_{\alpha\beta}(E) = N^{\rm NSI}_{\alpha\beta}(E) - N^{\rm SI}_{\alpha\beta}(E) \tag{5.7.1}$$

where $N_{\alpha\beta}$ stands for the number of events for $\nu_\alpha \to \nu_\beta$. The results are shown in Fig. 5.13. The top row depicts the event difference in case of $\nu_\mu \to \nu_e$ channel and the bottom row shows the event difference in case of $\nu_\mu \to \nu_\mu$ channel. We have picked four choices of the parameters as indicated in the figure. These choices are guided by our observations in Sec. 5.3. The red curves correspond to the almost degenerate case while blue curves correspond to regions away from degeneracy. The vertical grey line is showing the location of 2.5 GeV (5 GeV) in the top panel (bottom panel). If we use a given beam tune (say, the standard LE beam tune), the characteristic shape of the event difference spectrum is similar to the original event spectrum in case of no degeneracy (see the blue solid and dashed curves). When we choose the parameters corresponding to degenerate solutions, the spectrum shape of the event difference is completely altered (see the red curves). In the latter case, one can note that the SI-NSI degeneracy manifests itself in the form of a dip near the energy value of 2.5 GeV at which first oscillation maximum occurs for $\nu_\mu \to \nu_e$ channel.

Some of the crucial features that can be seen from Fig. 5.13 are :

- $\varepsilon_{e\mu}$ and $\varepsilon_{e\tau}$ have the largest impact in case of $\nu_\mu \to \nu_e$ channel (top row of Fig. 5.13).
- $\varepsilon_{\mu\tau}$ has the largest impact in case of $\nu_\mu \to \nu_\mu$ channel (bottom row of Fig. 5.13).

Bibliography

[1] C. Quigg, *Gauge Theories of the Strong, Weak, and Electromagnetic Interactions* (Princeton University Press, USA, 2013), ISBN 9780691135489, 9781400848225, URL http://chrisquigg.com/gauge-theories/.

[2] B. Pontecorvo, Sov. Phys. JETP **26**, 984 (1968), [Zh. Eksp. Teor. Fiz.53,1717(1967)].

[3] Z. Maki, M. Nakagawa, and S. Sakata, Progress of Theoretical Physics **28**(5), 870 (1962).

[4] W. Pauli, Cambridge Monogr.Part.Phys.Nucl.Phys.Cosmol.,14,1 (2000).

[5] E. Fermi, Z. Phys. **88**, 161 (1934).

[6] E. Fermi, Nuovo Cim. **11**, 1 (1934), [,535(1934)].

[7] F. Reines, C. L. Cowan, F. B. Harrison, A. D. McGuire, and H. W. Kruse, Phys. Rev. **117**, 159 (1960).

[8] B. Pontecorvo, J.Exptl. Theoret. Phys. **33** (1957) 549 [Sov. Phys. JETP **6** (1958) 429] .

[9] B. Pontecorvo, J.Exptl. Theoret. Phys. **34** (1958) 247 [Sov. Phys. JETP **7** (1958) 172] .

[10] B. Pontecorvo, J. Exptl. Theoret. Phys. **53** (1967) 1717. [Sov. Phys. JETP **26** (1968) 984] .

[11] R. Davis, D. S. Harmer, and K. C. Hoffman, Phys. Rev. Lett. **20**, 1205 (1968), URL https://link.aps.org/doi/10.1103/PhysRevLett.20.1205.

[12] R. J. Davis and J. C. Evans, Jr, Report on the Brookhaven solar neutrino experiment URL https://www.osti.gov/biblio/7330079.

[13] J. N. Bahcall, W. A. Fowler, I. Iben, and R. L. Sears, Astrophys. J., 137,344, 1963 .

[14] S. M. Bilenky and B. Pontecorvo, Comments on Nuclear and Particle-Physics,7(1977) 149 .

[15] S. Eliezer and A. R. Swift, Nucl. Phys., B105, 45, 1976 .

[16] S. M. Bilenky and B. Pontecorvo, Sov. J. Nucl. Phys., 24, 316-319, 1976 .

[17] L. Wolfenstein, Phys. Rev. **D17**, 2369 (1978).

[18] S. P. Mikheev and A. Y. Smirnov, Sov. Phys. Usp. **30**, 759 (1987).

[19] A. Loureiro, A. Cuceu, F. B. Abdalla, B. Moraes, L. Whiteway, M. McLeod, S. T. Balan, O. Lahav, A. Benoit-Lévy, M. Manera, R. P. Rollins, and H. S. Xavier, Phys. Rev. Lett. **123**, 081301 (2019), URL https://link.aps.org/doi/10.1103/PhysRevLett.123.081301.

[20] P. Minkowski, Phys. Lett. **B67**, 421 (1977).

[21] R. N. Mohapatra and G. Senjanovic, Phys. Rev. Lett. **44**, 912 (1980).

[22] T. Yanagida, Conf. Proc. **C7902131**, 95 (1979).

[23] M. Gell-Mann, P. Ramond, and R. Slansky, Conf. Proc. **C790927**, 315 (1979), 1306.4669.

[24] W. Konetschny and W. Kummer, Phys. Lett. **B70**, 433 (1977).

[25] T. P. Cheng and L.-F. Li, Phys. Rev. **D22**, 2860 (1980).

[26] G. Lazarides, Q. Shafi, and C. Wetterich, Nucl. Phys. **B181**, 287 (1981).

[27] J. Schechter and J. W. F. Valle, Phys. Rev. **D22**, 2227 (1980).

[28] R. N. Mohapatra and G. Senjanovic, Phys. Rev. **D23**, 165 (1981).

[29] R. Foot, H. Lew, X. G. He, and G. C. Joshi, Z. Phys. **C44**, 441 (1989).

[30] S. M. Barr, Phys. Rev. Lett. **92**, 101601 (2004), hep-ph/0309152.

[31] R. N. Mohapatra and J. W. F. Valle, Phys. Rev. D **34**, 1642 (1986), URL https://link.aps.org/doi/10.1103/PhysRevD.34.1642.

[32] M. Gonzalez-Garcia and J. Valle, Physics Letters B **216**(3), 360 (1989), ISSN 0370-2693, URL http://www.sciencedirect.com/science/article/pii/0370269389911313.

[33] Z.-z. Xing, Phys. Lett. **B530**, 159 (2002), hep-ph/0201151.

[34] B. R. Desai, D. P. Roy, and A. R. Vaucher, Mod. Phys. Lett. **A18**, 1355 (2003), hep-ph/0209035.

[35] W. Grimus and L. Lavoura, J. Phys. **G31**, 693 (2005), hep-ph/0412283.

[36] C. S. Lam, Phys. Lett. **B507**, 214 (2001), hep-ph/0104116.

[37] W. Grimus and L. Lavoura, JHEP **07**, 045 (2001), hep-ph/0105212.

[38] E. Ma, Phys. Rev. **D66**, 117301 (2002), hep-ph/0207352.

[39] A. Zee, Phys. Lett. **B93**, 389 (1980), [Erratum: Phys. Lett.B95,461(1980)].

[40] K. R. Dienes, E. Dudas, and T. Gherghetta, Nucl. Phys. **B557**, 25 (1999), hep-ph/9811428.

[41] N. Arkani-Hamed, S. Dimopoulos, G. R. Dvali, and J. March-Russell, Phys. Rev. **D65**, 024032 (2002), hep-ph/9811448.

[42] R. N. Mohapatra, S. Nandi, and A. Perez-Lorenzana, Phys. Lett. **B466**, 115 (1999), hep-ph/9907520.

[43] Y. Grossman and M. Neubert, Phys. Lett. **B474**, 361 (2000), hep-ph/9912408.

[44] I. Esteban, M. C. Gonzalez-Garcia, A. Hernandez-Cabezudo, M. Maltoni, and T. Schwetz, JHEP **01**, 106 (2019), 1811.05487.

[45] Y. Fukuda *et al.* (Super-Kamiokande), Phys. Rev. Lett. **81**, 1562 (1998), hep-ex/9807003.

[46] K. Abe *et al.* (T2K), Phys. Rev. Lett. **107**, 041801 (2011), 1106.2822.

[47] K. Abe *et al.* (T2K), Phys. Rev. **D91**(7), 072010 (2015), 1502.01550.

[48] F. P. An, J. Z. Bai, A. B. Balantekin, H. R. Band, D. Beavis, W. Beriguete, M. Bishai, S. Blyth, K. Boddy, R. L. Brown, B. Cai, G. F. Cao, *et al.*, Phys. Rev. Lett. **108**, 171803 (2012), URL https://link.aps.org/doi/10.1103/PhysRevLett.108.171803.

[49] A. Aguilar-Arevalo *et al.* (LSND), Phys. Rev. **D64**, 112007 (2001), hep-ex/0104049.

[50] A. A. Aguilar-Arevalo *et al.* (MiniBooNE), Phys. Rev. Lett. **121**(22), 221801 (2018), 1805.12028.

[51] M. A. Acero, C. Giunti, and M. Laveder, Phys. Rev. **D78**, 073009 (2008), 0711.4222.

[52] C. Giunti and M. Laveder, Phys. Rev. **C83**, 065504 (2011), 1006.3244.

[53] G. Mention, M. Fechner, T. Lasserre, T. A. Mueller, D. Lhuillier, M. Cribier, and A. Letourneau, Phys. Rev. **D83**, 073006 (2011), 1101.2755.

[54] M. Dentler, A. Hernández-Cabezudo, J. Kopp, P. A. N. Machado, M. Maltoni, I. Martinez-Soler, and T. Schwetz, JHEP **08**, 010 (2018), 1803.10661.

[55] S. Gariazzo, C. Giunti, M. Laveder, and Y. F. Li, JHEP **06**, 135 (2017), 1703.00860.

[56] A. M. Knee, D. Contreras, and D. Scott, JCAP **1907**, 039 (2019), 1812.02102.

[57] R. Adhikari, S. K. Agarwalla, and A. Raychaudhuri, Phys. Lett. **B642**, 111 (2006), hep-ph/0608034.

[58] M. Malinsky, T. Ohlsson, and H. Zhang, Phys. Rev. **D79**, 011301 (2009), 0811.3346.

[59] T. Ohlsson, Rept. Prog. Phys. **76**, 044201 (2013), 1209.2710.

[60] I. Girardi and D. Meloni, Phys. Rev. **D90**(7), 073011 (2014), 1403.5507.

[61] E. Fernandez-Martinez, J. Hernandez-Garcia, and J. Lopez-Pavon, JHEP **08**, 033 (2016), 1605.08774.

[62] D. V. Forero, S. Morisi, M. Tortola, and J. W. F. Valle, JHEP **09**, 142 (2011), 1107.6009.

[63] F. J. Escrihuela, D. V. Forero, O. G. Miranda, M. Tortola, and J. W. F. Valle, Phys. Rev. **D92**(5), 053009 (2015), [Erratum: Phys. Rev.D93,no.11,119905(2016)], 1503.08879.

[64] J. Cao *et al.* (2017), 1704.08181.

[65] A. Sousa, *talk at WIN2017*, URL https://indico.fnal.gov/contributionDisplay.py?contribId=101&confId=9942.

[66] W. Winter, *talk at WIN2017*, URL https://indico.fnal.gov/contributionDisplay.py?contribId=76&confId=9942.

[67] P. Huber, M. Lindner, and W. Winter, Comput.Phys.Commun. **167**, 195 (2005), hep-ph/0407333.

[68] P. Huber, J. Kopp, M. Lindner, M. Rolinec, and W. Winter, Comput. Phys. Commun. **177**, 432 (2007), hep-ph/0701187.

[69] J. Kopp, Sterile neutrinos and non-standard neutrino interactions in GLoBES, November 2010. https://www.mpi-hd.mpg.de/personalhomes/globes/tools/snu-1.0.pdf (2010).

[70] J. Kopp, M. Lindner, T. Ota, and J. Sato, Phys. Rev. **D77**, 013007 (2008), 0708.0152.

[71] R. Acciarri *et al.* (DUNE) (2015), 1512.06148.

[72] L. Camilleri, AIP Conference Proceedings **1680**, 020004 (2015), URL http://scitation.aip.org/content/aip/proceeding/aipcp/10.1063/1.4931863.

[73] M. Antonello *et al.* (LAr1-ND, ICARUS-WA104, MicroBooNE) (2015), 1503.01520.

[74] A. A. Aguilar-Arevalo *et al.* (MiniBooNE), Phys. Rev. Lett. **102**, 101802 (2009), 0812.2243.

[75] T. A. Mueller *et al.*, Phys. Rev. **C83**, 054615 (2011), 1101.2663.

[76] A. A. Aguilar-Arevalo *et al.* (MiniBooNE), Phys. Rev. Lett. **110**, 161801 (2013), 1303.2588.

[77] T. Alion *et al.* (DUNE) (2016), 1606.09550.

[78] C. Adams *et al.* (LBNE), in *LBNE* (2013), 1307.7335, URL http://www.osti.gov/scitech/biblio/1128102.

[79] V. De Romeri, E. Fernandez-Martinez, and M. Sorel, JHEP **09**, 030 (2016), 1607.00293.

[80] Michel Sorel, Private Correspondence (2017).

[81] T. J. Carroll, in *52nd Rencontres de Moriond on EW Interactions and Unified Theories (Moriond EW 2017) La Thuile, Italy, March 18-25, 2017* (2017), 1705.05064, URL https://inspirehep.net/record/1599558/files/arXiv:1705.05064.pdf.

[82] P. Adamson *et al.* (MINOS, Daya Bay), Phys. Rev. Lett. **117**(15), 151801 (2016), [Addendum: Phys. Rev. Lett.117,no.20,209901(2016)], 1607.01177.

[83] M. G. Aartsen *et al.* (IceCube), Phys. Rev. Lett. **117**(7), 071801 (2016), 1605.01990.

[84] K. Abe *et al.* (Super-Kamiokande), Phys. Rev. **D91**, 052019 (2015), 1410.2008.

[85] P. Adamson *et al.* (MINOS), Phys. Rev. Lett. **117**(15), 151803 (2016), 1607.01176.

[86] M. G. Aartsen *et al.* (IceCube), Phys. Rev. **D95**(11), 112002 (2017), 1702.05160.

[87] P. Adamson *et al.* (NOvA), Phys. Rev. D **96**(7), 072006 (2017), 1706.04592.

[88] J. Kopp, P. A. N. Machado, M. Maltoni, and T. Schwetz, JHEP **05**, 050 (2013), 1303.3011.

[89] G. H. Collin, C. A. Arguelles, J. M. Conrad, and M. H. Shaevitz, Phys. Rev. Lett. **117**(22), 221801 (2016), 1607.00011.

[90] R. Gandhi, P. Ghoshal, S. Goswami, P. Mehta, and S. U. Sankar, Phys. Rev. **D73**, 053001 (2006), hep-ph/0411252.

[91] R. Gandhi, B. Kayser, M. Masud, and S. Prakash, JHEP **11**, 039 (2015), 1508.06275.

[92] G. L. Fogli, E. Lisi, A. Marrone, D. Montanino, A. Palazzo, and A. M. Rotunno, Phys. Rev. **D86**, 013012 (2012), 1205.5254.

[93] M. Gonzalez-Garcia, M. Maltoni, and T. Schwetz, Nucl. Phys. B **908**, 199 (2016), 1512.06856.

[94] D. V. Forero, M. Tortola, and J. W. F. Valle, Phys. Rev. **D90**(9), 093006 (2014), 1405.7540.

[95] K. Abe *et al.* (T2K), Phys. Rev. D **96**(9), 092006 (2017), [Erratum: Phys.Rev.D 98, 019902 (2018)], 1707.01048.

[96] P. Adamson *et al.* (NOvA), Phys. Rev. Lett. **116**(15), 151806 (2016), 1601.05022.

[97] D. Dutta, R. Gandhi, B. Kayser, M. Masud, and S. Prakash, JHEP **11**, 122 (2016), 1607.02152.

[98] S. Goswami and T. Ota, Phys. Rev. **D78**, 033012 (2008), 0802.1434.

[99] S. Antusch, M. Blennow, E. Fernandez-Martinez, and J. Lopez-Pavon, Phys. Rev. **D80**, 033002 (2009), 0903.3986.

[100] W. Rodejohann, EPL **88**(5), 51001 (2009), 0903.4590.

[101] E. K. Akhmedov, M. Lindner, E. Schnapka, and J. W. F. Valle, Phys. Rev. **D53**, 2752 (1996), hep-ph/9509255.

[102] M. Malinsky, J. C. Romao, and J. W. F. Valle, Phys. Rev. Lett. **95**, 161801 (2005), hep-ph/0506296.

[103] Z.-z. Xing, Phys. Lett. **B718**, 1447 (2013), 1210.1523.

[104] Y.-F. Li and S. Luo, Phys. Rev. **D93**(3), 033008 (2016), 1508.00052.

[105] C. S. Fong, H. Minakata, and H. Nunokawa, JHEP **02**, 114 (2017), 1609.08623.

[106] M. Blennow, P. Coloma, E. Fernandez-Martinez, J. Hernandez-Garcia, and J. Lopez-Pavon, JHEP **04**, 153 (2017), 1609.08637.

[107] D. Dutta and P. Ghoshal, JHEP **09**, 110 (2016), 1607.02500.

[108] D. Dutta, P. Ghoshal, and S. Roy, Nucl. Phys. **B920**, 385 (2017), 1609.07094.

[109] F. J. Escrihuela, D. V. Forero, O. G. Miranda, M. Tórtola, and J. W. F. Valle (2016), 1612.07377.

[110] D. Dutta, P. Ghoshal, and S. K. Sehrawat, Phys. Rev. **D95**(9), 095007 (2017), 1610.07203.

[111] J. Tang, Y. Zhang, and Y.-F. Li, Phys. Lett. **B774**, 217 (2017), 1708.04909.

[112] Y. Abe, Y. Asano, N. Haba, and T. Yamada, Eur. Phys. J. **C77**(12), 851 (2017), 1705.03818.

[113] R. Acciarri *et al.* (DUNE) (2016), 1601.02984.

[114] P. Coloma, D. V. Forero, and S. J. Parke, JHEP **07**, 079 (2018), 1707.05348.

[115] R. Gandhi, B. Kayser, S. Prakash, and S. Roy, JHEP **11**, 202 (2017), 1708.01816.

[116] K. Abe *et al.* (Hyper-Kamiokande Proto-Collaboration), PTEP **2015**, 053C02 (2015), 1502.05199.

[117] J. M. Berryman, A. de Gouvêa, K. J. Kelly, and A. Kobach, Phys. Rev. **D92**(7), 073012 (2015), 1507.03986.

[118] S. Choubey and D. Pramanik, Phys. Lett. **B764**, 135 (2017), 1604.04731.

[119] K. J. Kelly, Phys. Rev. **D95**(11), 115009 (2017), 1703.00448.

[120] S. Choubey, D. Dutta, and D. Pramanik, Eur. Phys. J. **C78**(4), 339 (2018), 1711.07464.

[121] S. Antusch and O. Fischer, JHEP **10**, 094 (2014), 1407.6607.

[122] P. Astier *et al.* (NOMAD), Phys. Lett. **B506**, 27 (2001), hep-ex/0101041.

[123] P. Astier *et al.* (NOMAD), Phys. Lett. **B570**, 19 (2003), hep-ex/0306037.

[124] S. Parke and M. Ross-Lonergan, Phys. Rev. **D93**(11), 113009 (2016), 1508.05095.

[125] X. Qian, C. Zhang, M. Diwan, and P. Vogel (2013), 1308.5700.

[126] S. Antusch, C. Biggio, E. Fernandez-Martinez, M. B. Gavela, and J. Lopez-Pavon, JHEP **10**, 084 (2006), hep-ph/0607020.

[127] J. Hernandez-Garcia and J. Lopez-Pavon, in *Proceedings, Prospects in Neutrino Physics (NuPhys2016): London, UK, December 12-14, 2016* (2017), 1705.01840.

[128] K. Abe *et al.* (Hyper-Kamiokande), PTEP **2018**(6), 063C01 (2018), 1611.06118.

[129] K. Abe *et al.* (Hyper-Kamiokande) (2018), 1805.04163.

[130] M. Blennow and E. Fernandez-Martinez, Comput. Phys. Commun. **181**, 227 (2010), 0903.3985.

[131] O. G. Miranda, P. Pasquini, M. TÃşrtola, and J. W. F. Valle, Phys. Rev. **D97**(9), 095026 (2018), 1802.02133.

[132] D. S. Ayres *et al.* (NOvA) (2004), hep-ex/0503053.

[133] S.-F. Ge, P. Pasquini, M. Tortola, and J. W. F. Valle, Phys. Rev. **D95**(3), 033005 (2017), 1605.01670.

[134] P. F. de Salas, D. V. Forero, C. A. Ternes, M. Tortola, and J. W. F. Valle, Phys. Lett. **B782**, 633 (2018), 1708.01186.

[135] Valencia-Globalfit, http://globalfit.astroparticles.es/ (2018).

[136] NuFIT-Globalfit, http://www.nu-fit.org (2018).

[137] V. Barger, D. Marfatia, and K. Whisnant, Phys. Rev. **D65**, 073023 (2002), hep-ph/0112119.

[138] P. Huber, M. Maltoni, and T. Schwetz, Phys. Rev. **D71**, 053006 (2005), hep-ph/0501037.

[139] K. Hagiwara, N. Okamura, and K.-i. Senda, Phys. Lett. **B637**, 266 (2006), [Erratum: Phys. Lett.B641,491(2006)], hep-ph/0504061.

[140] T. Kajita, H. Minakata, S. Nakayama, and H. Nunokawa, Phys. Rev. **D75**, 013006 (2007), hep-ph/0609286.

[141] M. Ghosh, P. Ghoshal, S. Goswami, N. Nath, and S. K. Raut, Phys. Rev. **D93**(1), 013013 (2016), 1504.06283.

[142] Y. Farzan and M. Tortola, Front.in Phys. **6**, 10 (2018), 1710.09360.

[143] M. Masud, M. Bishai, and P. Mehta, Sci. Rep. **9**(1), 352 (2019), 1704.08650.

[144] C. Biggio, M. Blennow, and E. Fernandez-Martinez, JHEP **0908**, 090 (2009), 0907.0097.

[145] S. Davidson, C. Pena-Garay, N. Rius, and A. Santamaria, JHEP **03**, 011 (2003), hep-ph/0302093.

[146] J. Barranco, O. Miranda, C. Moura, and J. Valle, Phys. Rev. D **73**, 113001 (2006), hep-ph/0512195.

[147] J. Barranco, O. Miranda, C. Moura, and J. Valle, Phys. Rev. D **77**, 093014 (2008), 0711.0698.

[148] G. Mitsuka *et al.* (Super-Kamiokande Collaboration), Phys.Rev. **D84**, 113008 (2011), 1109.1889.

[149] P. Adamson *et al.* (MINOS Collaboration), Phys.Rev. **D88**(7), 072011 (2013), 1303.5314.

[150] J. Kopp, P. A. Machado, and S. J. Parke, Phys.Rev. **D82**, 113002 (2010), 1009.0014.

[151] A. M. Dziewonski and D. L. Anderson, Phys. Earth Planet. Interiors **25**, 297 (1981).

[152] C. Adams *et al.* (LBNE Collaboration), ArXiv e-prints (2013), 1307.7335.

[153] S. Agostinelli *et al.* (GEANT4), Nucl. Instrum. Meth. **A506**, 250 (2003).

[154] J. Allison *et al.*, IEEE Trans. Nucl. Sci. **53**, 270 (2006).

[155] J. Kopp, Int. J. Mod. Phys. **C19**, 523 (2008), physics/0610206.

[156] T. Kikuchi, H. Minakata, and S. Uchinami, JHEP **0903**, 114 (2009), 0809.3312.

[157] K. Asano and H. Minakata, JHEP **1106**, 022 (2011), 1103.4387.

[158] I. Esteban, M. C. Gonzalez-Garcia, M. Maltoni, I. Martinez-Soler, and J. Salvado, JHEP **08**, 180 (2018), 1805.04530.

[159] O. G. Miranda, M. A. Tortola, and J. W. F. Valle, JHEP **10**, 008 (2006), hep-ph/0406280.

[160] P. Coloma and T. Schwetz, Phys. Rev. **D94**(5), 055005 (2016), [Erratum: Phys. Rev.D95,no.7,079903(2017)], 1604.05772.

[161] K. Deepthi, S. Goswami, and N. Nath, Phys. Rev. D **96**(7), 075023 (2017), 1612.00784.

[162] G. Barenboim, M. Masud, C. A. Ternes, and M. Tórtola, Phys. Lett. **B788**, 308 (2019), 1805.11094.

[163] J. Liao, D. Marfatia, and K. Whisnant, Phys. Rev. **D93**(9), 093016 (2016), 1601.00927.

<u>Thesis Highlight</u>

Name of the Student: SAMIRAN ROY **Enrolment No.: PHYS08201304002**

Name of the CI/OCC: Harish-Chandra Research Institute, Prayagraj

Thesis Title: New Physics with Neutral and Charged Current Measurements at Long-Baseline Neutrino Experiments

Discipline: Physical Sciences **Sub-Area of Discipline: High Energy Physics**

Date of viva voce: 10th July 2020

Neutrino oscillation physics is entering into the precision measurements era. The present and future long base-line neutrino experiments could able to determine the values of oscillation parameters with more precision. Another aim of these experiments is to search for various new physics which may arise in the neutrino sector. New physics can alter the oscillation probability. Hence long-baseline experiments with huge detector mass can in principle put severe constraints on the new physics scenarios. We can detect neutrino through charged current (CC) and neutral current (NC) measurements. In literature, there are many studies on CC measurements. But NC measurements are less explored. In this thesis, we show the capability of NC and CC measurements to constrain various new physics scenarios. We also show that how the presence of new physics can alter the standard measurements at long-baseline neutrino experiments.

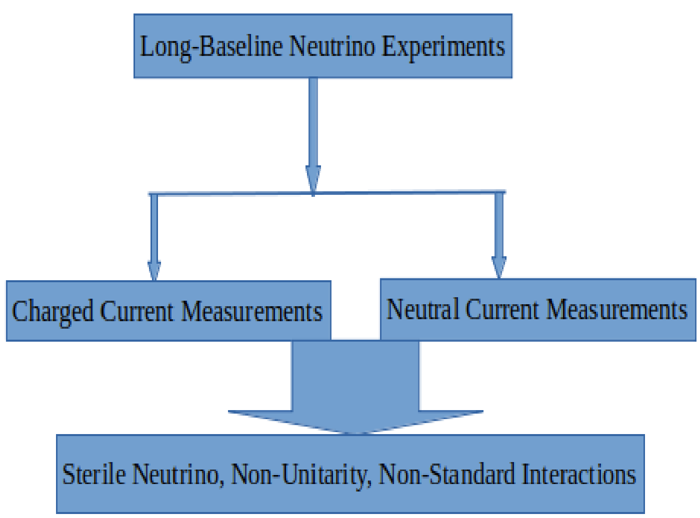

Figure 1. Schematic representation of the new physics searches at Long-Baseline Neutrino Experiments

The new physics which are in active exploration are sterile neutrino, non-unitarity, non-standard interactions (NSI) etc. The NC measurements are proportional to the total number of active flavor present in the beam. In the presence of light sterile neutrino, the active flavor can oscillate into the sterile state. Hence the number of active flavors reduces form the standard expected value. Thus, we are able to constrain some sterile parameters which are not much accessible in the CC measurements. We can also combine NC and CC measurements of the long-baseline experiments to constrain sterile and non-unitarity parameters more effectively. We observe that the different beam tune at DUNE experiment can improve the bounds on NSI parameters significantly. We also show that in the presence of non-unitarity, the mass hierarchy sensitivity of the long-baseline experiments will be deteriorated to a great extent.

NC measurements give us a new window to explore new physics scenarios in the long-baseline neutrino experiments. Finally, the combination of NC and CC measurements can constrain the new physics more effectively.